Unraveling complexity in the solid form screening of a pharmaceutical salt: Why so many forms? Why so few?

Contents of Supporting Information

A) **Crystallography**
B) **Computational**
C) **ssNMR Crystallography**
D) **Experimental**
E) **CSD-Survey**

A) Crystallography

1. Single crystal X-ray diffraction

Table S1. Crystallographic data for B5HCl crystal forms.

	Form I	Dihydrate	MeOH Solvate	MeOH Solvate
Empirical formula	$C_{16}H_{22}ClN_3O_3$	$C_{16}H_{26}ClN_3O_5$	$C_{17}H_{26}ClN_3O_4$	$C_{17}H_{26}ClN_3O_4$
Formula weight	339.81	375.85	371.86	371.86
Temperature (K)	100(2)	100(2)	100(2)	100(2)
Wavelength (Å)	1.54178	1.54178	1.54178	1.54178
Crystal size /mm	0.29 x 0.16 x 0.04	0.15 x 0.10 x 0.05	0.12 x 0.05 x 0.02	0.41 x 0.08 x 0.02
Crystal system	monoclinic	monoclinic	monoclinic	monoclinic
Space group	$P2_1/c$	$P2_1/c$	$P2_1/c$	$P2_1/c$
a (Å)	9.4935(4)	20.4540(3)	19.1192(7)	19.1672(6)
b (Å)	7.2855(3)	6.53041(10)	7.0804(3)	7.0772(2)
c (Å)	24.0201(9)	13.54956(19)	13.5975(6)	13.5789(4)
α (°)	90	90	90	90
β (°)	94.2277(13)	100.0044(8)	95.437(3)	95.390(2)
γ (°)	90	90	90	90
Volume (Å^3)	1656.83(12)	1782.33(5)	1832.43(13)	1833.84(9)
Molecules per cell (Z)	4	4	4	4
Calculated density (g cm^{-3})	1.362	1.401	1.348	1.347
Absorption coeff (mm^{-1})	2.203	2.185	2.078	2.080
F_{000}	720	800	792	792
Data collection θ range (°)	3.69 to 72.04	2.19 to 64.47	2.32 to 67.46	2.32 to 70.06
Index ranges	-11 ≤ *h* ≤ 11 -8 ≤ *k* ≤ 8 -29 ≤ *l* ≤ 29	-23 ≤ *h* ≤ 16 -7 ≤ *k* ≤ 6 -15 ≤ *l* ≤ 15	-22 ≤ *h* ≤ 22 0 ≤ *k* ≤ 8 0 ≤ *l* ≤ 15	-23 ≤ *h* ≤ 23 -8 ≤ *k* ≤ 8 -16 ≤ *l* ≤ 16
Measured, independent and observed [$I > 2\theta(I)$] reflections	51336/3256/3131	8060/2929/2653	9890/3270/3063	34893/3492/2962
Completeness (%)	99.9	97.7	98.4	100.0
Data/restraints/parameters	3256 / 2 / 216	2929 / 7 / 247	3270 / 333 / 239	3492 / 9 / 248
Goodness-of-fit on F^2	1.036	1.086	1.274	1.056
Final R indices [I>2sigma(I)]	R1 = 0.0284 wR2 = 0.0761	R1 = 0.0328 wR2 = 0.0854	R1 = 0.0811 wR2 = 0.1523	R1 = 0.0422 wR2 = 0.1008
Final R indices (all data)	R1 = 0.0294 wR2 = 0.0769	R1 = 0.0358 wR2 = 0.0877	R1 = 0.0878 wR2 = 0.1549	R1 = 0.0522 wR2 = 0.1060
Largest peak diff/hole (e·Å^{-3})	0.312 and -0.229	0.252 and -0.237	0.258 and -0.237	0.314 and -0.226

	EtOH Solvate	iPrOH Solvate	nBuOH Solvate	iBuOH Solvate
Empirical formula	$C_{18}H_{28}ClN_3O_4$	$C_{19}H_{30}ClN_3O_4$	$C_{20}H_{32}ClN_3O_4$	$C_{20}H_{32}ClN_3O_4$
Formula weight	385.88	399.91	413.93	413.93
Temperature (K)	100(2)	100(2)	100(2)	100(2)
Wavelength (Å)	1.54178	1.54178	1.54178	1.54178
Crystal size /mm	0.38 x 0.05 x 0.03	0.32 x 0.04 x 0.01	0.08 x 0.03 x 0.01	0.14 x 0.06 x 0.01
Crystal system	monoclinic	monoclinic	monoclinic	monoclinic
Space group	$P2_1/c$	$P2_1/c$	$P2_1/c$	$P2_1/c$
a (Å)	20.522(3)	20.7868(11)	22.5226(19)	22.764(3)
b (Å)	7.0606(9)	7.1728(4)	7.0668(5)	7.0293(9)
c (Å)	13.6148(17)	13.5340(7)	13.6477(12)	13.478(2)
α (°)	90	90	90	90
β (°)	96.928(6)	92.927(3)	100.516(7)	92.376(10)
γ (°)	90	90	90	90
Volume (Å^3)	1958.3(4)	2015.28(19)	2135.7(3)	2154.9(7)
Molecules per cell (Z)	4	4	4	4
Calculated density (g cm^{-3})	1.309	1.318	1.287	1.276
Absorption coeff (mm^{-1})	1.963	1.926	1.834	1.818
F_{000}	824	856	888	888
Data collection θ range (°)	6.636 to 70.068	2.128 to 72.120	3.992 to 68.241	3.887 to 54.239
Index ranges	-25 ≤ *h* ≤ 24 -8 ≤ *k* ≤ 8 -16 ≤ *l* ≤ 16	-25 ≤ *h* ≤ 25 -8 ≤ *k* ≤ 8 -16 ≤ *l* ≤ 15	-27 ≤ *h* ≤ 27 -8 ≤ *k* ≤ 8 -11 ≤ *l* ≤ 15	-23 ≤ *h* ≤ 23 -7 ≤ *k* ≤ 7 -14 ≤ *l* ≤ 14
Measured, independent and observed [$I > 2\theta(I)$] reflections	20810/3668/3350	29242/3961/3363	21720/3829/2568	19598/2624/1658
Completeness (%)	98.3	99.9	97.7	99.7
Data/restraints/parameters	3668 / 4 / 247	3961 / 4 / 257	3829 / 389 / 274	2624 / 404 / 278
Goodness-of-fit on F^2	1.164	1.056	1.232	1.103
Final R indices [I>2sigma(I)]	R1 = 0.0582 wR2 = 0.1490	R1 = 0.0406 wR2 = 0.0976	R1 = 0.1255 wR2 = 0.2687	R1 = 0.0986 wR2 = 0.1901
Final R indices (all data)	R1 = 0.0628 wR2 = 0.1518	R1 = 0.0511 wR2 = 0.1033	R1 = 0.1697 wR2 = 0.2874	R1 = 0.1566 wR2 = 0.2121
Largest peak diff/hole (e·Å^{-3})	0.670 and -0.425	0.990 and -0.249	0.484 and -0.511	0.410 and -0.378

	nPeOH Solvate	EtGly Solvate	PrGly Solvate
Empirical formula	$C_{21}H_{34}ClN_3O_4$	$C_{17}H_{25}ClN_3O_4$	$C_{17.5}H_{26}ClN_3O_4$
Formula weight	427.96	370.85	377.86
Temperature (K)	100(2)	100(2)	296(2)
Wavelength (Å)	1.54178	0.71073	1.54178
Crystal size /mm	0.31 x 0.04 x 0.02	0.12 x 0.08 x 0.02	0.12 x 0.04 x 0.02
Crystal system	monoclinic	monoclinic	orthorhombic
Space group	$P2_1/c$	$C2/c$	$Pna2_1$
a (Å)	23.5754(15)	39.137(2)	13.6770(3)
b (Å)	7.0923(4)	7.0158(4)	7.15140(10)
c (Å)	13.6146(9)	13.5444(7)	38.3289(7)
α (°)	90	90	90
β (°)	102.275(5)	103.9477(17)	90
γ (°)	90	90	90
Volume (Å^3)	2224.4(9)	3609.3(3)	3748.94(12)
Molecules per cell (Z)	4	8	8
Calculated density (g cm^{-3})	1.278	1.365	1.339
Absorption coeff (mm^{-1})	1.778	0.239	2.041
F_{000}	920	1576	1608
Data collection θ range (°)	3.838 to 68.239	3.026 to 24.767	2.305 to 67.661
Index ranges	$-28 \le h \le 28$ $-8 \le k \le 8$ $-16 \le l \le 16$	$-46 \le h \le 46$ $-8 \le k \le 8$ $-15 \le l \le 15$	$-16 \le h \le 16$ $-8 \le k \le 8$ $-45 \le l \le 45$
Measured, independent and observed [$I > 2\theta(I)$] reflections	38349/4092/2677	44493/3071/2703	43489/6670/6023
Completeness (%)	100.0	99.7	99.1
Data/restraints/parameters	4092 / 388 / 279	3071 / 4 / 237	6670 / 13 / 484
Goodness-of-fit on F^2	1.143	1.082	1.125
Final R indices [I>2sigma(I)]	R1 = 0.1438 wR2 = 0.2628	R1 = 0.0369 wR2 = 0.0834	R1 = 0.0554 wR2 = 0.1089
Final R indices (all data)	R1 = 0.1978 wR2 = 0.2881	R1 = 0.0449 wR2 = 0.0867	R1 = 0.0632 wR2 = 0.1128
Largest peak diff/hole (e·Å^{-3})	0.505 and -0.365	0.413 and -0.230	0.208 and -0.243

Table S2. 100K unit cell parameters from different B5HCl single crystals.

Solid Form	Space Group	*a* (Å)	*b* (Å)	*c* (Å)	β (°)	Volume (Å^3)
S-MeOH	$P2_1/c$	19.1146(9)	7.0796(3)	13.5933(6)	95.426(4)	1831.25(14)
S-MeOH	$P2_1/c$	19.1779(11)	7.0885(3)	13.5733(8)	95.210(4)	1837.57(17)
S-MeOH	$P2_1/c$	19.159(2)	7.0788(8)	13.578(2)	95.372(9)	1833.4(4)
S-MeOH	$P2_1/c$	19.152(5)	7.0701(12)	13.551(3)	95.30 (2)	1827.1(7)
S-MeOH	$P2_1/c$	19.171(4)	7.0817(12)	13.544(3)	95.358(14)	1830.8(6)
S-iPrOH	$P2_1/c$	20.781(4)	7.168(2)	13.548(3)	92.94(3)	2015.4(8)
S-iPrOH	$P2_1/c$	20.7756(12)	7.1629(4)	13.5442(8)	92.925(3)	2012.9(2)
S-iPrOH	$P2_1/c$	20.7854(12)	7.1748(4)	13.5299(8)	92.979(3)	2015.0(2)
S-iPrOH	$P2_1/c$	20.8200(13)	7.1390(5)	13.4896(9)	92.809(5)	2002.6(2)

2. Powder X-ray diffraction

The diffraction patterns were indexed with DICVOL04 using > 12 peaks. The space group was determined on the basis of a statistical assessment of systematic absences[1] as implemented in the DASH structure solution package.[2]

Table S3. Unit cell parameters and space group symmetry derived from indexation of RT PXRD patterns.

Solid Form	Space Group	a (Å)	b (Å)	c (Å)	beta (°)	Volume (Å^3)
Form I	$P2_1/c$	9.5367(3)	7.3624(1)	24.0794(7)	94.146(2)	1686.27(8)
Form II	$P2_1/c$	19.4919(3)	6.51644(15)	13.2350(2)	91.404(2)	1680.58(5)
Dihydrate	$P2_1/c$	20.5412(8)	6.5860(2)	13.7486(4)	100.149(2)	1830.87(11)
S-MeOH	$P2_1/c$	19.2743(7)	7.1506(1)	13.7116(3)	94.913(2)	1882.82(9)
S-EtOH	$P2_1/c$	20.8325(14)	7.1543(1)	13.6644(16)	93.581(10)	2032.60(29)
S-nPrOH	$P2_1/c$	22.7810(12)	7.1269(4)	13.6760(10)	101.572(8)	2175.27(25)
S-iPrOH	$P2_1/c$	20.9214(12)	7.2506(2)	13.6223(12)	92.874(7)	2063.82(23)
S-nBuOH	$P2_1/c$	22.6813(19)	7.1622(2)	13.6973(6)	99.110(3)	2197.04(23)
S-2BuOH	$P2_1/c$	22.4726(16)	7.1572(2)	13.6931(6)	90.817(3)	2202.18(20)
S-iBuOH	$P2_1/c$	23.6864(24)	7.1530(2)	13.6322(7)	105.244(4)	2228.42(27)
S-nPeOH	$P2_1/c$	23.9611(16)	7.1818(2)	13.6823(12)	99.797(7)	2320.16(28)
S-nOcOH	$P2_1/c$	26.9672(13)	7.2014(2)	13.7024(9)	103.794(3)	2548.29(24)
S-EtGly	$C2/c$	39.2019(16)	7.0831(2)	13.6181(4)	103.764(2)	3672.76(22)
S-PrGly	$Pna2_1$	13.6663(8)	7.1511(2)	38.3118(31)	90	3744.19(41)

B) Computational

3. Crystal Structure Prediction study details and supplementary results

CSD searches confirmed that the piperazine ring of $B5H^+$ cation can be kept in its chair conformation and the benzisoxazole ring kept planar, though the other components of the $B5H^+$ cation must remain flexible: the dimethylpropanoic acid group, the torsion between the piperazine and benzisoxazole rings, and the proton H22 on N3 atom can be either in the equatorial (*e)* or axial *(a)* position. The atomic numbering and torsion angles used in the search are shown in m/s Figure 1a.

3.1. Conformational analysis of gas-phase $B5H^+$ cation

10 unique conformations of $B5H^+$ cation (Figure S1) were optimized in gas phase at PBE0/6-31G(d,p) level using Gaussian03, allowing for either axial or equatorial substitutions on N2 and N3 sites. These conformations, represented as sets of torsion angles, are contrasted in Table S4 with those observed in the experimental structures.

Table S4. Comparison of $B5H^+$ conformations in all experimental crystal structures and optimized gas-phase structures at PBE0/6-31G(d,p) level. Colours link the crystalline conformations to the nearest isolated ion conformational minimum.

Solid Form	ϕ1 (°) C9-N3-C12-C13	ϕ2 (°) N3-C12-C13-C14	ϕ3 (°) C12-C13-C14-O3	ϕ4 (°) C13-C14-O3-H1	ϕ5 (°) C2-C1-N2-C8	ΔE_{intra} (kJ/mol)
Experimental structures						
Form I	65.79	-74.95	142.63	-178.29	-179.32	
Form II	-130.09	-74.24	-52.29	-178.04	163.31	
Dihydrate	-123.53	66.00	176.37	177.28	167.67	
S-MeOH	104.70	68.51	-177.94	-165.03	178.53	
S-EtOH	105.87	70.63	-177.25	-176.21	179.29	
S-IPA	104.51	70.90	-177.15	-168.97	179.62	
S-nBuOH	104.65	69.13	-174.32	-161.07	178.94	
S-iBuOH	103.53	71.46	-175.72	-165.38	-178.87	
S-PeOH	104.47	69.43	-172.74	-168.81	178.72	
S-EtGly	104.05	70.62	-179.33	-179.58	-179.66	
S-PrGly	104.51	70.87	-178.77	-179.38	179.10	
Form I (FB)	89.32	45.76	-34.57	0.02	178.23	
Gas-phase optimized structures						
N2-equ. N3-equ. (*ee* region in CSP search)						
OptFormI	70.71	-85.16	173.85	176.58	172.44	32.28
IntraO1	93.04	51.46	149.73	175.70	172.9	6.28
IntraO2	141.07	-51.42	-147.82	-175.90	173.15	6.91
IntraOH1	96.91	64.62	-50.46	-176.18	171.95	32.31
IntraOH2	137.91	-64.56	50.26	176.56	172.69	31.93
N2-equ. N3-axial (*ea* region in CSP search)						
Opt2H2O	-138.24	50.90	145.57	175.91	171.57	14.71
OptFormII	-95.62	-51.14	-146.39	-175.74	171.53	14.03
N2-axial N3-equ.						
N2aN3eOpt1	69.74	-84.89	170.29	175.88	-166.55	28.78
N2aN3eIntra	92.36	51.32	149.64	175.79	-166.70	0.0
N2-axial N3-axial						
N2aN3aIntra	-137.59	50.69	145.36	175.87	-167.19	10.77

As shown in Figure S1, in the absence of their pairing chloride ions and in gas phase, the $B5H^+$ cation can form internal hydrogen bonds between the carbonyl group and protonated piperazine ring, e.g. OptFormII, with a low ΔE_{intra} similar to the neutral B5 molecule. The Form I conformation of $B5H^+$ (OptFormI) is at a high relative energy, as it does not form any intramolecular hydrogen bond. However, in the presence of a chloride ion, it will most certainly occupy a position close to N3-H22 bond, thus disrupting any possible intramolecular hydrogen bonds between N3-H22 and the carboxylic group.

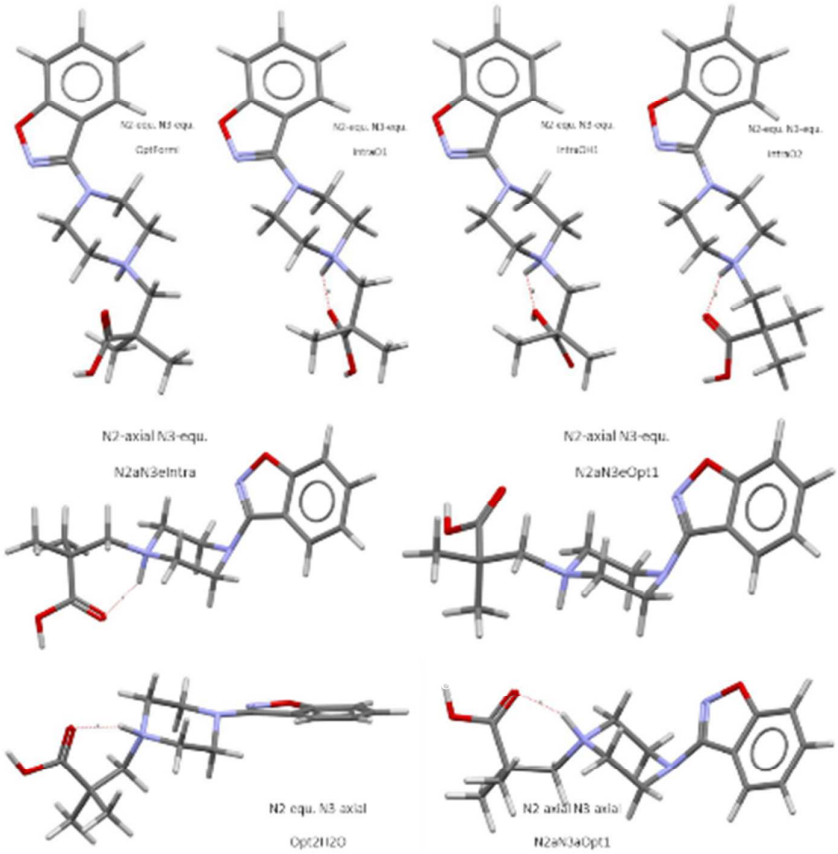

Figure S1. A selection of optimized gas-phase structures of $B5H^+$ cation in four conformational regions, obtained at PBE0/6-31G(d,p) level. See Table S4 for the complete list.

3.2. CrystalPredictor grid generation for the flexible cation

Current CSP study of B5HCl crystal energy landscape covered the following two separate regions, covering most but not all of the low energy conformations without an intramolecular hydrogen bond:

1) N2-equ. N3-equ. (*ee*) region: The conformations of $B5H^+$ in Form I and alcohol solvates structures are found in this region.
2) N2-equ. N3-axial (*ea*) region: The conformation of $B5H^+$ in Form II and the dihydrate structures lie in this region.

Four torsion angles, ϕ1, ϕ2, ϕ3, ϕ5, were used to construct the grids of intramolecular energy penalties used in CrystalPredictor search (Figure S2 and Figure S3), with torsion group 1 including three torsion angles in the dimethylpropanoic acid tail:

1) ϕ1: C9-N3-C12-C13, from 20° to 340° in 40° step (*ee*) or from 140° to 340° in 40° step (*ea*), due to higher energy penalty in the *ea* region from steric clash of the bulky dimethyl-propanyl acid tail on the N3 axial position;
2) ϕ2: N3-C12-C13-C14, from -100° to 220° in 40° step.
3) ϕ3: O3-C14-C13-C12, from 20° to 340° in 40° step.

and torsion group 2 including the torsion angle between the benzisoxazole and piperazine rings:

4) ϕ5: C8-N2-C1-C2, from 150° to 210° in 20 step°.

The separation into two torsion groups is based on the assumption that conformational changes of substituted groups on N2 and N3 sites will be largely independent from each other, which was shown to be reasonable from Figure S2.

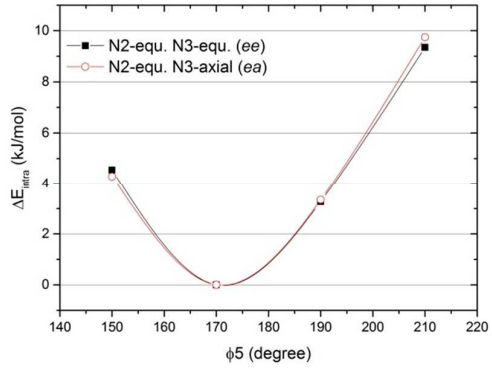

Figure S2. $B5H^+$ potential energy curves from grid calculations at PBE0/6-31G(d,p) level in torsion group 2 (ϕ_5) in the *ee* and the *ea* regions.

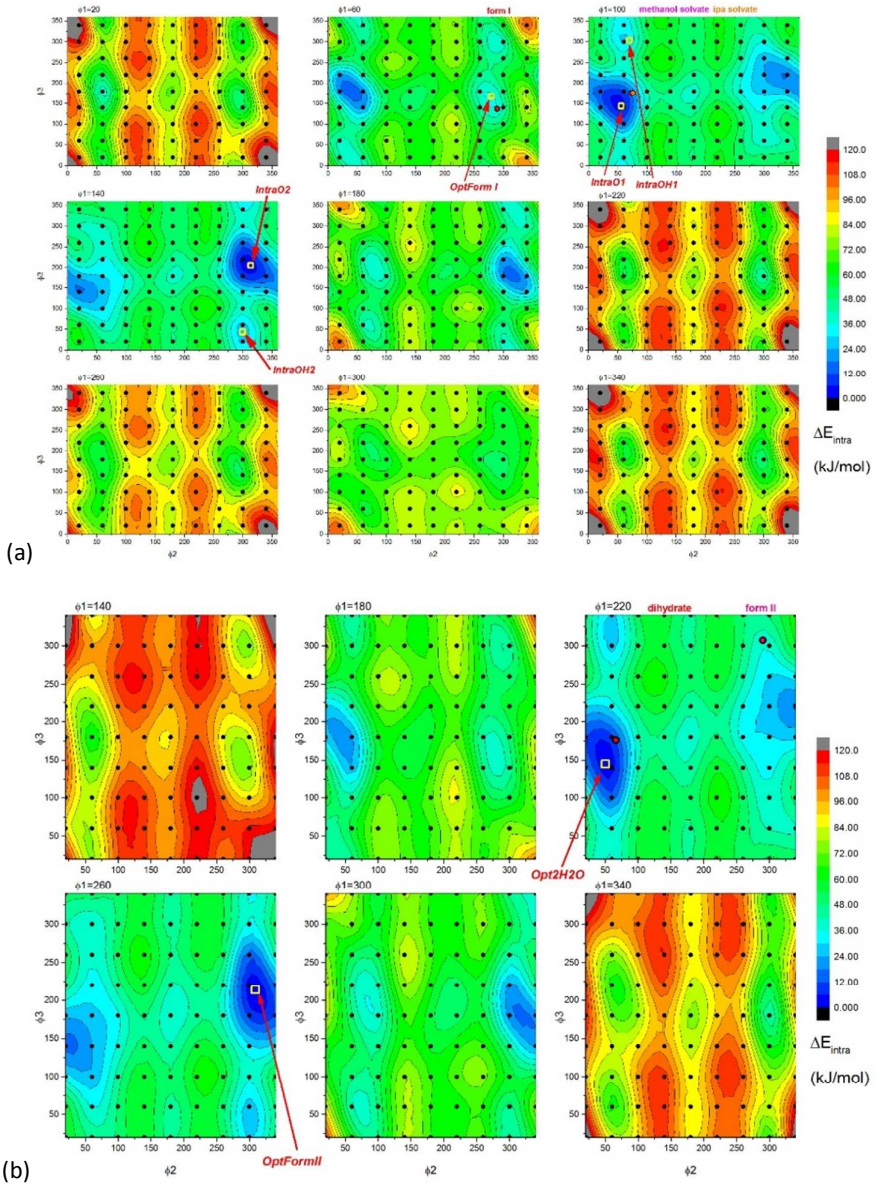

Figure S3. $B5H^+$ cation potential energy surface from grid calculations in the *ee* (a) and *ea* (b) region at PBE0/6-31G(d,p) level in torsion group 1 (ϕ1-ϕ2-ϕ3), shown as contours on ϕ2-ϕ3 plane on ϕ1 sections. Energy difference between adjacent contours is 6kJ mol^{-1}. The coloured circles corresponds to approximately the conformation of $B5H^+$ cation in experimental structures, while fully optimized conformations in Table S4 were labelled with hollow yellow squares. Energy zero was set to the global minimum in Table S4. The black dots are the calculated grid points.

3.3. CrystalPredictor search in the ee and ea region

Two separate CrystalPredictor (version 1.6) searches were carried out for the *ee* and *ea* regions in the 59 most common space groups. The structures are henceforth labelled by their rank (#) after the search stage as either "*ea*" or "*ee*". Potential-derived atomic charges, calculated at PBE0/6-31G(d,p) level for the IntraO2(*ee*) and Opt2H2O(*ea*) conformations, were used for electrostatic interactions and empirical FIT potential was used for dispersion-repulsion interactions.

For the *ee* region, a total of one and a half million minimisations were carried out (Figure S4 left) generating 494,177 unique crystal structures. The most frequently found crystal structure was found 1153 times, but most structures were found less than 10 times, and the experimental structure, was found only once as *ee*568. For the *ea* region one million minimisations were performed generating 28,113 unique structures. Form II was found once as *ea*209, while the computational desolvated dihydrate structure was found 16 times as *ea*333. Compared with the search in the *ee* region, lower-lying crystal structures in the *ea* region were generated significantly more frequently. This shows that there is a significant difference in the completeness of the two searches.

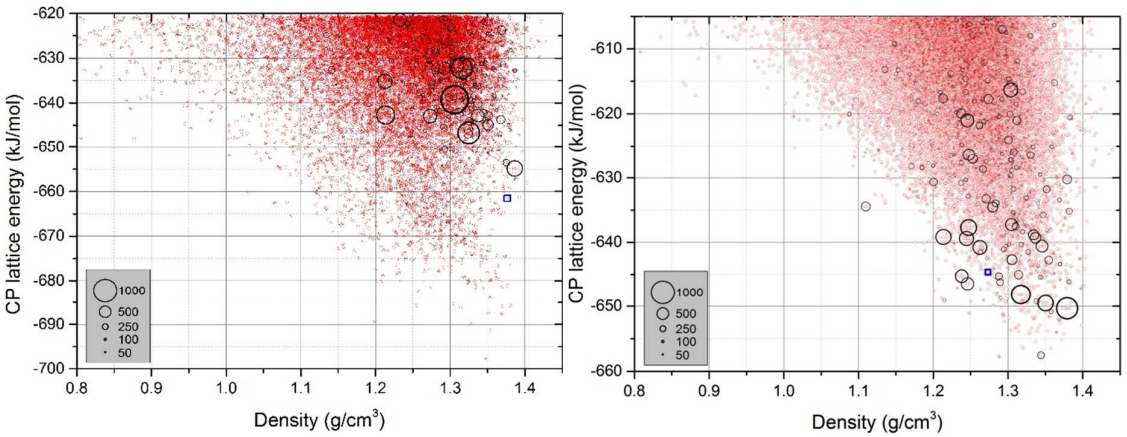

Figure S4. Lattice energy-density distribution of lower-lying B5HCl crystal structures (red circles) in the *ee* (left) and *ea* (right) region, generated with CrystalPredictor1.6. Red circles are of uniform size, labelling the position of each structure, while the size of black circles corresponds to the frequency a specific crystal structure was found in the CrystalPredictor search. The blue squares in the *ee* and *ea* region label the structures (*ee*568 and *ea*209) which match the experimentally observed anhydrous form I and II of B5HCl.

3.4. Final refinement of crystal structures

1) Combined lattice energy landscape of the *ee* and *ea* region

As in the 6th CCDC blind test, an intermediate one-step CrystalOptimizer evaluation was used to re-rank CrystalPredictor-minimised structures, then full CrystalOptimizer optimizations were carried out for the lowest 1925 structures in the *ee* region and 585 structures in the *ea* region, encompassing all unique structures with one-step CrystalOptimizer lattice energy lower than –620 kJ mol^{-1}. The experimental Form I of B5HCl was found as one of the lower-lying structures (*ee*568) with $RMSD_{15}$ = 0.282Å and $RMSD_{15+}$ = 0.328Å. It is 1.7 kJ mol^{-1} higher in lattice energy than that of the global minimum *ee*860, which corresponds to a dimer-based structure.

In the *ea* region, B5HCl Form II is found as *ea*209, with RMSD15 = 0.208 Å and $RMSD_{15+}$ = 0.212 Å, using a slightly larger angular tolerance in MERCURY (25° instead of the default 20°). The larger tolerance is necessary due to an obvious difference in ϕ3 for the carboxylic acid group of the cation. Nevertheless, all other aspects of the molecular packings in form II were well-reproduced in the CSP study. *ea*209 is highly metastable, 13.0 kJ mol^{-1} higher in energy than the global

minimum *ee*860 and 11.3 kJ mol^{-1} higher than Form I (*ee*568). The computationally dehydrated B5HCl dihydrate structure (*ea*333) is only slightly higher (0.6 kJ mol^{-1}) in energy than Form II (*ea*209). Figure S5 shows the combined lattice energy landscape of B5HCl containing both the *ee* and *ea* regions. The lowest energy minimum in the *ea* region, *ea*134, is only 1.16 kJ mol^{-1} higher in lattice energy than the global energy minimum, *ee*860, and both are competitive in energy with the experimentally observed anhydrous Form I.

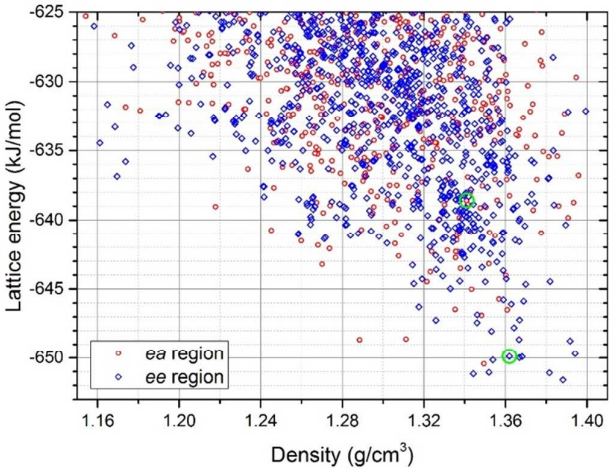

Figure S5. Overlay of lattice energy landscapes of B5HCl salt in the *ee* and *ea* regions, calculated at PBE0/6-31G(d,p)/FIT level. Experimental anhydrous Forms I and II corresponds to the structures in green circles.

2) Structural analysis of low energy structures

The low energy structures in *ee* and *ea* regions were analysed for their hydrogen bonding motifs in the lattice energy landscape in Figure S6. This does not discriminate very well, as the common NH$^+$···Cl$^-$···HOOC– hydrogen-bonding motif can have the two donors at very different angles, but the same graph set. Hence an XPac analysis was carried out on the lowest energy structures, with those for the *ee* region in Figure S7 and in Figure S8 for *ea*. Table S5 lists the final CrystalOptimizer optimized results of these structures, along with other structures mentioned in this paper.

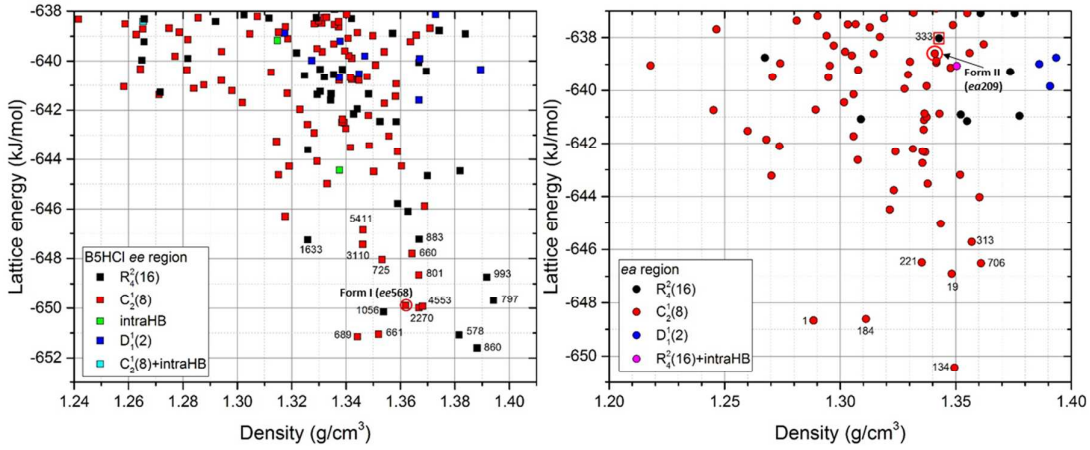

Figure S6. Lattice energy landscape of B5HCl in the *ee* (left) and *ea* (right) region, calculated at PBE0/6-31G(d,p)/FIT level. Experimental anhydrous forms correspond to the structures in red circles. Crystal structures are indexed with their hydrogen-bonding motifs determined with the Graph Set utility in Mercury. Only those structures discussed in details in the text are labelled.

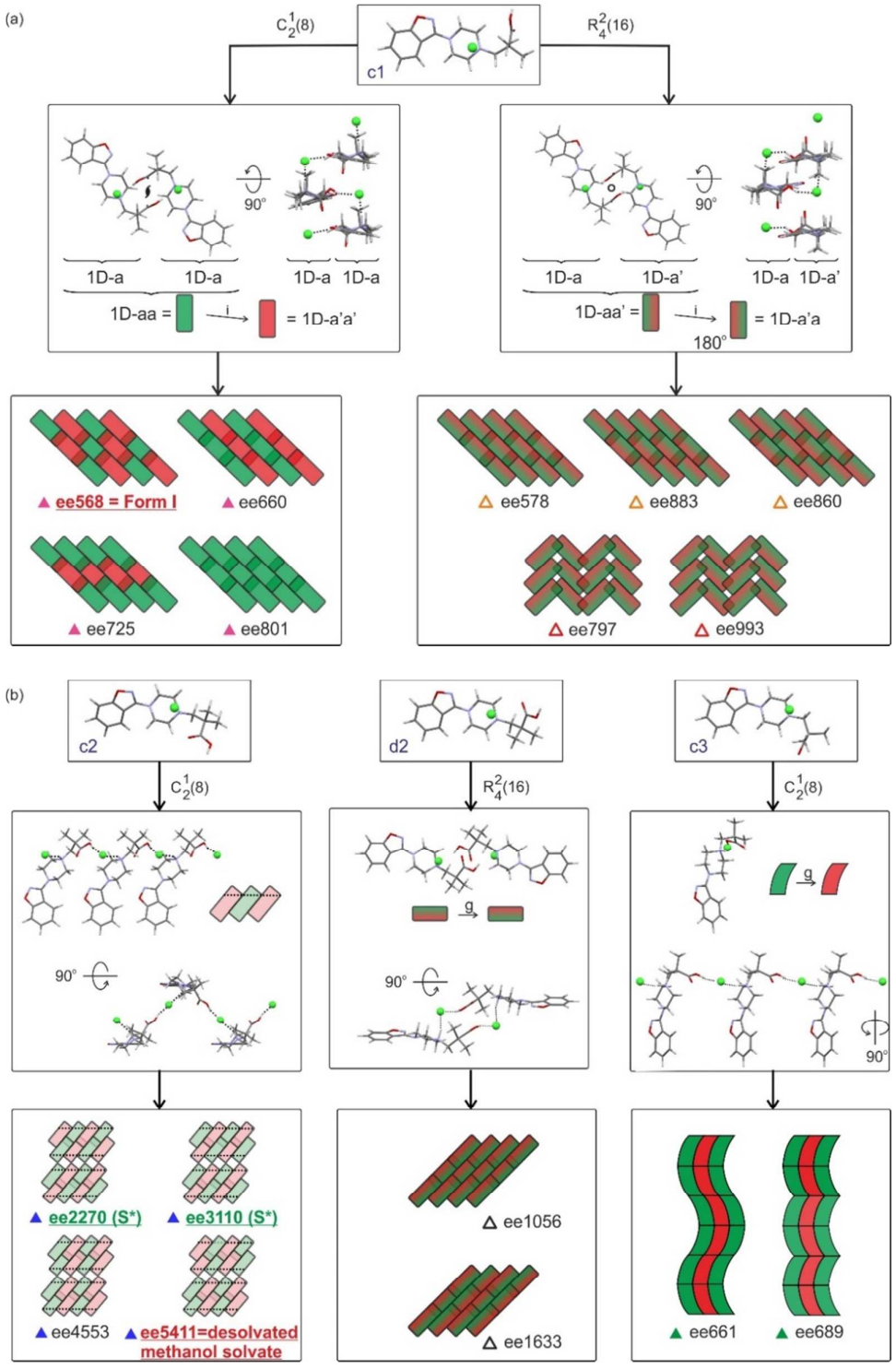

Figure S7. Key to low energy CSP generated B5HCl structures with the *ee* conformation showing the hydrogen bonding motifs and packing similarities, (a) the c1 conformation and (b) the c2, d2 and c3 conformations. 1D-a (1D-a') etc are 1-dimensional supramolecular constructs stacked in direction of plane. The C1,2(8) and R2,4(16) motifs are indicated with green and red symbols (green – COOH hydroxyl group pointing into the plane, red - COOH hydroxyl group pointing out of the plane). i – inversion. g – glide. Dotted lines indicate hydrogen bonding. S* – 2D packing similarity with all solvates except S-MeOH.

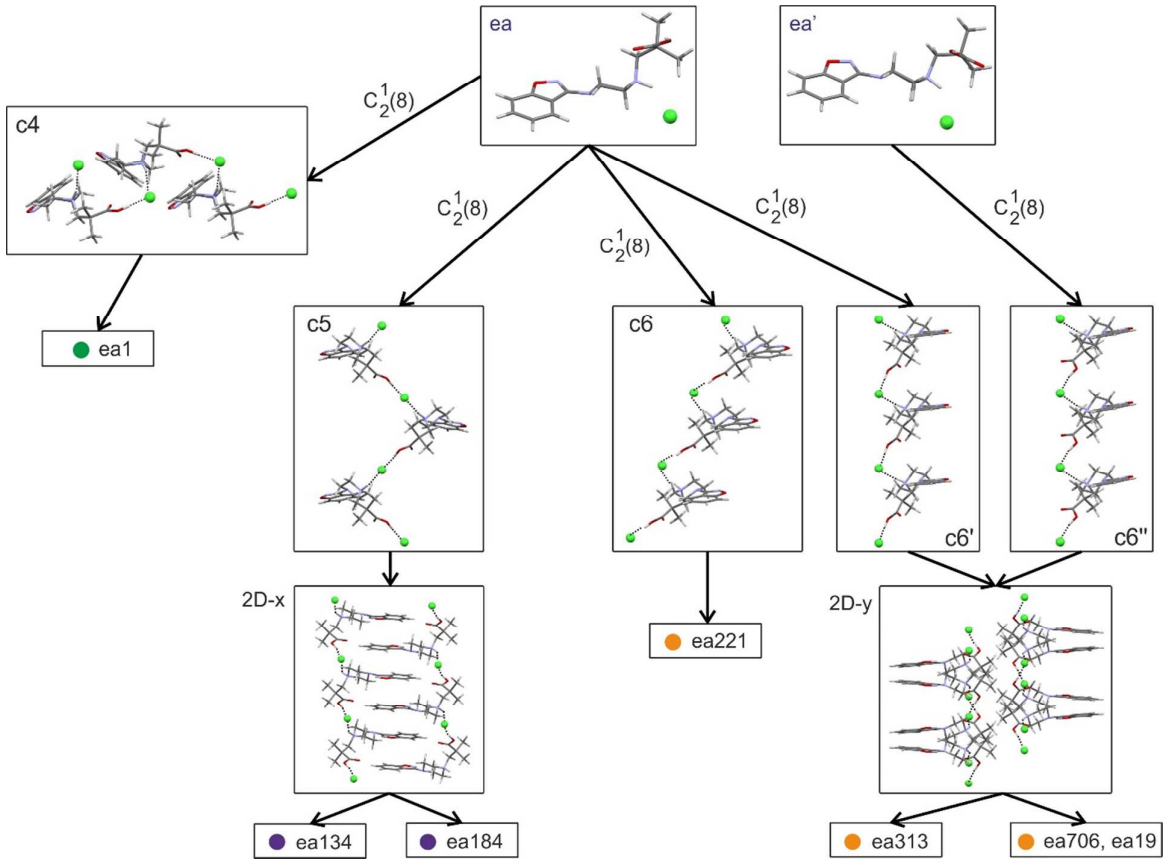

Figure S8. Illustration of the hydrogen bonding motifs and 2D packing similarities of B5HCl structures showing the *ea* (*ea*') conformations. Note that *ea and *ea' differ only in positon of the COOH proton. 2D-x and 2D-y are 2-dimensional supramolecular constructs present in at least two structures. Form II adopts ea' conformation and C5 HB chains but is not included in the XPac analysis as high in energy.

Table S5. Optimized cell parameters of CSP structures in the *ee* and *ea* regions, obtained after full CrystalOptimizer optimizations, organised by hydrogen-bonding motif. ΔE_{latt} is lattice energy relative to the global minimum, highlighted in yellow. The CSP structures corresponding to the experimental structure are shaded in green, while orange denotes computationally desolvated structures found in CSP, i.e. *ee*5411 (S-MeOH), and *ea*333 (DH).

	Space group	a (Å)	b (Å)	c (Å)	α (°)	β (°)	γ (°)	Density (g/cm^3)	ΔE_{latt} (kJ/mol)
Form I	$P2_1/c$	9.7193	7.1323	23.9907	90.00	94.95	90.00	1.3623	1.39
Form II	$P2_1/c$	19.7279	6.5155	13.0975	90.00	92.22	90.00	1.3417	12.97
Group c1 -- hydrogen-bonded chains, packed in planes									
***ee*568**	$P2_1/c$	9.7393	7.1165	24.0050	90.00	84.96	90.00	1.3619	1.71
***ee*801**	$P2_1$	9.7868	7.0724	11.9859	90.00	95.54	90.00	1.3667	2.95
***ee*725**	$P2_1/a$	19.9159	7.1153	11.8074	90.00	85.50	90.00	1.3532	3.56
***ee*660**	$P2_1/n$	14.7988	7.0382	16.1370	90.00	79.87	90.00	1.3642	3.79
Group c2 -- hydrogen-bonded chains, parallel-displaced packed into double layers									
***ee*2270**	$P2_1/c$	19.6241	6.7144	13.4288	90.00	68.96	90.00	1.3668	1.61
***ee*4553**	$P2_1/c$	22.6234	6.6556	13.4966	90.00	125.72	90.00	1.3681	1.67

***ee*3110**	$P2_1/c$	18.7223	6.7182	13.3579	90.00	86.37	90.00	1.3461	4.16
***ee*5411**	$P2_1/c$	19.5730	6.6485	13.4470	90.00	106.63	90.00	1.3462	4.74
Group c3 -- hydrogen-bonded chains, herring-bone packed into double layers									
***ee*689**	$Pca2_1$	9.0256	17.0946	10.8831	90.00	90.00	90.00	1.3442	0.45
***ee*661**	Pbca	33.9891	9.0157	10.8972	90.00	90.00	90.00	1.3519	0.55
Group d1 -- hydrogen-bonded dimers, packed in planes c.f. Group c1									
***ee*860**	$P2_1/c$	9.7187	6.9939	24.0509	90.00	84.02	90.00	1.3882	0.00
***ee*578**	P-1	7.0283	9.8588	11.9000	84.36	87.33	94.40	1.3815	0.52
***ee*883**	$P2_1/c$	11.7690	7.0007	20.1370	90.00	84.45	90.00	1.3669	4.36
Group d1' -- hydrogen-bonded dimers, packed in a zigzagging way									
***ee*797**	$P2_1/c$	9.5696	24.0786	7.0281	90.00	88.52	90.00	1.3942	1.91
***ee*993**	P2/c	7.0425	9.4399	26.9223	90.00	115.02	90.00	1.3917	2.86
Group d2 -- hydrogen-bonded dimers									
***ee*1056**	P-1	7.4509	7.1420	16.1463	84.70	85.23	77.54	1.3538	1.44
***ee*1633**	$P2_1/c$	16.9072	7.0637	15.2403	90.00	110.72	90.00	1.3259	4.35
Group c4									
***ea*1**	$P2_1/c$	11.4616	13.3513	11.4551	90.00	87.90	90.00	1.2885	2.93
Group c5									
***ea*134**	C2/c	36.2904	6.5712	14.5429	90.00	105.28	90.00	1.3494	1.16
***ea*184**	A2/n	14.0166	6.6247	37.1445	90.00	86.54	90.00	1.3112	2.99
***ea*209**	$P2_1/c$	19.7265	6.5209	13.0949	90.00	87.71	90.00	1.3410	13.01
Group c6, c6' and c6''									
***ea*19**	Pbca	12.0005	39.1955	7.1180	90.00	90.00	90.00	1.3484	4.70
***ea*706**	Pbca	11.9930	36.6940	7.5379	90.00	90.00	90.00	1.3609	5.09
***ea*221**	P-1	6.6451	20.8325	7.8154	100.17	62.57	118.20	1.3353	5.12
***ea*313**	$P2_1/c$	18.4810	7.6639	11.8730	90.00	81.57	90.00	1.3569	5.88
Structures of B5HCl obtained by computational desolvation of SXRD structures									
***ea*333**	$P2_1/c$	19.4147	6.8397	13.4519	90.00	70.22	90.00	1.3428	13.58
Desolvated S-EtGly	C2/c	39.9031	6.6683	13.3399	90.00	95.15	90.00	1.2720	12.14
Desolvated S-PrGly	$Pna2_1$	13.3373	6.6653	39.5372	90.00	90.00	90.00	1.2844	11.78
Desolvated S-IPA	$P2_1/c$	17.2077	6.9999	13.7539	90.00	90.36	90.00	1.3624	33.47

3.5. Sensitivity of lattice energies to computational models

There has been much less work on testing different computational models for ionic systems than for neutral organic molecules, and hence it is worth assessing how much the relative lattice energies change with modifications to the model for the intermolecular forces.

1) Effect of changing *exp-6* potential on lattice energy landscape

Williams potential along with a specific repulsion-dispersion potential for the chloride ion, kindly made available by Prof. Graeme Day (W99+Cl^-), was used to assess how much the relative lattice energies change with modifications to the model for the intermolecular forces. CrystalOptimizer

re-optimizations were performed for the set of the 17 crystal structures in the *ee* region listed in Table S5. The X-H distances were foreshortened in all these calculations, as is standard for the W99 potential.[3] The effect of just changing the Cl parameters, which changes all the repulsion-dispersion interactions involving the Cl^- ion through the combining rules, in conjunction with the original FIT potential was also tested (as FIT+Cl^-). The results in Figure S9 show that the lattice energies with the W99+Cl^- potential span a much wider energy range (~13.9 kJ mol^{-1}), compared to ~4.8 kJ mol^{-1} with FIT, changing the global minimum structure to *ee*2270 and increasing the energy gap between the global minimum and form I (*ee*568) from 1.5 to 7.2 kJ mol^{-1}, though the ranking is similar.

The re-ranking of crystal structures is correlated to the packing features (Figure S9 top right), as symbols for the same packing type lie approximately on lines parallel to the dashed line of no change. The chain-based Group c1 structures and the dimer-based Groups d1 and d1' structures moved much higher in lattice energy, while the double-layer-based Group c2 structures moved lower and actually ranked the first to the fourth in the 17 structures.

Although it is difficult to say which energy landscape gives us a more realistic picture, it is worth noting that with W99-Cl^- potential, the computationally desolvated methanol solvate (*ee*5411), is more stable than Form I (*ee*568) by 4.1 kJ mol^{-1}, contradicting experimental observations.

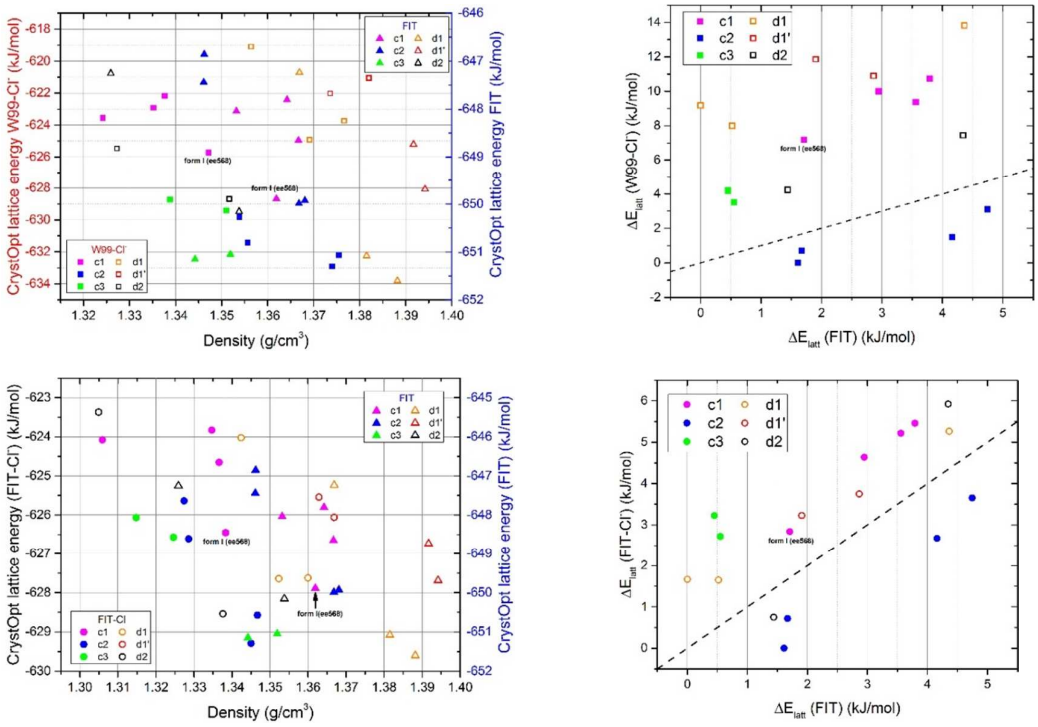

Figure S9. (top-left) Comparison of calculated lattice energies using CrystalOptimizer/FIT (triangles) and CrystalOptimizer/W99-Cl^- (squares) potentials for the 17 CrystalOptimizer structures in Table S5; (top-right) Change in relative lattice energies of the crystal structures listed in Table S5, using FIT and W99-Cl^- potentials. The dash line is the line of no change; (bottom) The same comparison between the FIT and FIT-Cl^- potentials.

2) Effect of polarisable continuum

Although a Polarisable Continuum Model (PCM) cannot model the crystal-specific polarising effect of the chloride ions on the cation, it can be used as an indication of how sensitive the energy landscape is to an overall polarizing effect. Both CrystalOptimizer/FIT and CrystalOptimizer/W99-Cl^- relative energies were refined with DMACRYS and a PCM model by recalculating ΔE_{intra} and the distributed multipoles with dielectric constant ε=11, the averaged values for organic salts.[4]

As shown in Figure S10, the rankings of crystal structures obtained with both FIT and W99-Cl^- repulsion-dispersion potentials are sensitive to the inclusion of PCM polarisation, with structures of the same packing type showing a similar shift in their relative energy. The overall effect of the inclusion of PCM polarisation is to make the two energy landscapes more comparable with each other, and to increase the energy range of the structures.

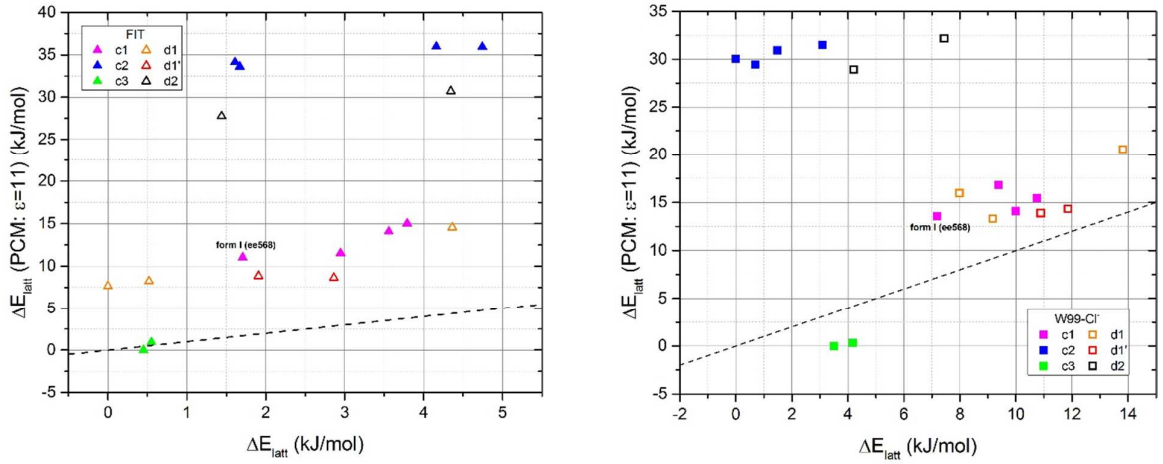

Figure S10. Change of relative lattice energies when PCM (ε=11) polarization was included in Gaussian calculations to obtain distributed multipoles and ΔE_{intra}, for the 17 structures in Table S5, with each packing group (Table S5) shown in a specific colour. The dashed line implies no change in relative energies: left for FIT and right for W99 with chloride ion potential (see text).

4. Comparison of B5HCl and B5 crystal structures on the computationally generated crystal energy landscapes

4.1. Conformational Diversity

The B5 anhydrate crystal energy landscape had only four conformations (six if the position of the carboxylic acid proton is taken into account) among the lowest energy structures (Figure S11); the B5HCl crystal energy landscape has five conformations (six if the positon of the carboxylic acid proton is taken into account) among the lowest energy structures: four in *ee* and one (two) in *ea* region. The B5HCl conformations seen in the most stable structures are distinct from the conformations seen in the computed B5 low-energy (and density) structures, reflecting the influence of the strong ionic interactions (Cl^-···H–N and Cl^-···H–O) on the most favourable crystal conformations.

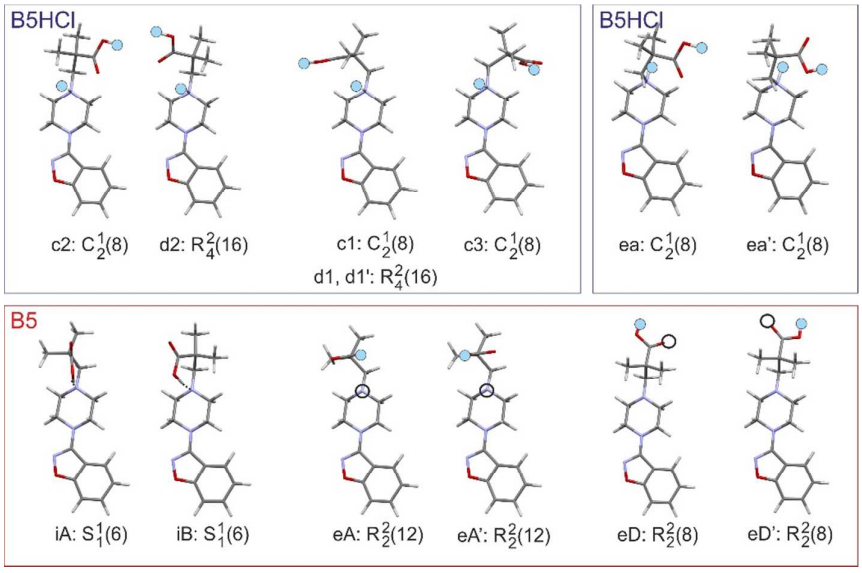

Figure S11. B5HCl and B5 conformations and graph-set motifs observed among the most favourable calculated structures. The hydrogen bond donor (light-blue dot) and acceptor (open circle) that are used in the most favourable intermolecular interactions of a given conformation are marked.

4.2. Hydrogen-bonding Diversity

Graph set motif analysis[5] of the lowest-energy B5 and B5HCl structures revealed that the most stable B5 structures have either an intramolecular H-bond (S) or ring (R) motifs. The R motifs involve either only the COOH function as donor and acceptor or the COOH as donor and piperazine N3 as acceptor. H-bond chain motifs (C) are possible but were found only in higher energy structures.

In B5HCl the N3 piperazine nitrogen is protonated. Furthermore, salt formation of B5, i.e. B5HCl, introduces another strong (ionic) H-bond acceptor, Cl^-, to the system. In all lowest-energy structures the $B5H^+$ cations form no strong $B5H^+\cdots B5H^+$ H-bonding interactions. All structures have strong N3–H$\cdots Cl^-\cdots$H-OCO interactions. Thus, $B5H^+$ does not act as H-bond acceptor. Two motifs, one chain (C1,2(8)) and one ring (R2,4(16)), were identified among the lowest-energy structures. In contrast to neutral B5, a B5HCl conformation can form more than one hydrogen bonding motif (Figure S11, c1/d1).

The two compounds, differing only in protonation of the piperazine N3 atom, differ substantially in H-bonding preference, because Cl^- is a stronger acceptor than the $B5H^+$ acceptor groups.

4.3. Crystal Packing Diversity

The packing modes adopted by the B5 and $B5H^+$ molecules in the lowest-energy structures were compared using the *XPac* method. All non-H atoms of the B5 and piperazine ring moieties were chosen as corresponding points. Despite the fact that the two compounds differ in conformation and strong H-bond interactions, it was possible to identify common 1D supramolecular constructs (Figure S12, Figure S13). All three 1D B5 SCs[6] were also found in B5HCl CSP structures. In B5 structures the 1D-B motif dominates, whereas in $B5H^+$ the 1D-C based motif is the most frequently

observed one among the lowest-energy structures. As seen in Figure S12, the 1D SCs do not involve hydrogen bonding and are dominated by close contacts only (especially 1D-B).

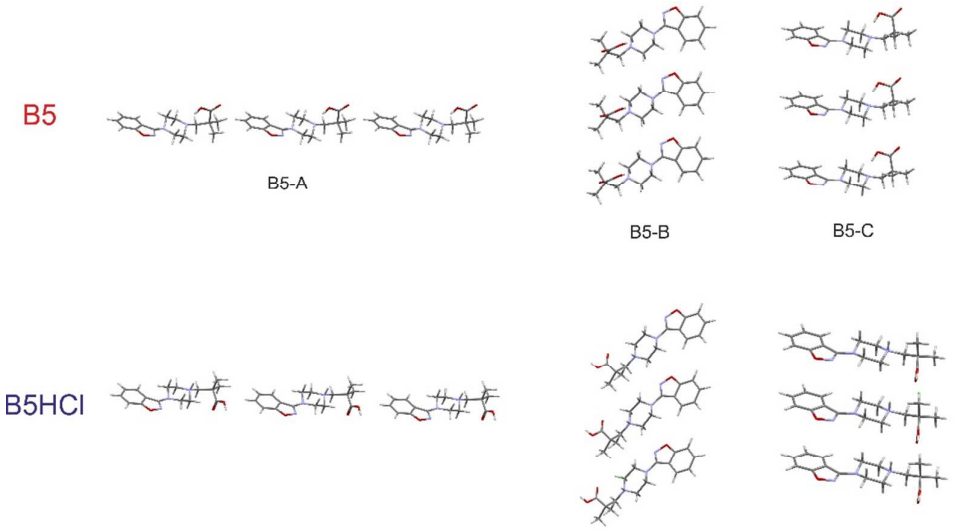

Figure S12. Illustration of the common 1D supramolecular constructs (SCs) found in B5 and B5HCl lowest-energy structures.

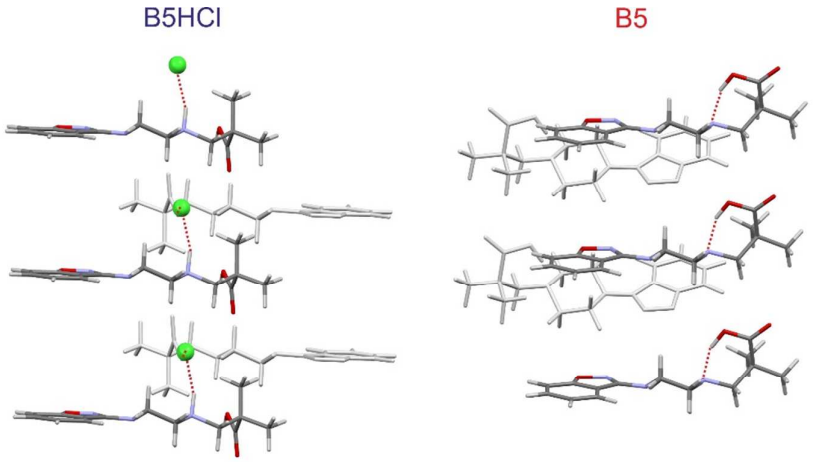

Figure S13. Comparison of the B5-C motif (colored by element) seen in many CSP generated B5HCl structures, and some B5 structures. This is the greatest similarity found, and does not involve molecules in van der Waals contact. The pale molecules exemplarily indicate adjacent B5-C motifs leading to different packings in B5HCl and B5. Red dotted lines indicate the strong H-bond interactions.

In the structure of B5HCl, the packing of the cation benzisoxazole and piperazine groups is clearly constrained by the binding to the Cl^-, and so distinct from the packing of the neutral molecule. Of the many pharmaceuticals where it is possible to obtain both neutral and salt forms, it seems that B5 and the morphinanes[7] are likely to be more typical in being strongly affected by the presence of the Cl^- ions, and to show considerable property variations with counterions when different salts are crystallized.[8] Cases where there is conservation of packing motifs between salt and neutral structures, such as the dimers in olanzapine[9] and levofloxacin,[7a] are likely to be unusual.

5. Computer modelling of solvates and derived structures

Computer modelling of B5HCl solvate structures was undertaken to assist in the characterization of the solvates and investigate their interrelationships. Computer modelling allows the substitution of smaller functional groups, or removal of solvate molecules, prior to minimisation. The methodology used for the CEL was supplemented by periodic DFT-D calculations.

5.1. Methodology: Dispersion corrected density functional theory calculations

In addition to the CrystalOptimizer calculations, we also performed computationally demanding periodic electronic structure calculations on the experimental and selected other solvates and computer generated models. Such calculations optimze all the atomic positions within the crystal, include the polarization effects and do not involve empirically fitted model potentials. The DFT-D calculations were carried out with the CASTEP plane wave code using the Perdew-Burke-Ernzerhof (PBE) generalized gradient approximation (GGA) exchange-correlation density functional and ultrasoft pseudopotentials, with the addition of the Tkatchenko and Scheffler (TS) or Grimme D2[10] semi-empirical dispersion corrections. Brillouin zone integrations were performed on a symmetrized Monkhorst–Pack k-point grid with the number of k-points chosen to provide a maximum spacing of 0.07 $Å^{-1}$ and a basis set cut-off of 780 eV. The self-consistent field convergence on total energy was set to $1x10^{-5}$ eV. Energy minimizations were performed using the Broyden–Fletcher–Goldfarb–Shanno optimizsation scheme within the space group constraints. The optimizations were considered complete when energies were converged to better than $2x10^{-5}$ eV per atom, atomic displacements converged to $1x10^{-3}$ Å, maximum forces to $5x10^{-2}$ eV $Å^{-1}$, and maximum stresses were converged to $1x10^{-1}$ GPa.

Isolated molecule minimizations to compute the isolated $B5H^+$ energies (Ugas) were performed by placing a single molecule in a fixed cubic 35x35x35 $Å^3$ unit cell and optimized and recalculated with the same settings as used for the crystal calculations. The N-H proton moved upon energy minimisation to the C=O oxygen. Therefore, no E_{latt} values are given for PBE-TS and PBE-D2 energy estimations in the following sections.

5.2. Modeling of dihydrate and its computational and experimental desolvation products

The computational models were both successful in reproducing the experimental Form I and dihydrate structures (Table S6).

Table S6. Quality of Representation of the Experimental form I and dihydrate structures.

	a/Å	b/Å	c/Å	β/°	PI	E_{latt}/kJ mol^{-1}	$rmsd_{15}$/Å	$rmsd_{15+}$/Å
Form I	9.4839	7.2873	24.0113	94.254				
PBE-TS	9.5162	7.2731	23.9611	93.926	72.3		0.048	0.050
CrystOpt	9.7393	7.1165	24.0050	84.964	71.7	-649.89	0.289	0.329
Dihydrate	20.4540	6.5304	13.5496	100.004				
PBE-TS	20.3320	6.5802	13.4806	99.409	74.9		0.068	0.086
CrystOpt	20.7218	6.5619	13.2037	100.5341	75.4	-764.29	0.195	0.262
Desolv(CO)	19.4391	6.8431	13.4471	109.8974	71.1	-637.83		

* compare to new form I (17018).

By manually removing water molecules from the DH structure and re-optimizing with CrystalOptimiser, the computationally desolvated DH (Figure S14) was optimized preserving the space group symmetry of the parent dihydrate to *ea*333 in the search.

In the dihydrate structure, water molecules act to bridge hydrogen-bonds between chloride ions and B5H$^+$ cations, resulting in a complicated 3D hydrogen-bonding network, among which there are $R_6^4(20)$, $R_4^4(12)$, $C_3^2(10)$, $C_3^2(11)$ motifs. When the water molecules were removed, the hydrogen-bonding network collapses, most of the motifs disappear, except for the $R_6^4(20)$ motif which transforms into an $R_4^2(16)$ motif. The collapse of the hydrogen bond network in the desolvated structure was accompanied by a significant shortening of the *a* axis by about 1 Å and an increase of cell angle β by almost 10°, as two B5H$^+$-Cl$^-$ pairs move closer to each other. The B5H$^+$ cation largely retained its original conformation in the computationally desolvated structure as in the dihydrate.

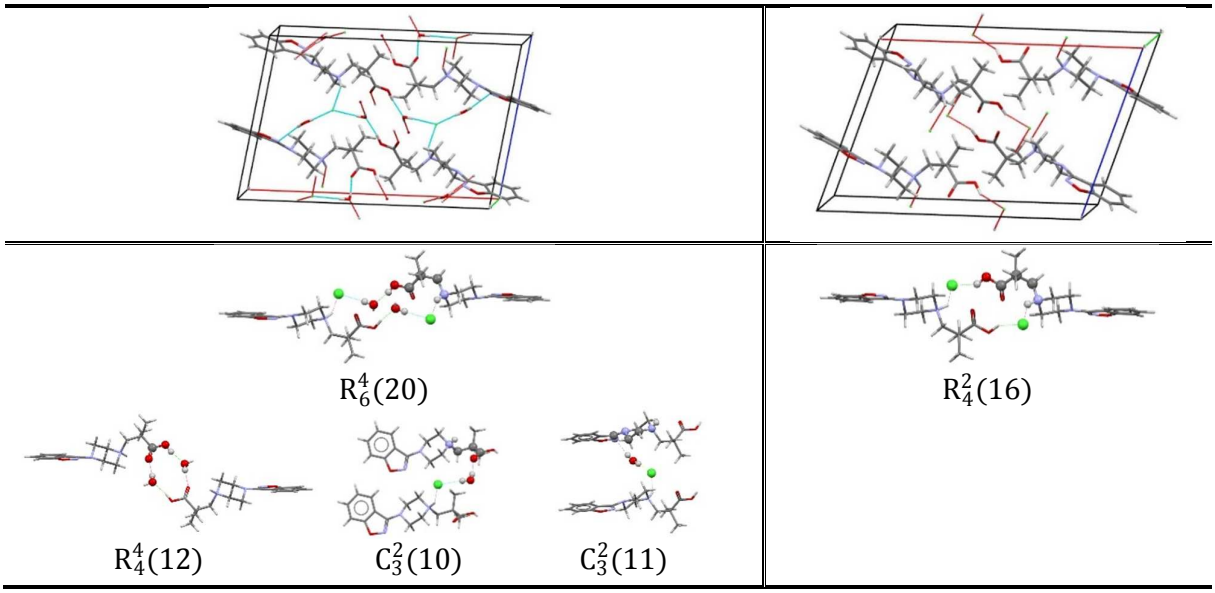

Figure S14. (Top) Comparison between the experimental B5HCl dihydrate structure (left) and its dehydrated structure (right) obtained by CrystalOptimizer optimisation after removing the water molecules; (Bottom) Hydrogen bonding motifs in B5HCl dihydrate (left) and its dehydrated structure (right). $R_6^4(20)$ in the dihydrate transforms into $R_4^2(16)$ motif upon dehydation, while the other 3 hydrogen bonding motifs will be lost.

5.3. Modelling of hemi-alcohol solvates and its computational dehydration products

The computational models were both successful in reproducing the experimental hemi-alcohol solvate structures (Table S7).

Table S7. Quality of Representation of the Experimental S-EtGly and S-PrGly structures.

	a/Å	b/Å	c/Å	β/°	E_{latt}/kJ mol^{-1}	$rmsd_{15}$ (Å)
S-EtGly (RT)	39.2019(16)	7.0831(2)	13.6181(4)	103.764(2)		
S-EtGly (100 K)	39.137(2)	7.0158(4)	13.5444(7)	103.948(2)		
PBE-TS (0 K)	39.2060	6.9071	13.5686	103.862		0.178
CrystOpt (0 K)	38.7114	7.0252	13.8632	104.0700	-1366.89	0.147*
Desolv (CrystOpt) (0 K)	39.9031	6.6683	13.3399	95.1578	-639.46	
S-PrGly (RT)	13.6663(8)	7.1511(2)	38.3118(31)	90		
S-PrGly (RT)	13.6770(3)	7.15140(10)	38.3289(7)	90		
PBE-TS (0 K)	13.6115	6.9828	38.4527	90.00		0.091
CrystOpt (0 K)	13.9503	7.1186	37.6214	90.00	-1361.91	0.131**
Desolv (CrystOpt) (0 K)	13.3373	6.6653	39.5372	90.00	-639.82	

*compared to the 100K structure. **compared to RT structure.

The two hemi-hydrate solvates show a two-dimensional structural similarity, a B5Cl double layer (Figure S15). Adjacent double layers are related by 2-fold symmetry in S-EtGly and by mirror plane in S-PrGly, leading to two distinct 3D packings. The common double layer, homochiral stacks of $B5H^+$ cations, is also present in the mono-alcohol structures with the exception of S-MeOH. The latter shows a distinct double layer. Adjacent double layers are again differently linked in the hemi-alcohols and mono-alcohols (Figure S16).

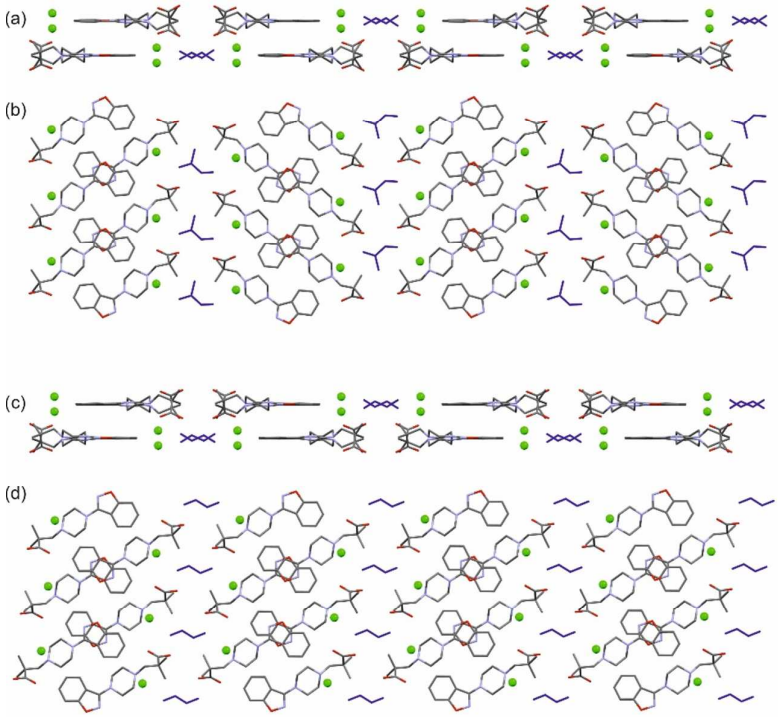

Figure S15. Packing diagrams of propylene glycol (a – viewed along *a*, b- viewed along *b*) and ethylene glycol solvates (c – viewed along *c*, d – viewed along *b*) showing the 2D structural similarity.

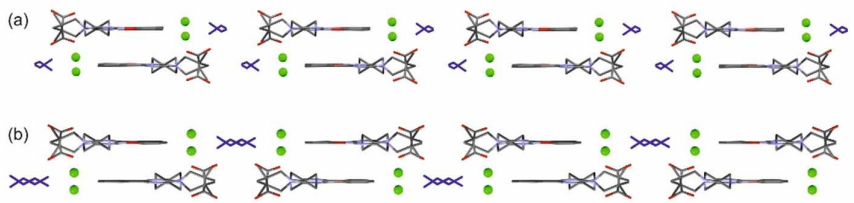

Figure S16. Packing diagrams of (a) ethanol and (b) propylene glycol solvates viewed along the *c* and *a* crystallographic axes, respectively showing the common 2D structural B5HCl layer motifs.

5.4. Modelling of the mono-alcohol solvates

The problems of experimentally obtaining suitable crystals for all of the alcohol solvates, despite the similarity of the PXRD patterns and the evidence for either the homo- or heterochiral 2D constructs of the $B5H^+$ Cl^- sheets (Figure S17), suggested that computer modelling should be able to propose the 3D alcohol solvate crystal structures.

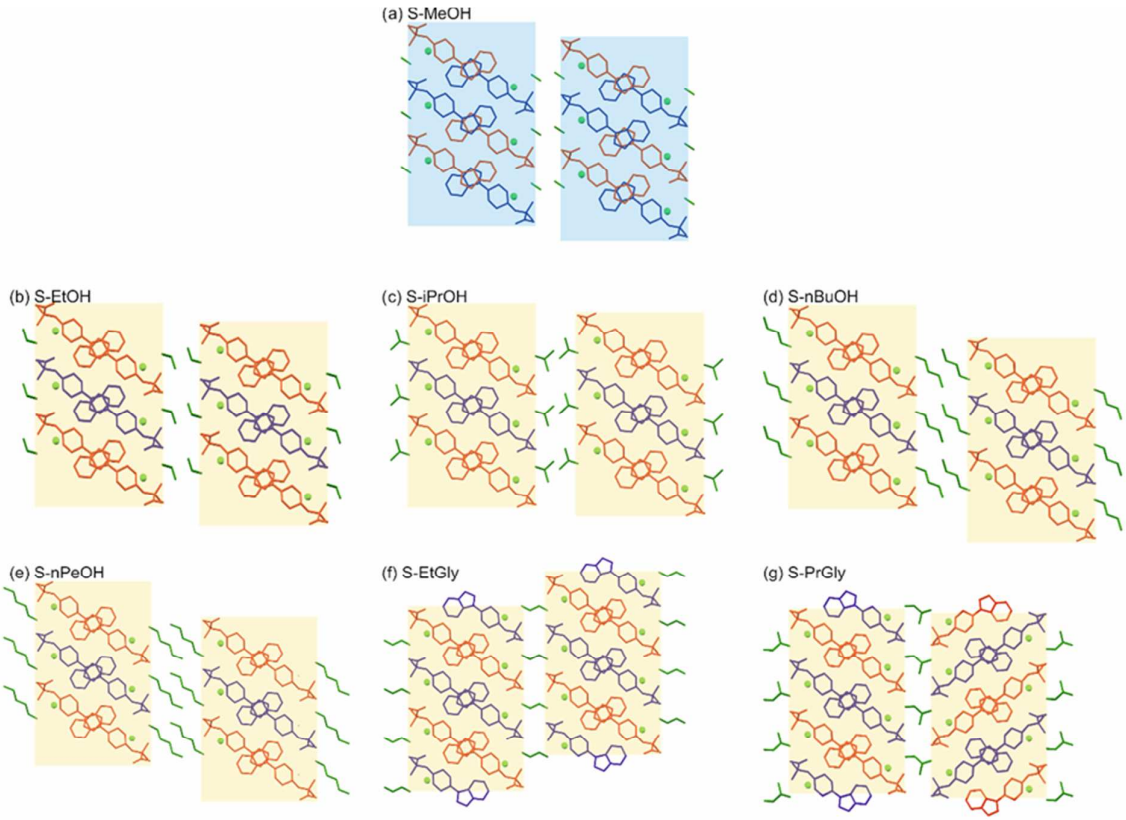

Figure S17. Packing diagrams of B5HCl alcohol solvates, showing the homo- and heterochiral stacks of $B5H^+$ molecules. Orientations of $B5H^+$: red COO^- pointing out, blue COO^- pointing into plane.

- First, we used the experimental S-MeOH and S-iPrOH solvates to help construct models for the other mono-alcohol solvates.

- Structure models for four solvates (S-EtOH, S-nBuOH, S-iBuOH and S-nPeOH) were derived and contrasted to their experimental structures which we were able to solve in parallel.
- For three of the mono-alcohol solvates (S-nPrOH, S-2BuOH and S-nOcOH) we were not able to grow single crystals suitable for laboratory SCXRD. Therefore, the computed structures were used to fill the gaps of missing experimental structures.
- Additionally, other hydrate/solvate structures were generated: S-tBuOH, S-nHexOH, S-HepOH, monohydrate and a mixed-alcohol solvate structure.

5.4.1. Modelling of S-MeOH and S-iPrOH and its computational and experimental desolvation

The i-PrOH and MeOH solvates exhibit differently stacked $B5H^+$ molecules and their computationally desolvated structures are different. For the i-PrOH solvate, the double-layers were well preserved in the desolvated structure, with $RMSD_{15+}$ = 0.282Å when compared to the i-PrOH solvate. The change of 3.7 Å in the *a* axis simply pulls two adjacent double-layers closer to each other. The computational desolvation of the methanol solvate results in a shearing of B5HCl double-layers and a slippage between stacked aromatic rings, as shown in Figure S18, such that the desolvated methanol solvate can only match 9 out of 15 molecules when compared with the original solvate. Two torsion angles in $B5H^+$ cation, ϕ1 and ϕ3, change more than 30 degrees. The significant changes in the desolvation of MeOH solvate, both in packing and molecular conformation, led to a substantially more stable structure by almost 38 kJ mol^{-1} than that of the desolvated i-PrOH solvate. This difference can be understood as the two desolvation optimizations started with different $B5H^+$ packings and different interlayer distances, so optimization within space group and translational symmetry constraints, proceeds along different pathways.

The desolvated methanol solvate was found in our search in the *ee* region as *ee*5411. It is 4.7 kJ mol^{-1} higher in lattice energy than that of the global minimum (*ee*860), and closely related to a few other structures in the low energy region, i.e. *ee*2270, *ee*3110 and *ee*4553, as Group c2 in Table S5. All four structures are composed of B5HCl double-layers.

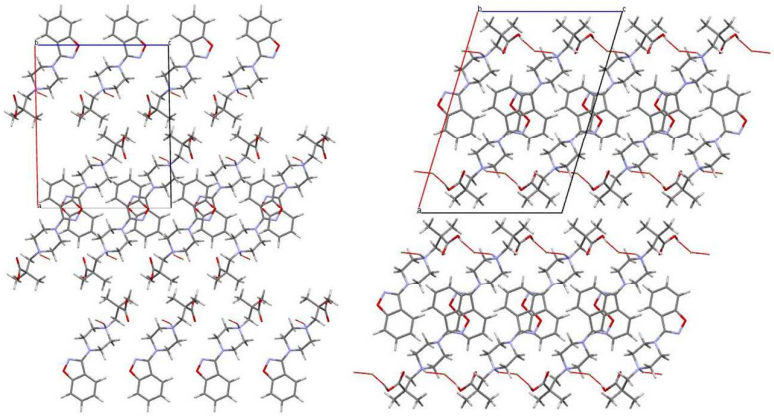

Figure S18. Comparison of desolvated i-PrOH (left) and MeOH (right) solvates of B5HCl.

In addition, the two solvate structures were minimized using CASTEP (PBE-TS) and experimental and computed structural information were compared.

For S-MeOH a solvate structure was generated differing from the experimental one in that the $B5H^+$ molecules stack in a homochiral fashion, instead of the heterochiral stacking arrangement. Figure **S19** shows a packing comparison for the two methanol solvate polymorphs.

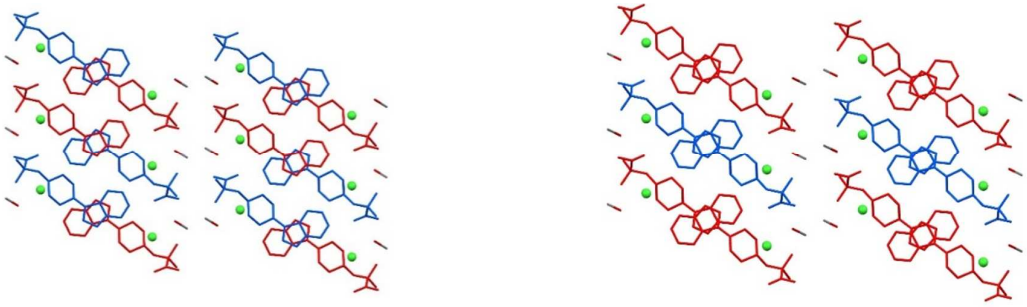

(a) S-MeOH (heterochiral stacks) (b) Methanol solvate (homochiral stacks)

Figure S19. Comparison of packing diagrams of (a) S-MeOH and (b) an alternative methanol solvate structure which is isostructural with S-EtOH. $B5H^+$ molecules drawn in red and blue: COO- pointing out and into plane, respectively.

The two (hypothetical) methanol solvate polymorphs differ by less than 2 kJ mol^{-1} in energy.

Furthermore, exemplarily for all alcohol mono-solvates, the two MeOH solvate structure models were combined into one structure (Figure S20).

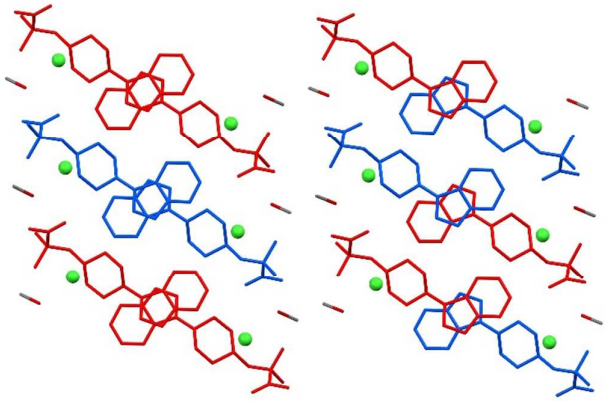

Figure S20. Packing diagram of a combined S-MeOH solvate structure having homo- and heterochiral $B5^+$ stacks. $B5^+$ molecules drawn in red and blue: COO^-pointing out and into plane.

A comparison of the simulated PXRD patterns, derived from the computer models using fixed lattice parameters (RT values derived from indexing the RT PXRD diffractograms) is shown in Figure S21. The three PXRD patterns are practically indistinguishable. Thus, based on PXRD data only it is not possible to deduce the packing of the solvate structure.

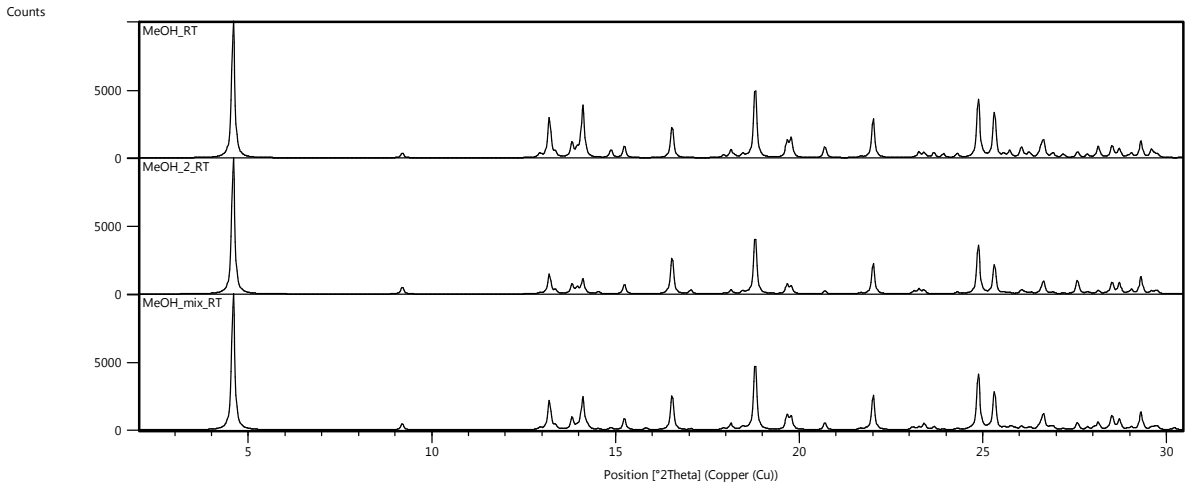

Figure S21. Comparison of computed (simulated) MeOH powder X-ray diffraction patterns. Structure minimizations were performed by optimizing atomic positions and fixing the lattice parameters to the S-MeOH RT values using CASTEP (PBE-TS). MeOH_RT – heterochiral packing, MeOH_2_RT – homochiral packing. MeOH_mix_RT – homo- and heterochiral packing arrangement.

The alcohol solvate packing models were contrasted to the computationally generated lowest energy structures. Structures *ee*2270 and *ee*3110 (Figure S22) show 2D packing similarity with all solvates except the S-MeOH. The isostructural S-MeOH solvate corresponds to *ee*5411 and S-MeOH shows 2D packing similarity with *ee*4553.

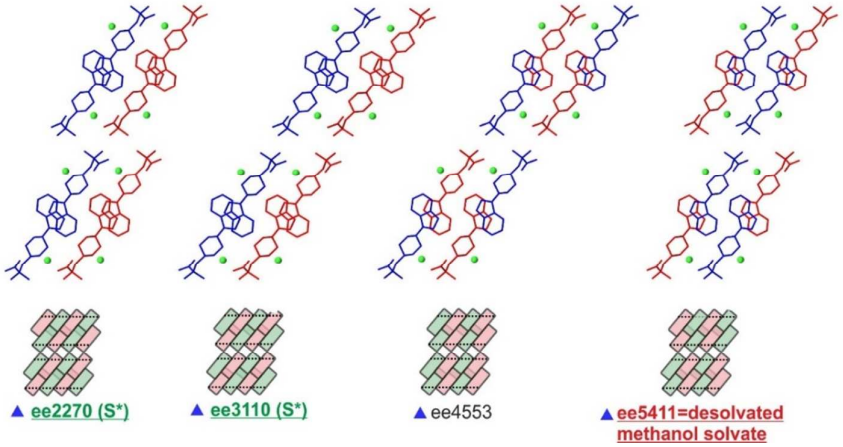

Figure S22. Comparison of packing possibilities of selected lowest energy structures adapting the same molecular conformation as observed in the solvates (c2 conformation, Figure 8).

The simulated PXRD patterns of the four structures *ee*2270, *ee*3110, *ee*4553 and *ee*5411 (Figure S23) indicate common structural features. Furthermore, the similarity in density and lattice energy (for selected structures) indicates the possibility for intergrowth/disorder. Thus, the computed anhydrate crystal energy landscape warns us that in the case of the formation of c2 chain layers (as seen in the solvates) disorder and stacking faults may occur.

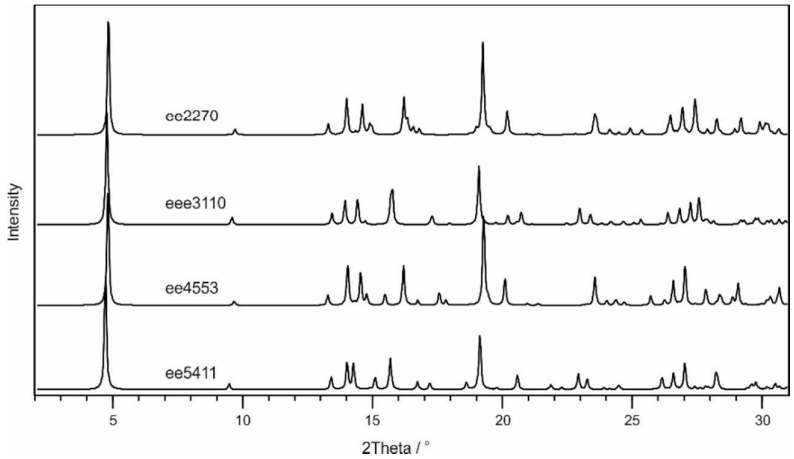

Figure S23. Comparison of computed (simulated) anhydrate c2 structures. Structure minimizations were performed by full structure optimisation (CASTEP).

Lattice energy differences (ΔE_{latt}) of the four c2 structures with respect to Form I are given in Table **S8**.

Table S8. Lattice energy differences / heat of transformations (ΔH_{trs}, measured with differential scanning calorimetry – see section 10) for experimental and selected computationally generated anhydrates.

ΔE_{latt} / $-\Delta H_{trs}$	Form I	Form II	*ea*333 (desolv DH)	*ee*2270	*ee*3110	*ee*4553	*ee*5411
CryOpt	0	11.26	13.58	-0.10	-0.04	2.45	3.03
PBE-TS	0	12.77	24.67	15.73	17.62	17.73	20.47
PBE-D2(sp)	0	19.05	22.20	15.57	16.02	17.30	18.51
DSC	0	8.5±0.3	–	–	–	–	–

5.4.2. Modelling to solve the EtOH solvate structure

Though single crystals of i-PrOH and MeOH solvate of B5HCl are readily grown, there were some persistent difficulties in preparing good diffraction-quality single crystals of other monoalcohol solvates. We have tried to rationalize this observation for the EtOH solvate with computational CSP methods. Starting from the experimental structure of the i-PrOH solvate, two models of EtOH solvate were constructed by removing one or the other of the two methyl groups in S-iPrOH. These were denoted as models EtOH_1 and EtOH_2. The two models were optimized with CrystalOptimizer, using the same degrees of freedom for the $B5H^+$ cation as in the pure form CSP search, additionally allowing two extra torsion angles (H-C-C-O, C-C-O-H) and one bond angle (COH) in ethanol to change under crystal packing forces.

The EtOH_2 model is 6.07 kJ mol^{-1} more stable than EtOH_1 model. A comparison of the optimized structures shows the different arrangement of solvent molecules, though in both cases ethanol forms hydrogen-bonds to the acid group and Cl^-, as shown in Figure S24, and the B5HCl framework is isostructural. However both EtOH structure models show that these are less densely packed compared to the MeOH and i-PrOH solvates (Figure S25 and Figure 12).

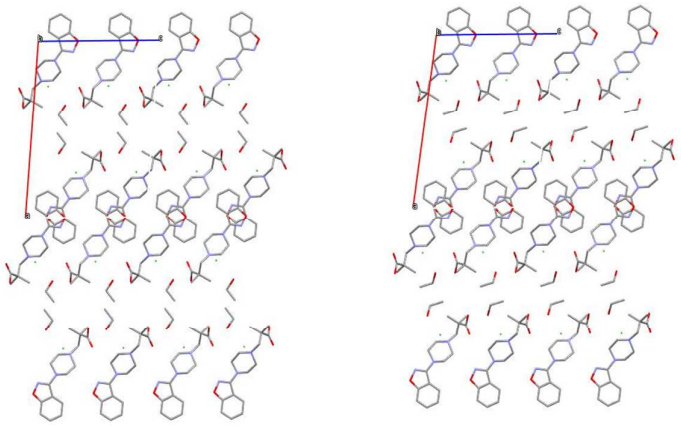

Figure S24. Two models for B5HCl ethanol solvates (left: EtOH_1, right: EtOH_2).

Unlike methanol, the alkyl tail of ethanol cannot fully embed inside the layers, yet while sticking out, terminal CH3 tail is not big enough to pack tightly as S-iPrOH, as shown in Figure S25. The existence of gaps could potentially provide enough "wiggling" room for solvent alkyl tails to cause disorder in the growing crystal and makes it difficult to grow large enough for a good quality single crystal.

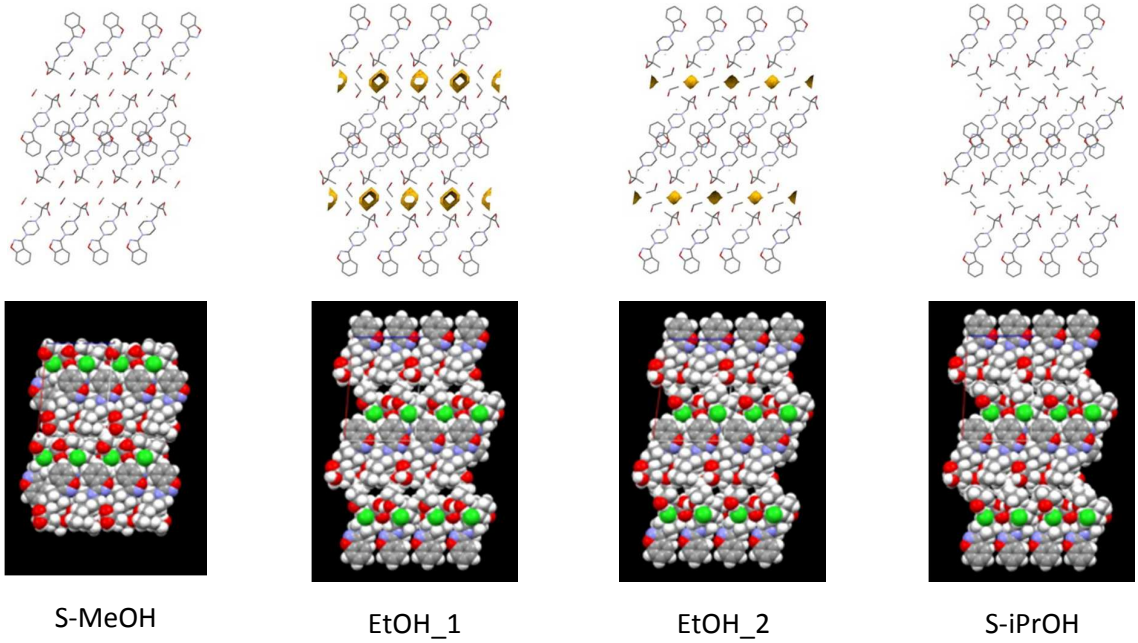

Figure S25. Packing comparisons of MeOH, (hypothetical) EtOH and i-PrOH solvate structures. Void space was calculated using Mercury (Version 3.9) with the orange surface in the wireframe view showing the closest contact possible for a probe of 1.0 Å radius.

In addition, CASTEP (PBE-TS) was applied to derive structure models for the ethanol solvate. Both, EtOH_1 and EtOH_2, were used as starting models. Furthermore, four disorder models were generated, covering EtOH_1:EtOH_2 ratios of 25:75, 75:25 and twice 50:50 (Figure S26). The structures were optimized, keeping the lattice parameters fixed at the RT values (indexed from

PXRD pattern: a = 20.8325(14) Å, b= 7.1543(1) Å, c = 13.6644(16) Å, β = 93.581(10)°, V = 2032.60(29) Å^3 and space group $P2_1/c$, Z′ = 1).

The six structure models (Figure S26) are indistinguishable if the solvent molecules are ignored. A disorder model (Figure S23c-f) was calculated to be slightly more stable than the two ordered models. Any disorder ratio of the ethanol molecule between the two orientations may be possible as there is no limitation in space in the solvate framework, c.f. iPrOH solvate with both "orientations" being occupied at the same time.

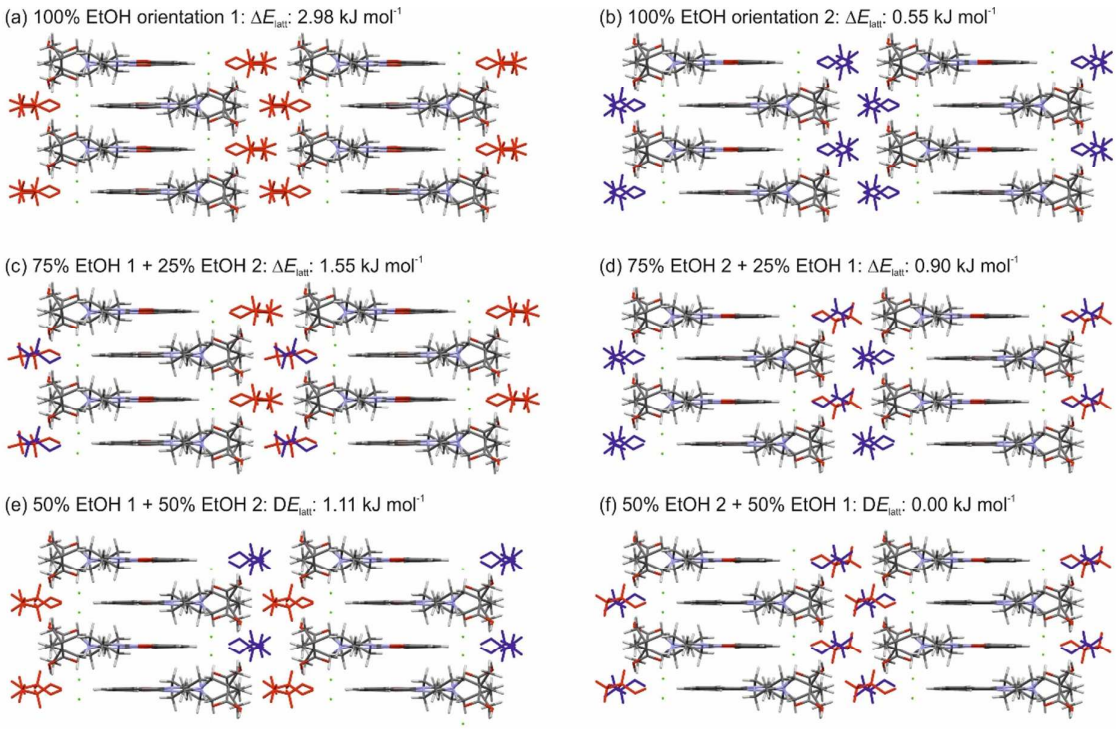

Figure S26. Packing diagrams of computationally generated ethanol solvate models differing in the orientation of the solvent molecules (indicated in red and blue) and ratios of the two orientations. Lattice energy differences were calculated relative to the most stable model (f) using CASTEP (PBE-TS).

After having derived the ethanol solvate models we were successful in solving the ethanol structure from SCXRD data. The 100 K structure solution had EtOH_2 present. A second structure determination at room temperature showed that the structure model differed from the low temperature determination in the size of the thermal ellipsoids of the hydrocarbon tail of the ethanol molecule. This is indicative of thermal movement of the alcohol hydrocarbon groups and can be supported by the calculations (Figure S26).

Furthermore, we investigated the possibility of a heterochiral ethanol solvate structure. The homochiral packing of EtOH_1, was calculated to be 3.14 (PBE-TS) to 3.65 (PBE-D2) more stable than the heterochiral packing, as observed as the dominant packing arrangement in S-MeOH. Based on the lattice energy calculations the presence of heterochiral B5H$^+$ domains in the homochiral S-EtOH structure cannot be excluded.

5.4.3. Modeling of the n-BuOH solvate

Eight n-butanol solvate models were constructed from the homochiral B5HCl n-PrOH solvate models (see section 5.4.6) by replacing one H atom on the $–CH_3$ group with an extra $–CH_3$ group. One of the starting models clashed (steric hindrance), thus only seven of the models were optimized using CASTEP (PBE-TS, Figure S29).

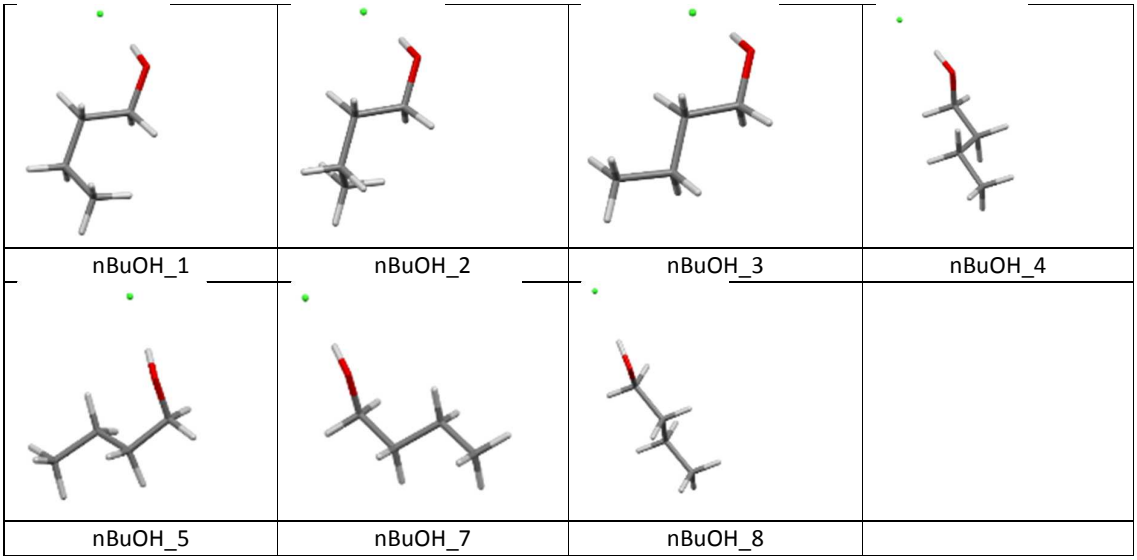

Figure S27. Comparison of *n*-BuOH conformations used as starting points for B5HCl *n*-BuOH solvate lattice energy minimizations.

Table S9. Comparison of lattice energy differences relative to the lowest energy structure calculated using different methods. The lowest energy structure is highlighted in green.

Structure	ΔE_{latt} / kJ mol^{-1} PBE-TS (opt)	ΔE_{latt} / kJ mol^{-1} PBE-D2 (sp)
nBuOH_1	8.77	5.71
nBuOH_2	17.29	11.21
nBuOH_3	0.00	0.00
nBuOH_4	17.42	11.99
nBuOH_5	21.45	20.27
nBuOH_7	16.02	12.07
nBuOH_8	20.92	12.34

The lowest energy n-BuOH solvate model (Figure S28) closely matches the experimental powder pattern (solvate reflections), ignoring the anisotropic thermal effects (Figure S29).

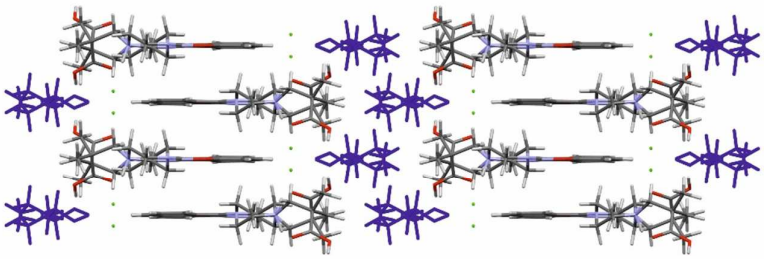

Figure S28. Packing diagram of the computationally generated lowest energy n-BuOH solvate structure.

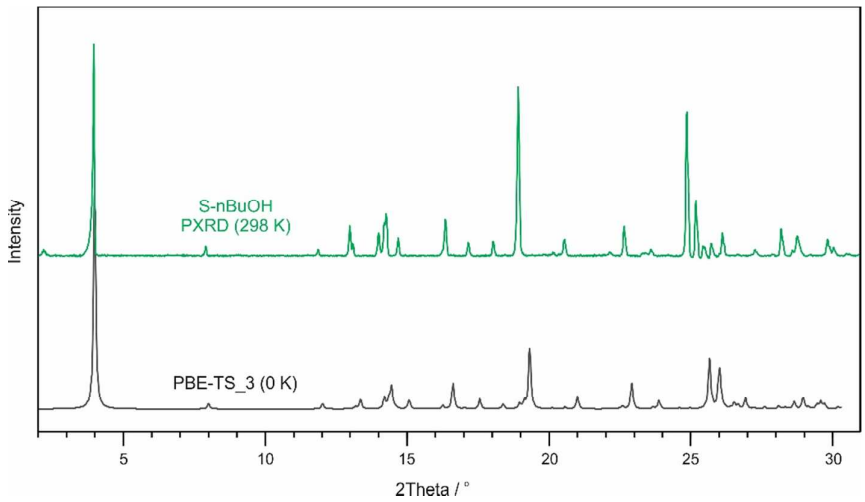

Figure S29. Comparison of the experimental and computed, simulated from nBuOH_3 structure, powder X-ray diffraction patterns. Structure minimisations were performed by optimising lattice parameters and atomic positions using CASTEP (PBE-TS).

The *n*-BuOH solvate PXRD pattern was successfully indexed to a monoclinic unit cell with $P2_1/c$ symmetry and following lattice parameters: a=22.6813(19) Å, b=7.1622(2) Å, c=13.6973(6), β=99.110(3)°. The experimental cell (room temperature) matches the 0 K cells derived for the lowest energy structure model, under neglecting thermal effects (Table S10). The n-butanol structure 3 (nBuOH_3) was later confirmed to be the experimental structure.

Table S10. Experimental nBuOH solvate lattice parameters are contrasted to 0 K lattice parameters of structure model nBuOH_3.

Method	a / Å	b / Å	c / Å	β / °	Volume / Å^3
PXRD (RT)	22.6813(19)	7.1622(2)	13.6973(6)	99.110(3)	2197.04(23)
PBE-TS (0 K)_3	22.395	6.941	13.615	100.04	2084.04

5.4.4. Modelling of the i-BuOH solvate

Six i-butanol solvate models were constructed using the *n*-PrOH models as starting points, by manually replacing one H atom on the –CH_3 groups with an extra –CH_3 group (Figure S30). The six starting models were optimised using CASTEP (PBE-TS).

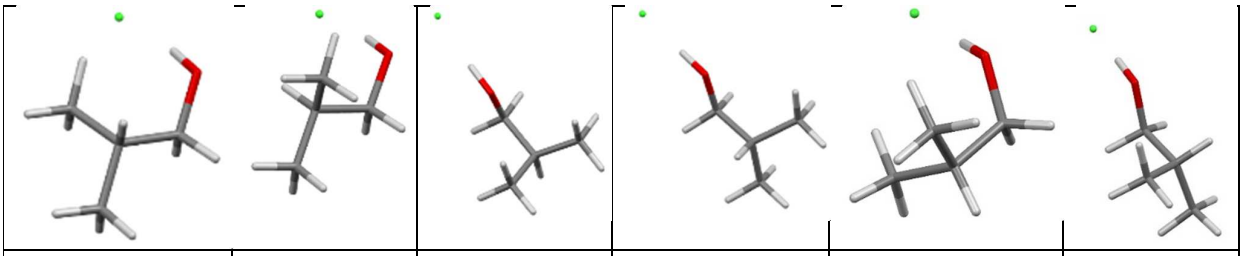

Figure S30. Comparison of *i*-BuOH orientations used as starting points for B5HCl *i*-BuOH solvate lattice energy minimizations.

Three of the i-BuOH solvate structures were found within 5 kJ mol^{-1} of the lowest energy structure (iBuOH_4) using both TS and D2 (sp: single-point energy) for optimization (Table S11). The structure models are isostructural (Figure S31) apart from the orientation of the CH tail of the solvent molecule.

Table S11. Comparison of lattice energy differences relative to the lowest energy structure calculated using different methods. Lowest energy structures are highlighted in green.

Structure	ΔE_{latt} / kJ mol^{-1} PBE-TS (opt)	ΔE_{intra} / kJ mol^{-1} PBE-D2(sp)
i-BuOH_1	4.96	8.35
i-BuOH_2	8.05	7.52
i-BuOH_3	4.98	3.92
i-BuOH_4	0	0
i-BuOH_5	9.61	8.89
i-BuOH_6	3.33	1.83

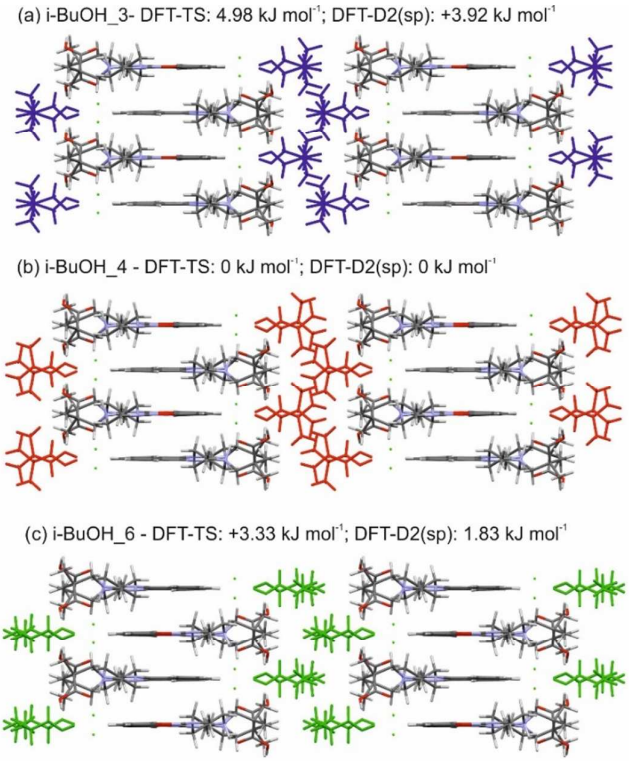

Figure S31. Packing diagrams of computationally generated i-BuOH solvate models differing in the orientation of the solvent molecules (indicated in red, blue and green). Lattice energy differences were calculated relative to the most stable model.

The i-BuOH PXRD pattern indexed to a monoclinic unit cell with $P2_1/c$ symmetry and following lattice parameters: a=23.6864(24) Å, b=7.1530(2)Å, c=13.6322(7), β=105.244(4)°. The experimental cell (room temperature) matches the 0 K cells derived for the lowest energy structure model, under neglecting thermal effects (Table S12). The two experimental solvate structure solutions, one of which is included in Table S1, correspond to solvate models 4 and 6, respectively.

Table S12. Experimental i-BuOH solvate lattice parameters are contrasted to selected 0 K lattice parameters of structure models.

Method	a / Å	b / Å	c / Å	β / °	Volume / Å^3
PXRD (RT)	23.6864(24)	7.1530(2)	13.6322(7)	105.244(4)	2228.42(27)
PBE-TS (0 K)_3	22.7717	6.9751	13.5965	103.787	2097.38
PBE-TS (0 K)_4	22.7737	6.8941	13.5397	92.265	2124.13
PBE-TS (0 K)_6	23.7547	6.9361	13.3854	105.077	2129.53

5.4.5. Modelling of the n-PeOH solvate

Three n-pentanol solvate models were constructed from the B5HCl n-BuOH_3 solvate model, by replacing one H atom on the –CH_3 group with an extra –CH_3 group (Figure S32). Lattice energy differences with respect to the most stable of the three models are given in Table S13.

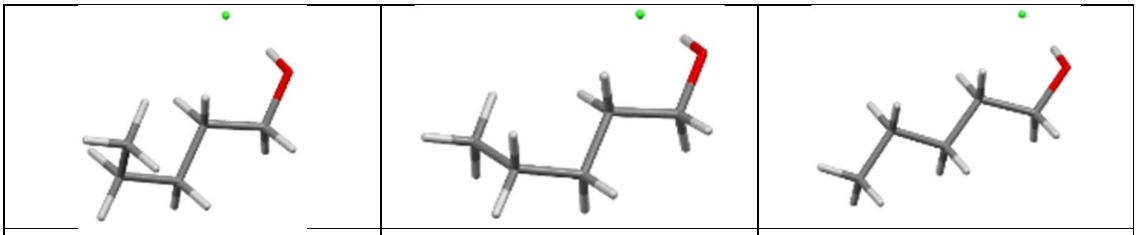

Figure S32. Comparison of nPeOH orientations used as starting points for B5HCl n-PeOH solvate lattice energy minimizations.

Table S13. Comparison of lattice energy differences relative to the lowest energy structure calculated using different methods.

Structure	ΔE_{latt} / kJ mol^{-1} PBE-TS (opt)	ΔE_{intra} / kJ mol^{-1} PBE-D02 (sp)
1-PeOH_1	18.61	13.31
1-PeOH_2	4.35	1.04
1-PeOH_3	0.00	0.00

A packing comparison of the two lowest energy computationally generated *n*-PeOH solvate structures shows that the structures are isostructural apart from the orientation of the hydrocarbon tail of the *n*-PeOH molecule. The small lattice energy differences, estimated using different methods, and isostructurality of the B5HCl frameworks may indicate the possibility of disorder of the solvate molecule (not necessarily of the conformational variety seen in Figure S33).

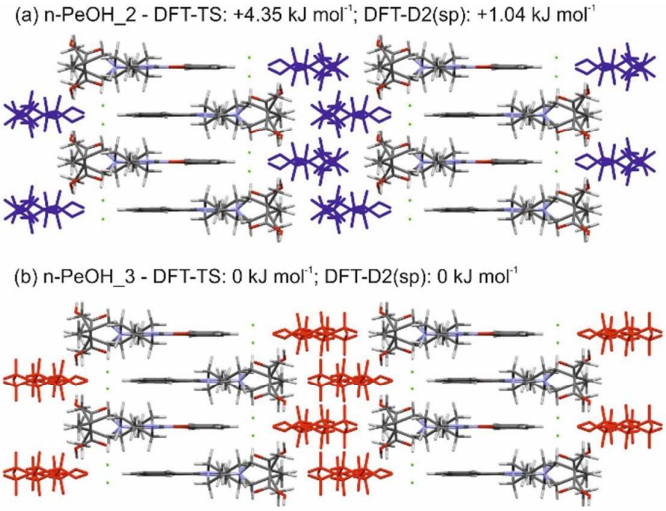

Figure S33. Packing diagrams of computationally generated n-PeOH solvate models differing in the orientation of the solvent molecules (indicated in blue, blue and red). Lattice energy differences were calculated relative to the most stable model.

The n-PeOH PXRD pattern indexed to a monoclinic unit cell with $P2_1/c$ symmetry and following lattice parameters: a=23.9611(16) Å, b=7.1818(2) Å, c=13.6823(12), β=99.797(7)°. The experimental cell (room temperature) matches the 0 K cells derived for the lowest energy structure model, under neglecting thermal effects (Table S14). The lowest energy n-PeOH structure model was later identified as the main domain in the experimental structure.

Table S14. Experimental n-PeOH solvate lattice parameters are contrasted to 0 K lattice parameters of structure models n-PeOH_2 to n-PeOH_3.

Method	a / Å	b / Å	c / Å	β / °	Volume / Å^3
PXRD (RT)	23.9611(16)	7.1818(2)	13.6823(12)	99.797(7)	2320.16(28)
PBE-TS (0 K)_2	22.8430	6.9898	13.7695	99.322	2169.51
PBE-TS (0 K)_3	23.3837	6.9532	13.6417	102.982	2161.36

5.4.6. Modelling of the n-PrOH solvate

The n-PrOH PXRD pattern was successfully indexed at room temperature to a monoclinic unit cell with $P2_1/c$ symmetry and following the lattice parameters: *a*= 22.7810(12) Å, *b*=7.1269(4) Å, *c*=13.6760(10), β=101.572(8)°. Twelve n-PrOH solvate models were constructed from the experimental crystal structures of S-iPrOH (6 structures, S-nPrOH_*x*homo) and S-MeOH (6 structures, S-nPrOH_*x*het) by either manually replacing one H atom on one of the two $-CH_3$ groups with a $-CH_3$ group or replacing one $-CH_3$ solvent H atom with a $-CH_2CH_3$ group of S-MeOH. The twelve starting models were optimized using CASTEP (PBE-TS and PBE-D2, Table S15 & Figure S34). 0 K models were derived by optimizing in addition to the atomic positions also the lattice parameters, whereas for the RT optimizations only the atomic positions were optimized in fixed unit cells. It has to be noted that the RT lattice parameters are average values and crystal-to-crystal variability in lattice parameter due to disorder can be expected as seen for S-MeOH and s-iPrOH.

Huge differences in the stability order of lattice energies were observed between RT and 0 K models. The latter can be attributed to the fact that certain 0 K structures differ significantly in lattice parameters. Room temperature optimizations S-nPrOH_1homo, S-nPrOH_2homo and S-nPrOH_2homo differ in $B5^+$ stacks from the experimental solvate structures and other S-nPrOH models, leading to higher lattice energies. The S-nPrOH_1het 0 K and RT structures differ in the location of the solvate molecule.

Interestingly, structure models showing different stacks of $B5H^+$ conformational enantiomers (homo- vs. heterochiral) and different solvent molecule orientations are among the lowest energy structures at 0 K and RT (Table S15). Based on lattice energy calculations, the S-nPrOH_6homo (homochiral $B5H^+$ stacks) may be seen as the most likely S-nPrOH packing with other structure models being likely to be present as domains, as seen for S-MeOH (Figure 8).

Neither a comparison of the experimental PXRD nor ss-NMR data with the simulated data derived from the solvate models (see section C) allowed us to unambiguously conclude which $B5H^+$ stacking or solvate orientation is present in the experimental solvate. A mixture of the structure models presented in Figure S34 is likely.

Table S15. Comparison of lattice energy differences relative to the lowest energy structure calculated using different methods.

	0 K[a]		RT[b]	
	PBE-TS	PBE-D2 (sp[c])	PBE-TS	PBE-D2
Structure model	ΔE_{latt} (kJ mol^{-1})			
S-nPrOH_1homo	4.76	3.66	30.34	21.67
S-nPrOH_2homo	12.11	7.17	29.56	19.90
S-nPrOH_3homo	1.66	0.99	11.44	10.24
S-nPrOH_4homo	11.96	6.88	0.47	0.50
S-nPrOH_5homo	22.65	15.03	10.61	3.64
S-nPrOH_6homo	3.36	0.00	0.00	0.32
S-nPrOH_1het	0.00	1.83	46.83	45.65
S-nPrOH_2het	5.58	3.04	7.55	2.86
S-nPrOH_3het	6.61	3.64	2.31	0.00
S-nPrOH_4het	17.01	10.99	2.79	1.52
S-nPrOH_5het	26.40	16.60	7.54	0.66
S-nPrOH_6het	23.45	15.82	2.70	0.22

[a] Optimization of atomic positons and lattice parameters. [b] Optimization of atomic poisons, but keeping the experimental room temperature (RT) lattice parameters fixed. [c] Single point calculations using fixed lattice parameters and fixed atomic positions (based on PBE-TS structures).

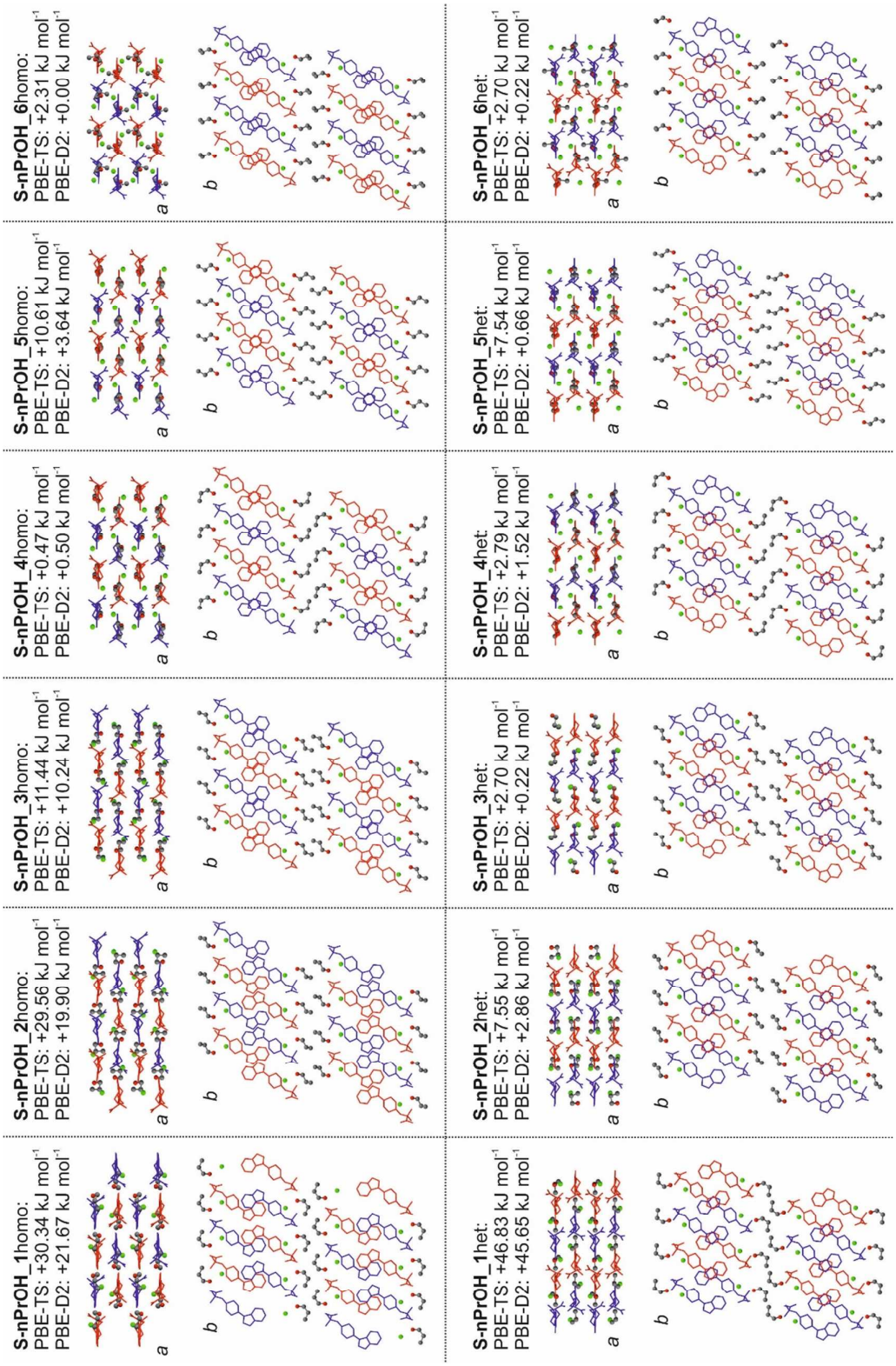

Figure S34. Room temperature structure model for S-nPrOH, which feature heterochiral and homochiral stacking of $B5H^+$ conformational enantiomers (shown in red and blue) and different orientations of the solvent (nPrOH) molecules. Cl^- atoms and nPrOH molecules are shown as 'ball and stick' and H-atoms are omitted for clarity.

5.4.7. Modelling of the 2-BuOH solvate

The 2-BuOH PXRD pattern indexed to a monoclinic unit cell with $P2_1/c$ symmetry and following lattice parameters: a=22.4726(16) Å, b=7.1572(2) Å, c=13.6931(6), β=90.817(3), room temperature.

Twelve S-2BuOH solvate models were constructed using the *n*-PrOH models as starting points by manually replacing one H atom on the $–CH_3$ groups with an extra $–CH_3$ group. The twelve starting models were optimized using CASTEP (PBE-TS and PBE-D2, Table S16 and Figure S35) and consist of six structures showing homochiral $B5H^+$ and six structures showing heterochiral $B5H^+$ stacks.

Independent of the applied dispersion correction (TS or D2) and the temperature (0 K or RT) the structure model S-2BuOH_5het, heterochiral B5+ stacks, was calculated to be the lowest in lattice energy. Albeit other packings, homochiral stacks, and/or different 2-BuOH molecular conformations were calculated to be close in energy, indicating the possibility of domains of alternate packings in S-2BuOH_5het.

Similar to the S-nPrOH, neither a comparison of the experimental PXRD nor ss-NMR data with the simulated data derived from the solvate models allowed us to conclude which $B5H^+$ stacking or solvate orientation is present in the experimental solvate. Based on the lattice energy calculations disorder, stacking faults and/or different solvent molecule orientations, seems to be likely.

Table S16. Comparison of lattice energy differences relative to the lowest energy structure calculated using different methods.

	0 K[a]		RT[b]	
	PBE-TS	PBE-D2 (sp[c])	PBE-TS	PBE-D2
Structure model	ΔE_{latt} (kJ mol^{-1})			
S-2BuOH_1homo	3.04	1.66	10.40	7.91
S-2BuOH_2homo	16.28	12.77	13.66	9.79
S-2BuOH_3homo	13.03	9.80	22.37	13.42
S-2BuOH_4homo	5.48	4.03	13.49	9.53
S-2BuOH_5homo	1.10	0.80	6.77	5.08
S-2BuOH_6homo	12.56	14.97	24.87	22.27
S-2BuOH_1het	2.11	2.08	9.13	4.78
S-2BuOH_2het	11.62	6.75	17.85	12.32
S-2BuOH_3het	19.19	14.71	40.08	21.56
S-2BuOH_4het	13.67	9.39	4.05	3.64
S-2BuOH_5het	0.00	0.00	0.00	0.00
S-2BuOH_6het	29.43	25.89	25.09	23.33

[a] Optimization of atomic positons and lattice parameters. [b] Optimization of atomic poisons, but keeping the experimental room temperature (RT) lattice parameters fixed. [c] Single point calculations using fixed lattice parameters and fixed atomic positions (based on PBE-TS structure).

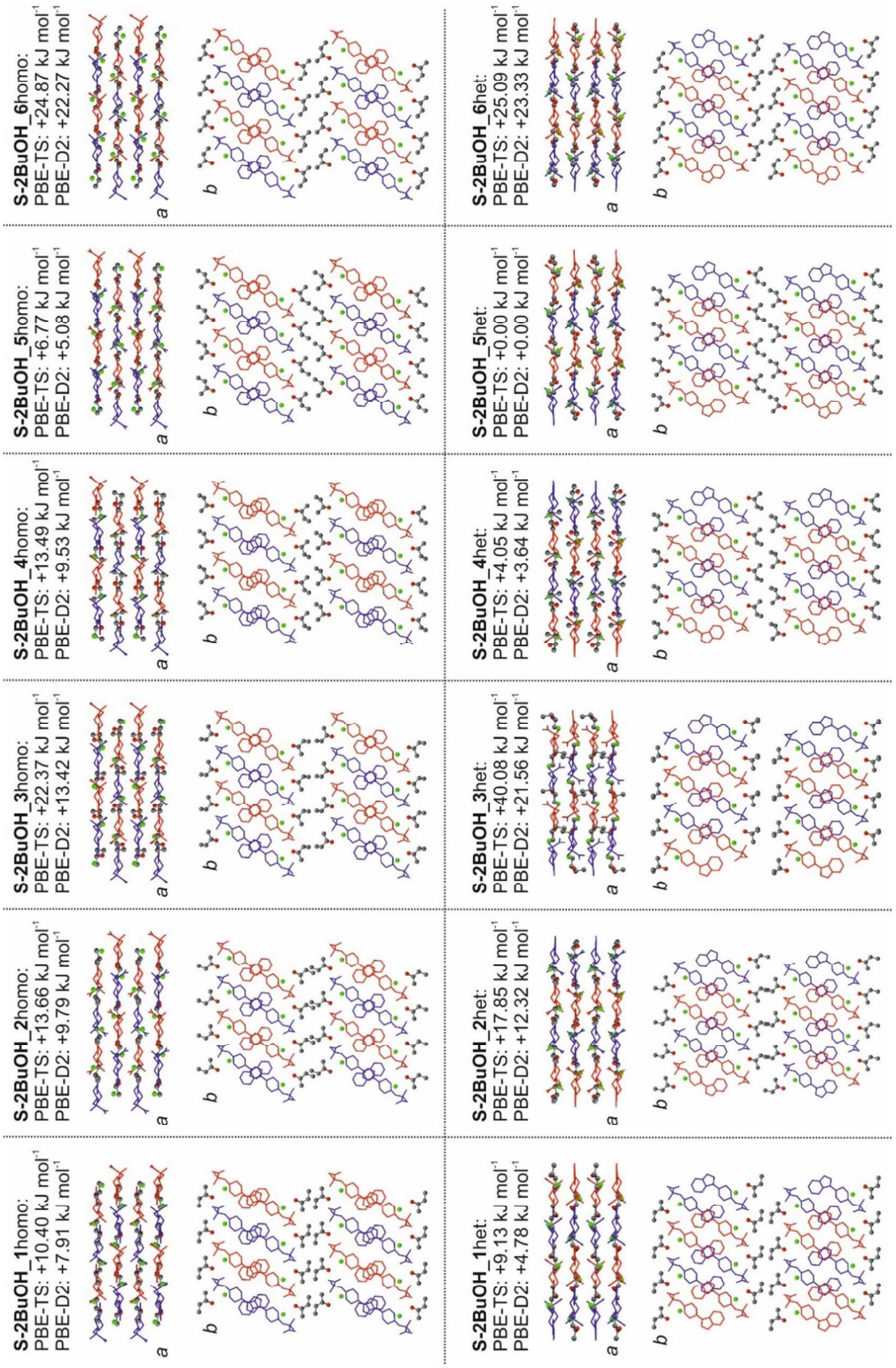

Figure S35. Room temperature structure model for S-2BuOH, which feature heterochiral and homochiral stacking of $B5^+$ conformational enantiomers (shown in red and blue) and different orientations of the solvent (nPrOH) molecules. Cl^- atoms and nPrOH molecules are shown as 'ball and stick' and H-atoms are omitted for clarity.

5.4.8. Modelling of the n-HexOH, n-HepOH and n-OcOH solvates

For n-hexanol, n-heptanol and n-octanol each one model was constructed by manually adding $-CH_3$ groups to the n-pentanol molecule and optimizing the structure (Figure S39). No disorder modelling was attempted for the three solvate types. The three solvate models show homochiral stacks of $B5H^+$ molecules.

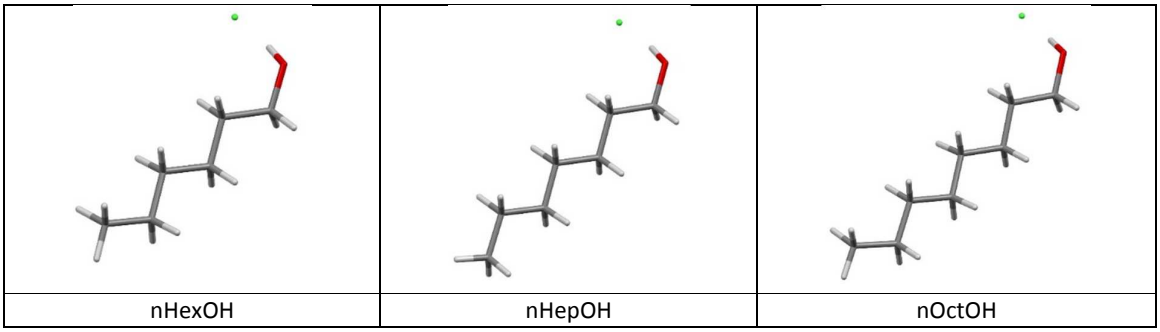

Figure S36. Comparison of n-HexOH, n-HepOH and n-OcOH extended orientations used as starting points for B5HCl solvate lattice energy minimisations.

The n-HexOH and n-HepOH structures were used as intermediates to propose the S-nOcOH structural model. The packing diagrams (Figure S37) of the three computed B5HCl alcohol solvate structures indicate that the B5HCl layers are maintained and that the three solvate structures mainly differ, as expected, in the length of the *a* crystallographic axis due to the different number of solvent carbon atoms (Table S17).

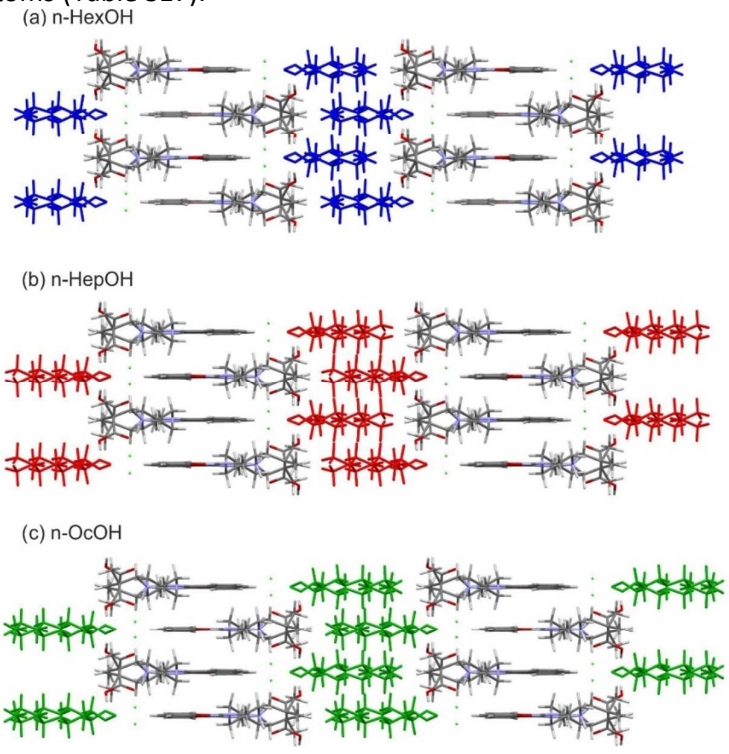

Figure S37. Packing diagrams of computationally generated n-HexOH (a), n-HepOH (b) and n-OcOH (c) solvate models.

The PXRD pattern of the S-nOcOH solvate indexed to a monoclinic unit cell with $P2_1/c$ symmetry and following lattice parameters: a=26.9672(13) Å, b=7.2014(2) Å, c=13.7024(9), β=103.794(3)°. The experimental cell (room temperature) matches the 0 K cells derived for the lowest energy structure model, under neglecting thermal effects (Table S17).

Table S17. Experimental n-OcOH solvate lattice parameters are contrasted to 0 K lattice parameters of structure models of B5HCl n-OcOH, n-HepOH and n-HexOH monoalcohol solvates.

Method	a / Å	b / Å	c / Å	β / °	Volume / Å^3
S-nOcOH (RT)	26.9672(13)	7.2014(2)	13.7024(9)	103.794(3)	2548.29(24)
S-nOcOH (0K)	26.8366	6.9153	13.5549	104.356	2437.01
S-nHepOH (0K)	25.7158	6.9523	13.6030	105.160	2347.36
S-nHexOH (0K)	24.7295	6.9183	13.5917	103.287	2263.1

For S-nOcOH an additional solvate model showing heterochiral B5H$^+$ stacks was constructed. Based on the lattice energy difference of 5.9 kJ mol^{-1} (PBE-D2) between the two 0 K optimizations a domain structure (disorder) is plausible.

5.4.9. Computationally generated t-BuOH structure

A solvate model was constructed from the experimental crystal structure of the B5HCl i-PrOH solvate, by manually removing the H atom on C1 and replacing it with an extra –CH_3 group. The minimized packing (PBE-TS, Figure S35) was found to be isostructural with the other homochiral mono-alcohol solvates. The 0 K lattice parameters of the Z'=1, $P2_1/c$ structure were calculated as follows: a=22.3726 Å, b=6.9966 Å, c=13.5211 Å, β=91.304°. Experimentally we were not able to produce the t-BuOH solvate of B5HCl. The calculated packing index of the t-BuOH solvate structure was within the range of the observed structures.

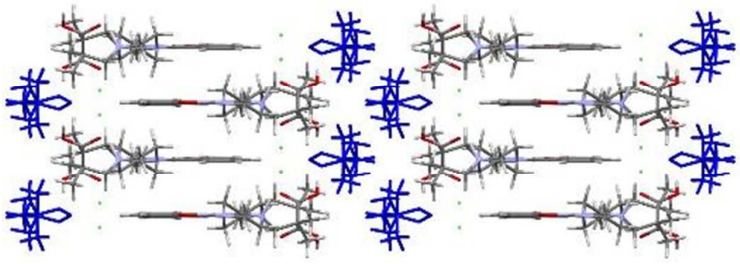

Figure S38. Packing diagram of a computationally generated t-BuOH solvate structure.

5.4.10. Computationally generated monohydrate structures

By replacing the solvent molecule in the MeOH (heterochiral stacks) and EtOH (homochiral stacks) solvate structure with water we investigated the possibility whether isostructural monohydrate packings could be produced at least computationally. To derive the starting model the methanol –CH_3 or ethanol –CH_2–CH_3 groups were replaced by an H atom. The packing diagrams of the optimised (PBE-TS) structures shows isostructurality with the S-MeOH and other mono-alcohol

solvates (Figure S39a&b) and the water molecule shows three strong hydrogen bonds, two to adjacent COOH functional groups and one to the Cl^- ion (Figure S39c&d). In Figure S39c (MH_in_MeOH) water and one carboxylic acid oxygen atom form a tetrameric ring motif, whereas in Figure S39d (MH_in_EtOH) the same two atoms form a chain propagating along the 2_1 screw axis.

The two monohydrate models differ by 1.40 (PBE-TS) and 1.69 (PBE-$D2_{sp}$) kJ mol^{-1} in lattice energy, with the MH_in_MeOH packing being slightly more stable. The packing indices of the two monohydrates (74.0 and 74.6) are close to the packing index of the calculated DH structure (74.9, 0 K) and higher than for Form I (72.3, 0 K).

Experimentally, the hypothetical monohydrate was not observed which may be related to the fact that the solvates readily desolvate to Form I and that a stable B5HCl dihydrate structure exists.

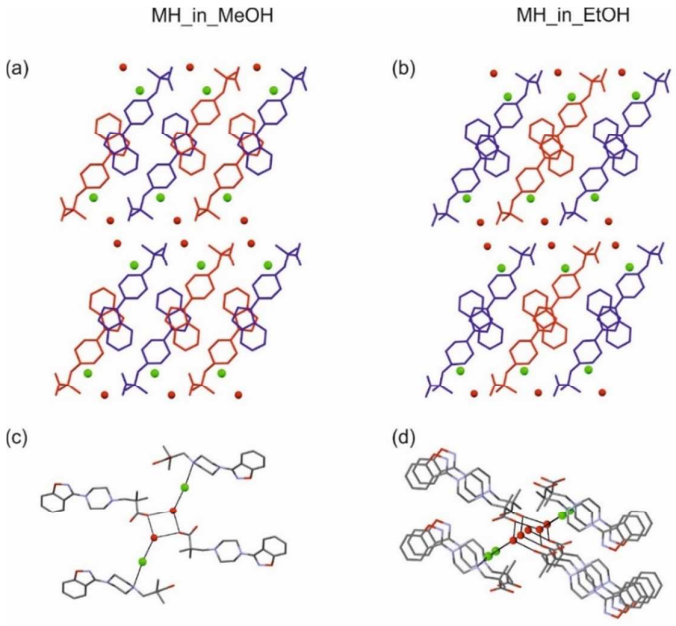

Figure S39. Packing diagram of a hypothetical monohydrate structures: (a) isostructural with S-MeOH and (b) isostrucural with S-EtOH. Hydrogen bonding motfs are given in (c) and (d), with (c) corresponding to MH_in_MeOH and (d) to MH_in_EtOH.

According to equations (1) and (2), a simple estimation of $\Delta_{dehy}U_{Hy\text{-}AH}$ and $\Delta_{trs}U_{Hy\text{-}AH}$ can be made by comparing the lattice energy, E_{latt}, of the hydrate to those of the anhydrate and ice:

$$\Delta_{dehy}U_{Hy-AH} = -E_{latt(Hy)} - (-E_{latt(AH)}) \quad (1)$$

$$\Delta_{trs}U_{Hy-AH} \approx \Delta_{dehy}U_{Hy-AH} - n(-E_{latt(ice)}) \quad (2)$$

Using the lattice energies of the experimental hydrate and anhydrate structures and a value of -59 kJ mol^{-1} [11] for ice (the used functional is known to overbind the ice crystal structures) $\Delta_{trs}U_{Hy\text{-}AH}$ was calculated to be 26.79 kJ mol^{-1} for DH and 10.22/8.82 kJ mol^{-1} for the hypothetical MH (based on MeOH/EtOH structure). Based on the lattice energies DH was estimated to be more stable than MH.

Table S18. Computed heat of dehydration ($\Delta_{dehy}U_{Hy\text{-}AH}$) and hydrate to anhydrate transformation enthalpy ($\Delta_{trs}U_{Hy\text{-}AH}$).

	E_{CASTEP} (kJ/mol)	Mol water	$\Delta_{dehy}U_{Hy\text{-}AH}$ (kJ/mol)	$\Delta_{trs}U_{Hy\text{-}AH}$ (kJ/mol)
AH	-517848.37	0		
DH	-608467.40	2	144.79	26.79
MH (in MeOH)	-563154.71	1	69.22	10.22
MH (in EtOH)	-563153.31	1	67.82	8.82

5.4.11. Computationally generated Perfect Mixed Crystal: S-EtOH2 and S-iPrOH

A mixed crystal structure of S-EtOH2 and S-iPrOH (ratio 1:1) was constructed and full structure optimization was applied (Figure S40).

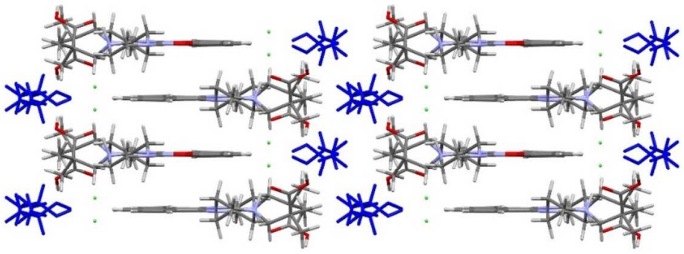

Figure S40. Packing diagram of the computationally generated 1:1 perfect mixed crystal of S-EtOH2 and S-iPrOH.

The PXRD pattern simulated from the calculated structure is compared to the simulated patterns of S-EtOH2 and S-iPrOH in Figure S41. The three simulated powder pattern show high resemblance and concluding whether a mixed crystal or "pure" solvate is present may not be possible based on powder diffraction data only. It has to be noted that the simulated patterns do not suffer from preferred orientation effects.

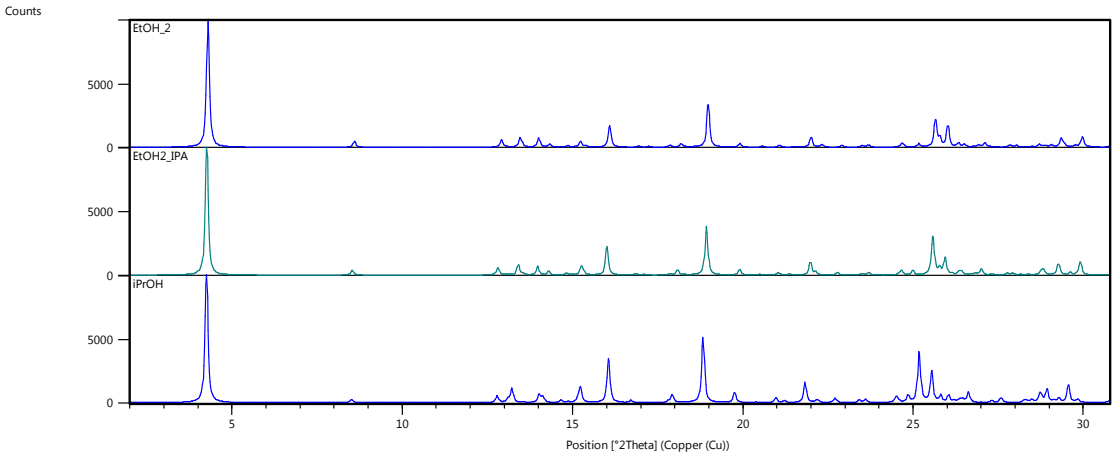

Figure S41. Comparison of simulated S-EtOH2 (top), a mixed S-EtOH2 and S-iPrOH structure (mixed EtOH2_IPA) and S-iPrOH (bottom) powder X-ray diffraction patterns. Structure minimizations were performed by optimizing atomic positions and lattice parameters using CASTEP (PBE-TS).

5.5. Overview - Modelling of mono-alcohol solvates: reproduction of the best experimental model of the solvate crystal structures, by the various computational models and computational desolvation calculations.

Table S19. Representation of the Experimental alcohol solvate structures.

	a/Å	b/Å	c/Å	β/°	E_{latt} /kJ mol^{-1}
S-MeOH (RT)	19.2743(7)	7.1506(1)	13.7116(3)	94.913(2)	
S-MeOH (100 K)	19.1146(9)	7.0796(3)	13.5933(6)	95.426(4)	
PBE-TS (0 K)	19.1692	6.9936	13.6272	95.732	
CrystOpt (0 K)	18.9741	7.1209	13.9429	96.6819	-693.44
Desolv(CO) (0 K)	19.5894	6.6458	13.4570	106.7261	-646.70
S-EtOH (RT)	20.8325(14)	7.1543(1)	13.6644(16)	93.581(10)	
S-EtOH (100 K)	20.522(3)	7.0606(9)	13.6148(17)	96.928(6)	
PBE-TS (0 K)	20.5723	6.9357	13.5506	93.376	
CrystOpt (0 K)	20.2731	7.0522	14.0089	98.2259	-698.72
Desolv(CO) (0 K)	17.0190	7.0604	13.8899	88.9419	-608.76
S-iPrOH (RT)	20.9214(12)	7.2506(2)	13.6223(12)	92.874(7)	
S-iPrOH (100 K)	20.7854(12)	7.1748(4)	13.5299(8)	92.979(3)	
PBE-TS (0 K)	20.7803	7.0655	13.5141	93.288	
CrystOpt (0 K)	20.8012	7.1568	13.9454	94.5037	-701.66
Desolv(CO) (0 K)	17.0184	7.0607	13.8997	89.0061	-608.91
S-nBuOH (RT)	22.6813(19)	7.1622(2)	13.6973(6)	99.110(3)	
S-nBuOH (100 K)	22.500(4)	7.071(2)	13.643(3)	100.45(3)	
PBE-TS (0 K)	22.3951	6.9413	13.6150	100.043	
S-iBuOH (RT)	23.6864(24)	7.1530(2)	13.6322(7)	105.244(4)	
S-iBuOH (100 K)	22.749(5)	7.0359(13)	13.517(3)	92.305(14)	
S-iBuOH (100 K)	23.651(4)	7.1555(10)	13.627(2)	105.298(9)	
PBE-TS (0 K)_4	22.7737	6.8941	13.5397	92.265	
PBE-TS (0 K)_6	23.7547	6.9361	13.3854	105.077	
S-nPeOH (RT)	23.9611(16)	7.1818(2)	13.6823(12)	99.797(7)	
S-nPeOH (100 K)	23.564(6)	7.0823(11)	13.625(4)	102.26(2)	
PBE-TS (0 K)	23.3837	6.9532	13.6417	102.982	
S-EtGly (RT)	39.2019(16)	7.0831(2)	13.6181(4)	103.764(2)	
S-EtGly (100 K)	39.137(2)	7.0158(4)	13.5444(7)	103.948(2)	
PBE-TS (0 K)	39.2060	6.9071	13.5686	103.862	
CrystOpt (0 K)	38.7114	7.0252	13.8632	104.0700	-1366.89
Desolv(CO) (0 K)	39.9031	6.6683	13.3399	95.1578	-639.46
S-PrGly (RT)	13.6663(8)	7.1511(2)	38.3118(31)	90	
S-PrGly (RT)	13.6770(3)	7.15140(10)	38.3289(7)	90	
DFT-D	13.6115	6.9828	38.4527	90.00	
CrystOpt	13.9503	7.1186	37.6214	90.00	-1361.91
Desolv(D)	13.3373	6.6653	39.5372	90.00	-639.82

C) ssNMR Crystallography:

NMR shielding calculations were performed on PBE-TS optimized RT structural models of Form I, the dihydrate and all alcohol solvates, using the CASTEP NMR code.[12] Brillouin zone integrations were performed on a symmetrized Monkhorst–Pack k-point grid with the number of k-points chosen to provide a maximum spacing of 0.07 $Å^{-1}$ and a basis set cut-off of 780 eV. The self-consistent field convergence on total energy was set to $1x10^{-5}$ eV. Energy minimizations were performed using the Broyden–Fletcher–Goldfarb–Shanno optimization scheme within the space group constraints. Shielding constants were calculated with on the fly pseudopotentials.
The CASTEP computed shielding constants, σ_{calc}, were converted to chemical shifts, δ_{calc}, according to $\delta_{calc} = \sigma_{ref} - \sigma_{calc}$ using a reference value, σ_{ref}, taken from the zero intercepts of the fits of the calculated shielding *v*. experimental chemical shift plots ($\sigma_{Castep} = -x \cdot \delta_{exp} + \sigma_{ref}$) for each solid form. Overlays of the ^{13}C NMR spectra and the calculated chemical shifts (δ_{calc}) from the corresponding CASTEP NMR calculations are shown in this sections.

6. Form I, Form II and Dihydrate

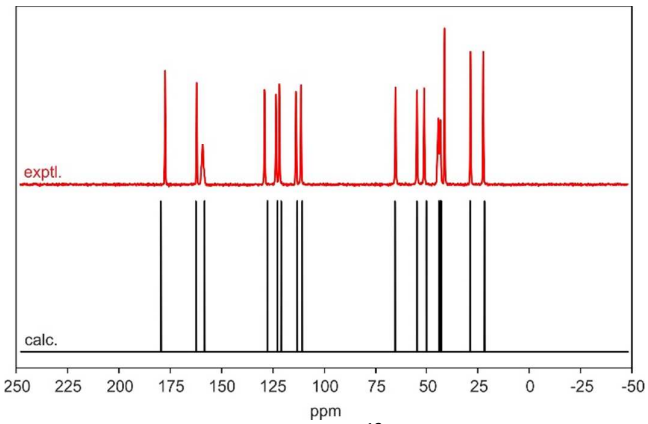

Figure S42. Overlay of experimental (top) and computed ^{13}C ssNMR spectra of Form I.

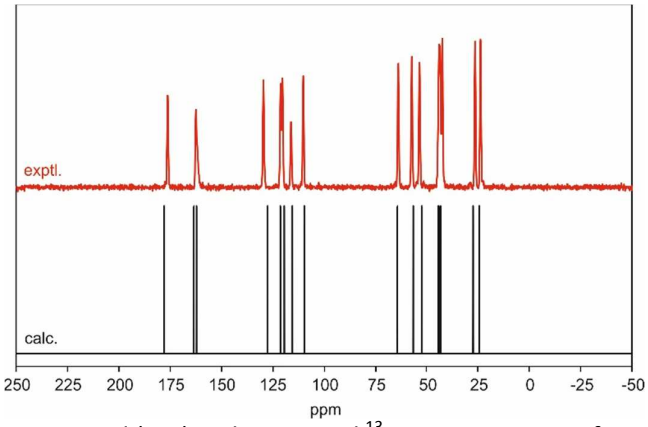

Figure S43. Overlay of experimental (top) and computed ^{13}C ssNMR spectra of Form II.

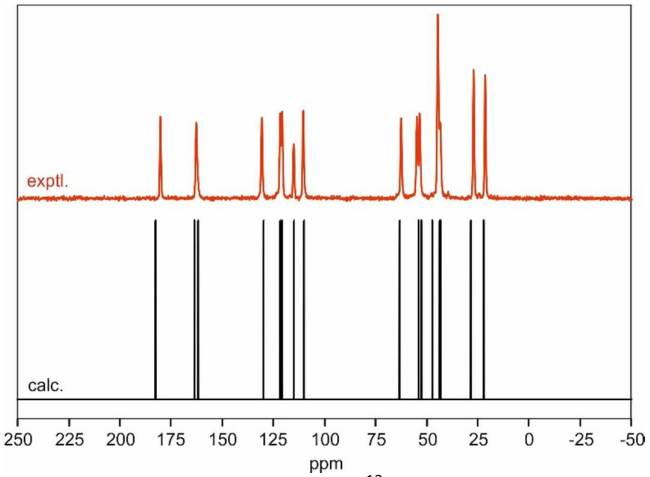

Figure S44. Overlay of experimental (top) and computed ^{13}C ssNMR spectra of the dihydrate.

7. Mono-alcohol Solvates

^{13}C ssNMR spectra of S-nPrOH, S-2BuOH and S-nPeOH are not phase pure, showing in addition to the solvate peaks also the form I peaks.

In Figure S45 the experimental ^{13}C ssNMR spectrum of **S-MeOH** is contrasted to computed chemical shifts calculated for the two methanol polymorphs (homo- and heterochiral B5H$^+$ stacks). The two calculated spectra are very similar and the max. difference in C-atom peak positions relative to the experimental spectrum is less than 1.2 ppm.

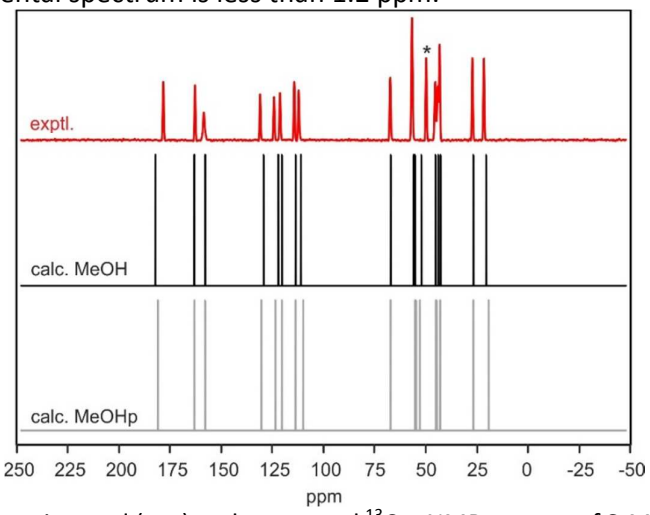

Figure S45. Overlay of experimental (top) and computed ^{13}C ssNMR spectra of S-MeOH. Solvent C-atom highlighted with "*". Calc. MeOH – heterochiral B5H$^+$ stacks and calc. MeOHp – homochirial B5H$^+$ stacks.

The calculated chemical ^{13}C chemical shift positions are nearly indistinguishable for the two solvate models EtOH_1 and EtOH_2 apart from the –CH_3 groups (B5+ molecule and EtOH). A comparison of the experimental **S-EtOH** spectrum with the calculated peak positions reveals that either only one orientation is present or movement between the two orientations is faster than the NMR time scale (?dynamic disorder).

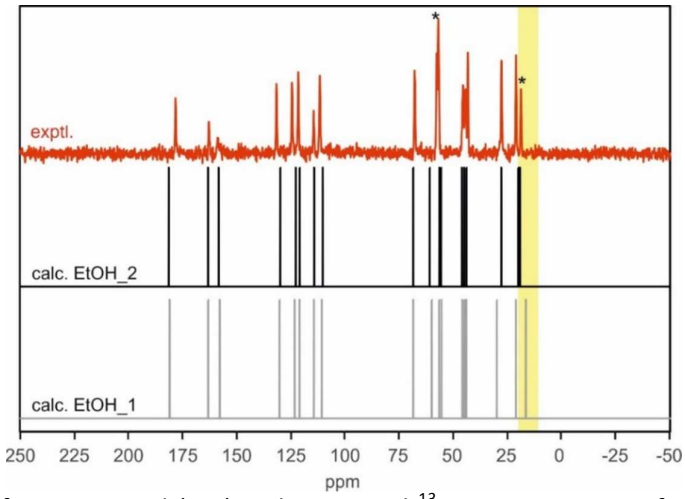

Figure S46. Overlay of experimental (top) and computed ^{13}C ssNMR spectra of S-EtOH. Solvent C-atom peak positions are highlighted with "*".

The experimental **S-nPrOH** spectrum is not phase pure. The characteristic peak positons of Form I are present. In addition to Form I peaks there are still more C-atoms peaks positions present than excepted for $B5^+$ and nPrOH, in particular in the region of aliphatic carbon atoms (< 35 ppm, Figure S47). Thus, (at least) two distinct orientations of the aliphatic part of the nPrOH solvate molecule are present. Lattice energy differences were calculated to be less than 2 and 1 kJ mol^{-1} at the PBE-TS and PBE-D2, respectively. Thus, the calculations support the possibility for disorder of the solvent molecule.

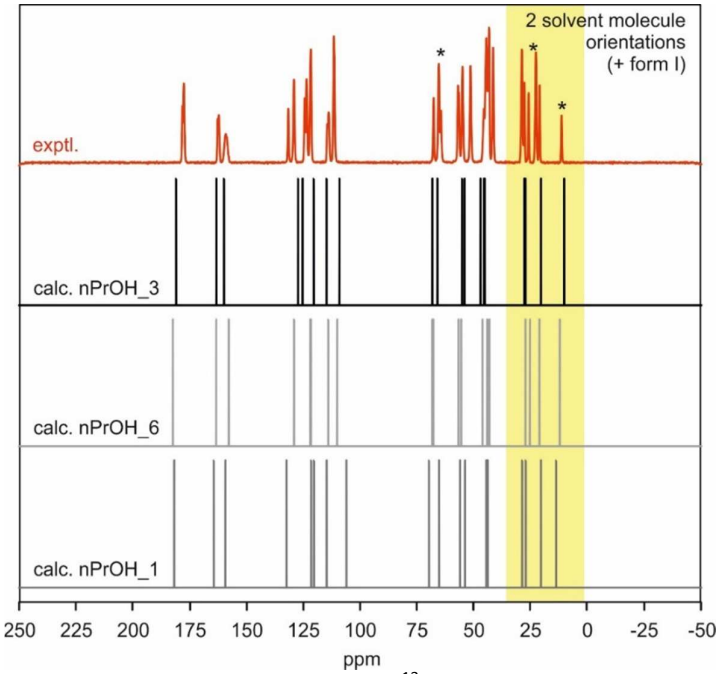

Figure S47. Overlay of experimental (top) and computed ^{13}C ssNMR spectra of S-nPrOH. Solvent C-atom peak positions are highlighted with "*".

An overlay of the experimental NMR spectrum and the calculated chemical shifts of **S-iPrOH** is shown in Figure S48.

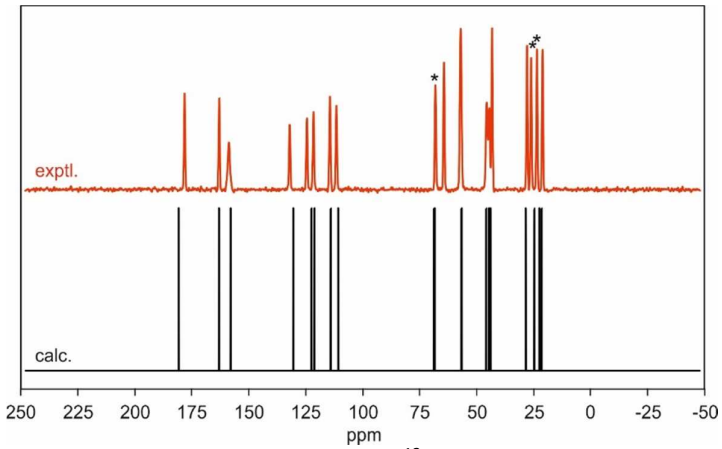

Figure S48. Overlay of experimental (top) and computed ^{13}C ssNMR spectra of S-iPrOH. Solvent C-atom peak positions are highlighted with "*".

An overlay of the experimental NMR spectrum and the calculated chemical shifts of **S-nBuOH** is shown in (Figure S49).

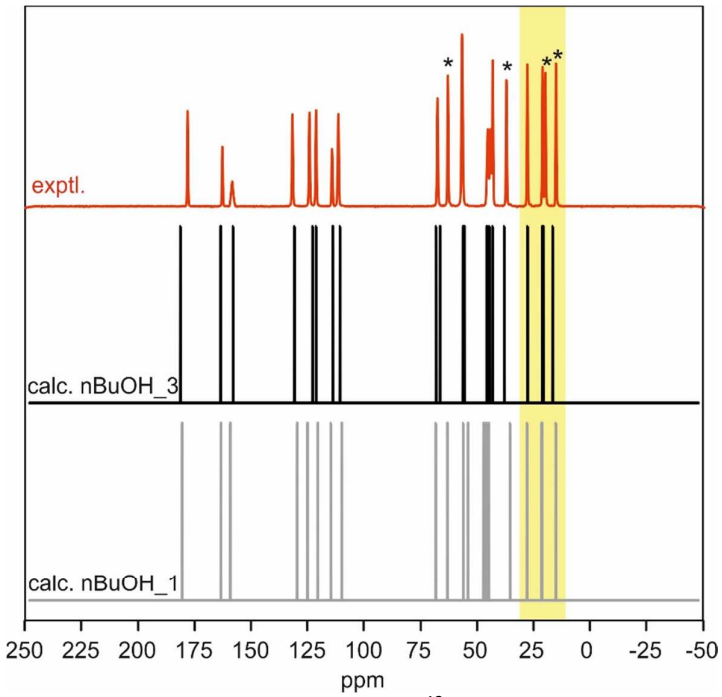

Figure S49. Overlay of experimental (top) and computed ^{13}C ssNMR spectra of S-nBuOH. Solvent C-atom peak positions are highlighted with "*".

The **S-2BuOH** spectrum shows characteristic peaks positons of Form I in addition to the solvate peaks (Figure S50). More peaks than carbons atoms are present in the region of aliphatic carbon

atoms (< 40 ppm), indicating that two distinct orientations of the aliphatic part of the 2BuOH solvent molecule may be present in the solvate. Lattice energy differences were calculated to be less than 2 and 1 kJ mol^{-1} at the PBE-TS and PBE-D2, respectively. Thus, the calculations support the possibility for disorder of the solvent molecule.

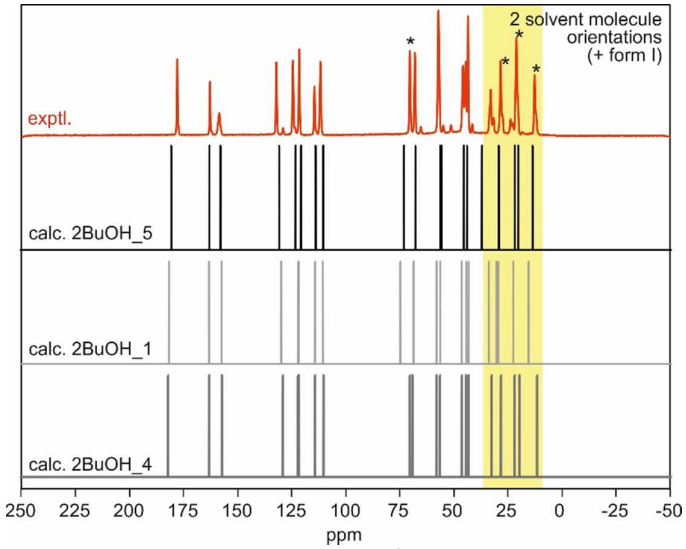

Figure S50. Overlay of experimental (top) and computed ^{13}C ssNMR spectra of S-2BuOH. Solvent C-atom peak positions are highlighted with "*".

The **S-iBuOH** ^{13}C ssNMR spectrum shows only one peak for each $B5H^+$ and iBuOH molecule (Figure S51). A comparison of the experimental **S-iBuOH** spectrum with the calculated peak positions reveals that either only one orientation is present or movement between the two orientations is faster than the NMR time scale (?dynamic disorder). Based on initial SCXRD data more than one orientation of the solvent molecule is possible.

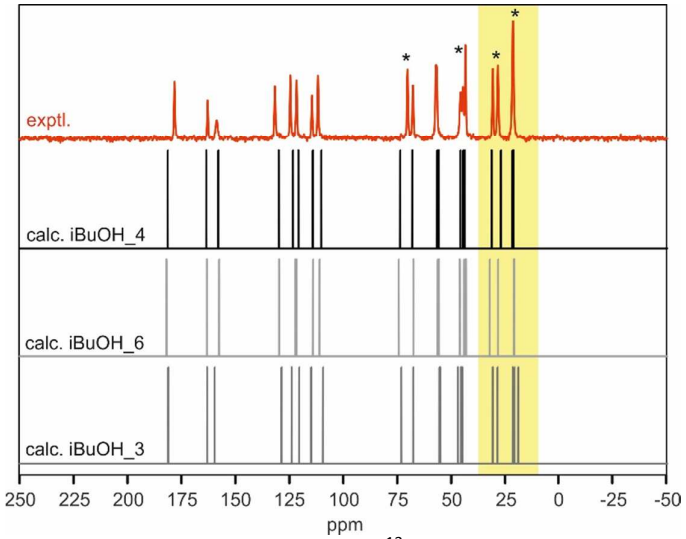

Figure S51. Overlay of experimental (top) and computed ^{13}C ssNMR spectra of S-iBuOH. Solvent C-atom peak positions are highlighted with "*".

Characteristic Form I peaks positions are present in the ssNMR spectrum of **S-nPeOH**. Furthermore, based on the number ^{13}C peaks more than one solvent molecules orientation is present in the solvate (Figure S52). Lattice energy differences were calculated to be less than 4.5 and approx. 1 kJ mol^{-1} at the PBE-TS and PBE-D2, respectively. Thus, the calculations support the possibility for disorder of the solvent molecule.

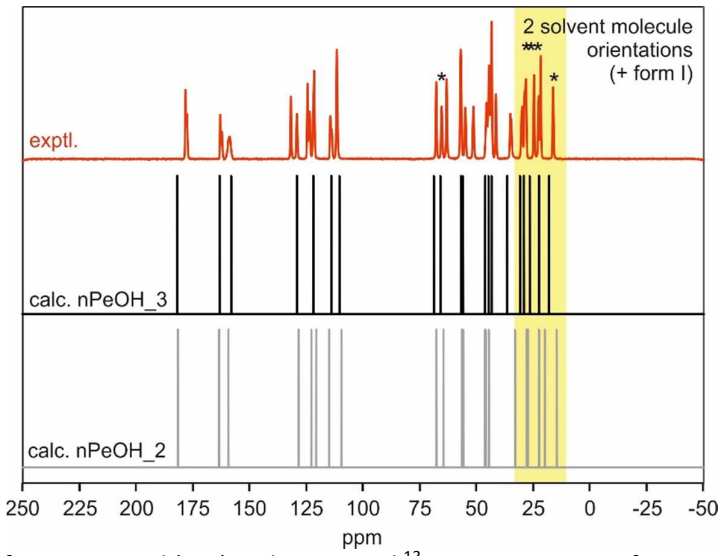

Figure S52. Overlay of experimental (top) and computed ^{13}C ssNMR spectra of S-nPeOH. Solvent C-atom peak positions are highlighted with "*".

An Overlay of the experimental NMR spectrum and the calculated chemical shifts of **S-nOcOH** is shown in Figure S53.

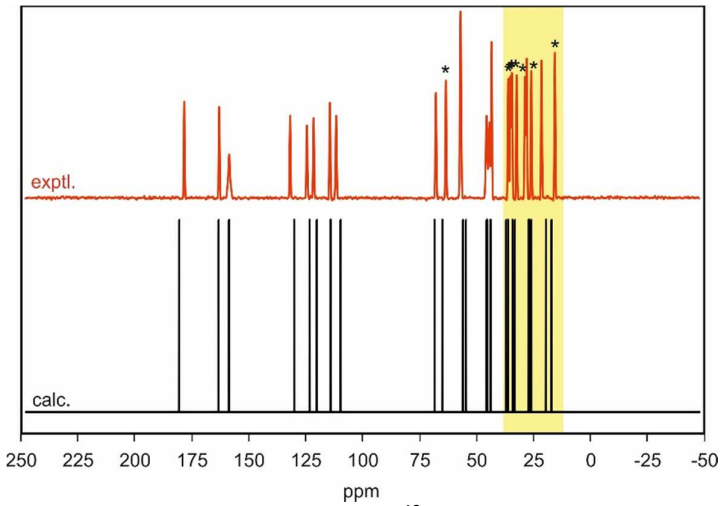

Figure S53. Overlay of experimental (top) and computed ^{13}C ssNMR spectra of S-nOcOH. Solvent C-atom peak positions are highlighted with "*"

8. Hemi-alcohol Solvates

An Overlay of the experimental **S-EtGly** NMR spectrum and the calculated chemical shifts is shown in Figure S54.

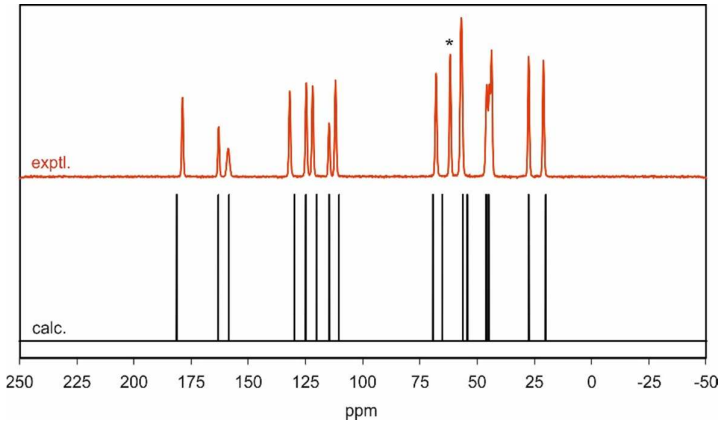

Figure S54. Overlay of experimental (top) and computed ^{13}C ssNMR spectra of S-EtGly. Solvent C-atom peak position is highlighted with "*"

The ^{13}C ssNMR spectrum of **S-PrGly** shows peak splitting which can be related to the two crystallographically independent B5^{+} molecules of the asymmetric S-PrGly unit (Figure S55, highlighted in green).

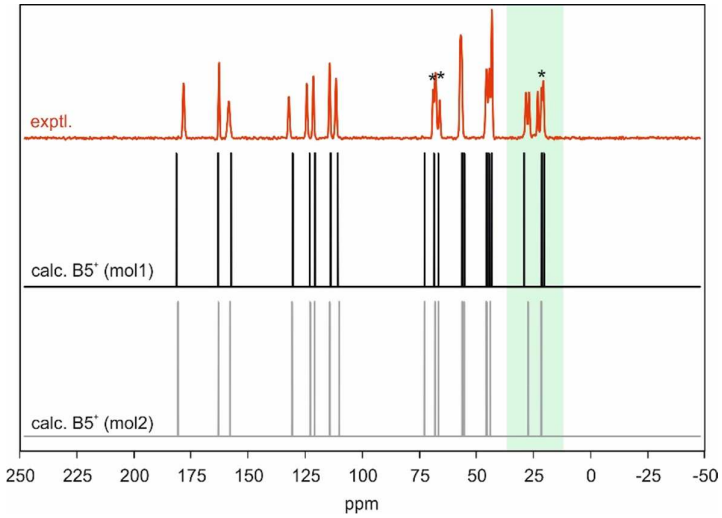

Figure S55. Overlay of experimental (top) and computed ^{13}C ssNMR spectra of S-PrGly. Solvent C-atom peak positions are highlighted with "*". Peak region of –CH_3 groups highlighted in green.

D) Experimental Section:

9. Preparation of B5HCl Crystal Forms

B5HCl Form I (>99% purity) was supplied by Lilly Research Laboratories.

Form II:

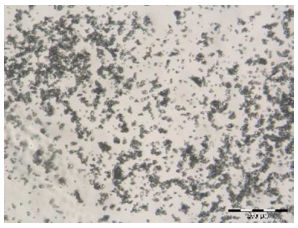

B5HCl (~300 mg) was suspended in 0.1 N HCl (2 mL) at RT with stirring (500 RPM). The temperature was oscillated between 20 and 10 °C at 0.1 °C min^{-1} overnight. The product dihydrate, confirmed to be phase pure by PXRD, was vacuum filtered and placed in the 0% RH chamber for two days.

Dihydrate:

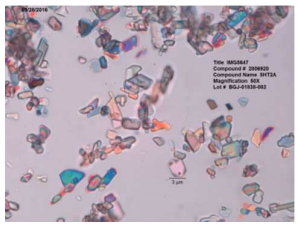

B5HCl (300 mg) was suspended in water (2 mL) at RT with stirring (600 RPM). The suspension was stirred for one day, then isolated by vacuum filtration.

MeOH Solvate:

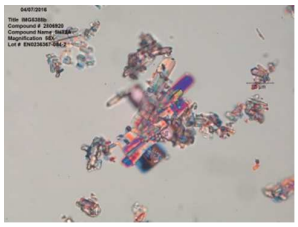

B5HCl (200 mg) was slurried in MeOH (20 mL) at RT. The solid product was characterized by capillary XRPD as a wet suspension. Crystals were harvested by vacuum filtration and air-dried. Single crystals of the MeOH solvate were grown by slow evaporation of a 2.8:5 MeOH-iPrOH solution at RT.

EtOH Solvate:

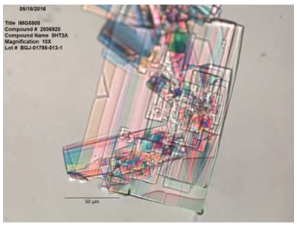

B5HCl (27 mg) was mostly dissolved in 5:1 EtOH-H_2O (1.1 mL) at RT. The stirred (250 RPM) solution was gently heated to fully dissolve the starting material, then slowly syringe filtered into EtOH (40 mL) at RT. The vessel was covered and the solution allowed to stand at RT for 9 days. The solid product was characterized by capillary XRPD as a wet suspension. Crystals were harvested by vacuum filtration and air-dried.

n-PrOH solvate:

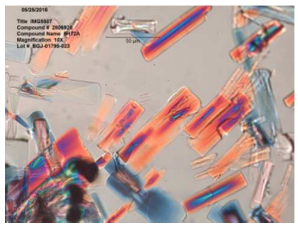

B5HCl (350 mg) was mostly dissolved in 5:1 EtOH-H_2O (~10 mL). The stirred (250 RPM) solution was gently heated to fully dissolve the starting material, then slowly syringe filtered into nPrOH (190 mL) at RT. The vessel was covered and the solution allowed to stand at RT overnight. The solid product was characterized by capillary XRPD as a wet suspension. Crystals were harvested by vacuum filtration and air-dried.

i-PrOH Solvate:

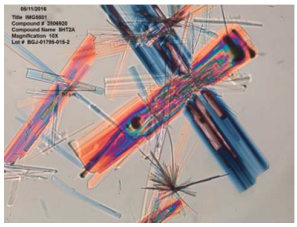

B5HCl (25.7 mg) was mostly dissolved in 5:1 IPA-H_2O (2.4 mL). The stirred (250 RPM) solution was heated to 50 °C, then slowly syringe filtered into a clean vessel. The vessel was covered with parafilm punctured with pinholes to allow the solution to slowly evaporate at RT. The solid product was characterized by capillary XRPD as a wet suspension. Crystals were harvested by vacuum filtration and air-dried.

n-BuOH Solvate:

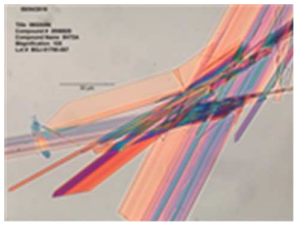

B5HCl (400 mg) was mostly dissolved in 5:1 EtOH-H_2O (12 mL). The stirred (250 RPM) solution was heated to 50 °C, then slowly syringe filtered into nBuOH (200 mL) at RT. The vessel was covered, then placed allowed to stand at RT to crystallize. The solid product was characterized by capillary XRPD as a wet suspension. Crystals were harvested by vacuum filtration and air-dried.

2-BuOH Solvate:

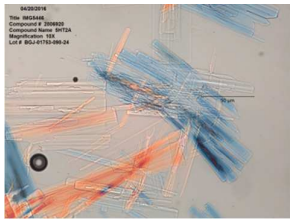

B5HCl (26 mg) was mostly dissolved in 5:1 EtOH-H_2O (1 mL). The stirred solution (250 RPM) was heated gently, then slowly syringe filtered into 2-BuOH (19 mL) at RT. The vessel was covered and the solution allowed to stand at RT for 11 days to crystallize. The solid product was characterized by capillary XRPD as a wet suspension. Crystals were harvested by vacuum filtration and air-dried.

i-BuOH Solvate:

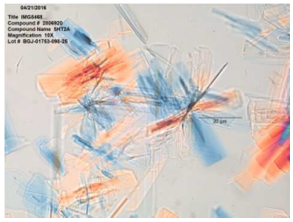

B5HCl (25 mg) was mostly dissolved in 5:1 EtOH-H_2O (1 mL). The stirred (250 RPM) solution was heated gently, then slowly syringe filtered into iBuOH (19 mL) at RT. The vessel was covered and the solution allowed to stand at RT overnight. The solid product was characterized by capillary XRPD as a wet suspension. Crystals were harvested by vacuum filtration and air-dried.

n-Pentanol Solvate:

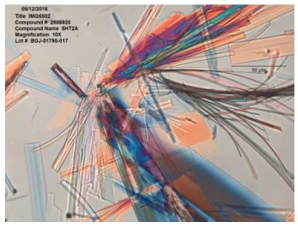

B5HCl (322 mg) was mostly dissolved in 5:1 EtOH-H_2O (9 mL). The stirred (250 RPM) solution was heated to 50 °C, then slowly syringe filtered into n-pentanol (200 mL) at RT. The vessel was covered and the solution allowed to stand at RT overnight. The solid product was characterized by capillary XRPD as a wet suspension. Crystals were harvested by vacuum filtration and air-dried.

n-Octanol Solvate:

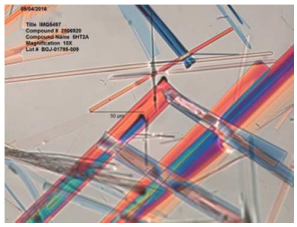

B5HCl (386 mg) was mostly dissolved in 5:1 EtOH-H_2O (12 mL). The stirred (250 RPM) solution was heated to 50 °C to mostly dissolve the solids, then slowly syringe filtered into n-octanol (200 mL) at RT. The vessel was covered, then allowed to stand at RT overnight. The solid product was characterized by capillary XRPD as a wet suspension. Crystals were harvested by vacuum filtration and air-dried.

Ethyleneglycol Hemisolvate:

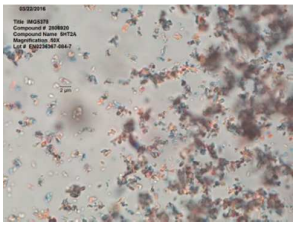

B5HCl (200 mg) was slurried in ethylene glycol (10 mL) at RT. The solid product was characterized by capillary XRPD as a wet suspension. Crystals were harvested by vacuum filtration and air-dried.

1,2-Propanediol Hemisolvate:

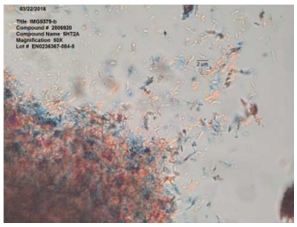

B5HCl (250 mg) was slurried in propylene glycol (10 mL) at RT. The solid product was characterized by capillary XRPD as a wet suspension. Crystals were harvested by vacuum filtration and air-dried.

10. Solubility

B5HCl (30 or 100 mg) was dispensed into 29 (4 mL) vials using a Symyx Powdernium® powder weighing station. To the vials, a total of 21 pure and 8 mixed solvents (0.25 or 0.8 mL) was added. All suspensions were agitated at 250 RPM on a J-KEM Shaker Block for 24 hours at 25 °C. After 2 hours of agitation, ~200 µL aliquots were withdrawn from suspensions through 0.45 micron Millex PTFE filters. After the 24 hour equilibration period, ~300 µL aliquots were withdrawn through 0.45 micron Millex PTFE filters from each of the vials containing visible solids. Samples were then diluted with mobile phase and analyzed by HPLC. When possible, residues were air dried and submitted for XRPD analysis. The solubility measurements were repeated at 50 °C (sampling only after 24 hours) for select pure solvents in which the 25 °C solubility of B5HCl was between 1 and 100 mg/mL. The samples were analyzed using an Agilent 1100 HPLC with a Zorbax RX C-18 column (15 cm x 4.6 mm, 3.5 micron particle size). The mobile phase consisted of 0.1% TFA/water, 30%, acetonitrile, 70%. Instrument conditions were as follows: flow rate 1.0 mL/minute, wavelength of detection 230 nm and column temperature 30 °C. A stock solution (1.0 mg/mL) of B5HCl was prepared in methanol and diluted with mobile phase to give concentrations suitable for quantification of the solubility samples.

Table S20. Solubility (N=1) of B5HCl at 25 and 50 °C.

Solvent(s) (v/v)	a_w	Temp (°C)	Solubility (mg/mL)		Solid Form (XRPD)	Temp (°C)	Solubility (mg/mL)	Solid Form (XRPD)
			2 h	24 h			24 h	
Methanol		25	12.88	11.56	☐,**M**	50	17.04	☐,**M**
Ethanol		25	3.33	2.25	☐	50	8.37	☐
2-Propanol		25	0.07	0.04	☐	50	---	---
1-Butanol		25	0.51	0.38	☐	50	---	---
Acetonitile		25	0.03	<0.01	☐	50	---	---
Acetone		25	<0.01	<0.01	☐	50	---	---
Methyl ethyl ketone		25	0.05	0.02	☐	50	---	---
Methyl isobutyl ketone		25	0.02	<0.01	☐	50	---	---
Ethyl acetate		25	0.1	0.04	☐	50	---	---
Isopropyl acetate		25	<0.01	<0.01	☐	50	---	---
n-Butyl acetate		25	<0.01	1.57	☐	50	---	---
Methyl t-butyl ether		25	0.01	<0.01	☐	50	---	---
Tetrahydrofuran		25	<0.01	0.05	☐	50	---	---
2-Methyltetrahydrofuran		25	<0.01	<0.01	☐	50	---	---
N-Methyl-2-pyrrolidone		25	40.87	36.62	☐	50	44.64	☐
Dimethyl sulfoxide		25	65.98	38.92	☐,**B5**	50	104.63	☐
Chloroform		25	0.6	<0.01	☐	50	---	---
Toluene		25	<0.01	0.05	☐	50	---	---
Heptane		25	<0.01	<0.01	☐	50	---	---
Water	1.0	25	29.13	20.82	☐,**B5**	50	10.48	☐,**B5**
Methanol - Water (1:1)	0.73	25	>37.5	>37.5	---	50	---	---
Methanol - Water (3:1)	0.50	25	>37.5	>37.5	---	50	118.31	☐
Ethanol - Water (1:1)	0.80	25	>37.5	>37.5	---	50	---	---
Ethanol - Water (3:1)	0.70	25	20.44	>37.5	---	50	109.62	☐
Acetonitrile - Water (1:1)	0.90	25	>37.5	>37.5	---	50	---	---
Acetone - Water (1:2)	0.91	25	>37.5	>37.5	---	50	---	---
2-Propanol - Water (3:1)	0.94	25	31.6	26.52	☐	50	---	---
Ethyl acetate (wet)	0.98	25	0.18	<0.01	☐	50	---	---
Acetic acid - Water (1:1)	0.79	25	>37.5	>37.5	----	50	---	---

[a] ☐ = Form I; **M** = S-MeOH; **B5** = parent compound.

pH Solubility

B5HCl (50 mg) and/or B5 free base (40 mg) were manually weighed into vials to which was added 0.5 mL or 0.8 mL of pH 2-8 (50 or 100 mM) phosphate buffer solution, water or HCl (0.001, 0.01, 0.1 or 1N). All suspensions were agitated at 250 RPM on a J-KEM Shaker Block for 24 hours at 25 °C. After 2 hours of agitation, ~200 mL aliquots were withdrawn from suspensions through 0.45 micron Millex PTFE filters. After the 24-hour equilibration period, ~300 µL aliquots were withdrawn through 0.45 micron Millex PTFE filters from each of the vials containing visible solids. The filtrate pH was measured using an IQ pH meter. Samples were then diluted with mobile phase and analyzed by HPLC. When possible, residues were air dried and submitted for XRPD analysis. The samples were analyzed using an Agilent 1100 HPLC with a Zorbax RX C-18 column (15 cm x 4.6 mm, 5.0 micron particle size). The mobile phase consisted of 0.1% TFA/water, 20%, acetonitrile, 80%. HPLC conditions were as follows: flow rate 1.0 mL/minute, wavelength of detection 230 nm, injection volume of 20 µl and column temperature 30 °C. A stock solution (1.0 mg/mL) of B5HCl was prepared in methanol and diluted with mobile phase to give concentrations suitable for quantification of the solubility samples. Additional buffers of increasing molarity were tested to determine if the pH could be maintained throughout a given solubility experiment. Acetate buffers (100 and 200 mM) were evaluated at pH 5 and 6, while McIlvaine phosphate-citrate buffer was examined at pH 3, 4 and 6.

The pKa values of B5, estimated from a non-linear regression analysis of experimental pH solubility data (below) and directly measured by potentiometric titration, were in excellent agreement (pKa1 (acid) 3.37/3.17 and pKa2 (N3 base) 7.85/7.54).

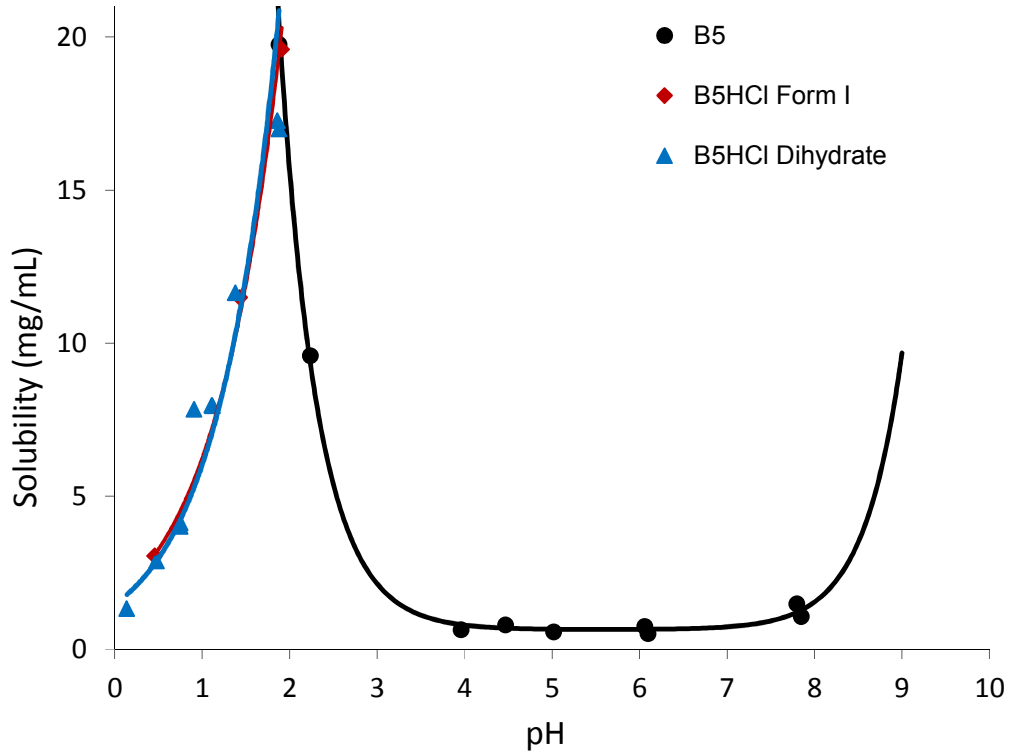

Figure S56. pH solubility profile of B5/B5HCl at 25 °C. The solid lines are taken from the non-linear regression fits to the experimental data.

11. Solid Form Screen

The solution crystallization screen of B5HCl, generally designed around the solubility properties of Form I, encompassed solvent evaporation, cooling, antisolvent addition, pH swing and vapor diffusion experiments. Solvent diversity was ensured based on the premise that the success rate of discovering new solid forms by crystallization from solution may be increased if solvents with diverse properties are surveyed. The specific conditions under which B5HCl could be recrystallized were determined not only by the solubility of the API, but also by the suitability (boiling point, evaporation rate, miscibility) of specific solvents for the different types of recrystallization experiments. In addition to crystallization from solution, B5HCl was screened for hydrates specifically using moisture sorption analysis and slurry techniques, while thermal analysis (ramped temperature) and isothermal annealing were used to screen for high temperature forms and desolvated forms. The experiments conducted are detailed in the following sections.

An attempt to render B5HCl amorphous by lyophilization was unsuccessful, highlighting the relative ease with which the Form I crystal nucleates.

11.1 Evaporative crystallization

B5HCl (25 ± 1 mg) was manually weighed into 15 (8 mL) vials. Solvents (0.3-8 mL) were dispensed to the vials manually. The suspensions were heated (50 °C; except CH_2Cl_2 and MTBE) with stirring, then filtered through 0.45 µm syringe filters into clean vials. The vials were covered with parafilm rendered with a pinhole, then placed in a fume hood to allow the solvents to slowly evaporate at RT. Residues were analyzed after either evaporation of the solvent to dryness or isolation by vacuum filtration. HT evaporative crystallization screening was also performed using the Symyx Discovery Tools® system. B5HCl (25 ± 0.5 mg) was dispensed as a powder using a Symyx Powdernium® powder weighing station into a substrate containing 24 (4 mL) vials. A total of 15 different pure and mixed solvents (2-4 mL total volume) was manually dispensed to the vials. The suspensions/solutions were magnetically stirred for 1.5 hours at 40 °C, after which time the stir bars were removed and the solutions were syringe filtered into clean (4 mL) vials. The vials were then transferred to two temperature controlled blocks and the solutions allowed to evaporate at either RT or 50 °C for approximately 2 days under N_2. The results of the evaporative crystallization screen are summarized in Table S21.

Table S21. Summary of B5HCl evaporative crystallization experiments.

Solvent(s) (v/v/v)	Form(s)		Solvent(s) (v/v/v)	Form(s)	
	5 °C	RT		RT	50 °C
1:0.4 MeOH-IPA		M	MeOH	M,□	M,□
1:0.8 MeOH-IPA		M	1:1.8 MeOH-IPA	M	
1:8 MeOH-IPA	I	I	1:3.3 MeOH-IPA	M	
1:8 MeOH-nPrOH	-	Pr	1:6.7 MeOH-IPA	I	
1:8 MeOH-nBuOH	B	B	EtOH	E,□	
1:6 MeOH-2BuOH	2B,M?	□,?	H_2O	□	□
1:8 MeOH-iBuOH	iB	iB	1:1 MeOH-H_2O	□	
1:7 MeOH-tBuOH	□,?	□,?	3:1 MeOH-H_2O	□, **B5**	
1:8 MeOH-pentanol	P,M?	P	1:1 EtOH-H_2O	□	□
1:7 MeOH-octanol	O,M	O	3:1 EtOH-H_2O	□	
1:7 MeOH-acetone	M,?	□,?	9:1 EtOH-H_2O	E,□	
1:8 MeOH-ACN	M	□	~1:1 IPA-H_2O	□	
5:1:27 EtOH-H_2O-IPA	E,I?	E,I?	3:1 IPA-H_2O	□	□
5:1:27 EtOH-H_2O-nPrOH	-	Pr	9:1 IPA-H_2O	□	
5:1:27 EtOH-H_2O-nBuOH	B	B	2:1 1-BuOH-H_2O	B,□,◇	
5:1:30 EtOH-H_2O-2BuOH	□	□,?	17:3 1-BuOH-H_2O	B,□	
5:1:27 EtOH-H_2O-iBuOH	iB	iB	1:1 ACN-H_2O	□,**B5**	□
5:1:30 EtOH-H_2O-tBuOH	□,?	□	1:1 acetone-H_2O	□	□
5:1:27 EtOH-H_2O-pentanol	P,□?	P	1:2 acetone-H_2O	□,**B5**	
5:1:27 EtOH-H_2O-octanol	□,?	S_{OctOH}	9:1 acetone-H_2O	□	
5:1:37 EtOH-H_2O-acetone	□,?	□,?	1:2 EtOH-heptane		□
5:1:27 EtOH-H_2O-ACN	□,?	□	2-methoxyethanol	□	
1:7 MeOH-MEK	M,?	M,?	1:1 chloroform-MeOH	M,□	M,□
5:1:28 EtOH-H_2O-MEK	□	□	1:1 chloroform-EtOH	□	
3:20 MeOH-nBuOAc	M	M	N-methyl-2-pyrrolidone	□	□,**B5**
5:1:32 EtOH-H_2O-nBuOAc	□	□	DMSO	□	□
45:1:40 IPA-H_2O	I	I	MeOH-ACN	M,□	
iPrOAc-H_2O		□,◇	MeOH-acetone	□	
H_2O-MeOH-acetone		□,◇	1:1 1,4-dioxane-H_2O	□	□
Ethylene glycol		EG	13:1 1,4-dioxane-H_2O	□	
1,2-propanediol		PG	1:1 THF-H_2O	□	□
1,2-propanediol//heptane		PG	13:1 THF-H_2O	□	
H_2O-EtOH-THF		□,E	1:1 acetic acid-H_2O	□	□
100:1 1-BuOH-DMSO		□, **B5**	~6:1 H_2O-iPrOAc	◇	□ (40°C)

[a] □ = Form I; ◇ = dihydrate; **M** = S-MeOH; **E** = S-EtOH; **Pr** = S-nPrOH; **I** = S-iPrOH; **B** = S-nBuOH; **iB** = S-iBuOH; **2B** = S-2BuOH; **P** = S-nPeOH; **O** = S-nOcOH; **EG** = S-EtGly; **PG** = S-PrGly; **B5** = parent compound.

11.2 Cooling crystallization

B5HCl (25 and 50 ± 1 mg) was dispensed using a Symyx Powdernium® powder weighing station into 1.8 mL vials. Solvents (0.5-1.5 mL total volume) were dispensed to the vials manually. The vials were then transferred to the Crystal16™ parallel crystallizer, equipped with programmable heating/cooling, magnetic stirring and turbidity sensors. The suspensions were stirred at 700 or 1000 rpm then heated to 55, 60, 70 or 75 °C at 3 °C/min, equilibrated for 2 hours, then cooled to 10 °C at 1 °C/min. Solvent/antisolvent was added to samples that did not dissolve or precipitate and another heat/cool cycle performed. Solutions were forward processed in either antisolvent addition or evaporative crystallizations. The results of the slow and fast cooling crystallization screen are summarized in Table S22.

Table S22. Summary of cooling crystallization experiments.

Solvent	Form(s)[a]	Solvent(s)	Form(s)[a]	Solvent(s)	Form(s)[a]
Methanol	M,□	wet EtOAc	□	1:1 1,4-dioxane-H_2O	□
N-methyl-2-pyrrolidone	-	9:1 acetone-H_2O	□	4:1 1,4-dioxane-H_2O	□
DMSO	-	2:1 acetone-H_2O	-	19:1 1,4-dioxane-H_2O	□
DMAC	-	3:1 THF-H_2O	□	19:1 IPA-H_2O	□
DMF	□	1:1 EtOH-H_2O	□	9:1 IPA-H_2O	□,I
H_2O	□,**B5**	3:1 EtOH-H_2O	□	4:1 IPA-H_2O	□
1,2-propanediol	PG	9:1 EtOH-H_2O	□	3:7 IPA-H_2O	□
2-methoxyethanol	-	19:1 EtOH-H_2O	□	3:1 ACN-H_2O	-
benzyl alcohol	-	3:8 DMSO-ACN	□	1:1 EtOH-octanol	O
5:7 chloroform-DMSO	-	9:7 chloroform-DMSO	-	5:2 chloroform-DMSO	-
5:7 EtOH-DMSO	-	9:7 EtOH-DMSO	-	5:2 EtOH-DMSO	-
5:7 acetone-DMSO	-	9:7 acetone-DMSO	-	5:2 acetone-DMSO	-
5:7 ACN-DMSO	-	9:7 ACN-DMSO	□	5:2 ACN-DMSO	-
5:7 MEK-DMSO	-	9:7 MEK-DMSO	□	5:2 MEK-DMSO	-
5:7 MTBE-DMSO	-	9:7 MTBE-DMSO	□	5:2 MTBE-DMSO	-
5:7 THF-DMSO	-	9:7 THF-DMSO	-	5:2 THF-DMSO	-
2:1 2-methoxyethanol-MeOH	□	2:1 benzyl alcohol-iPrOAc	□	1:2 DMSO-THF	□
~5:1:5 IPA-H_2O-acetone	□	~2:1:3 1-BuOH-H_2O-heptane	□	85:15 1-BuOH-H_2O	B
1,2-propanediol	□	15:1 H_2O-EtOH	□,**B5**	1:30:40 DMSO-EtOH-octanol	□,O
1:3 EtOH-cyclohexane	□	EtOH	E,□	5:1 IPA-H_2O	I
85:15 1-BuOH-H_2O	□	MeOH-toluene	M	Ethylene glycol	EG
1:50 DMSO-octanol (19.5)	O,?				

[a] □ = Form I; ◇ = dihydrate; **M** = S-MeOH; **E** = S-EtOH; **Pr** = S-nPrOH; **I** = S-iPrOH; **B** = S-nBuOH; **iB** = S-iBuOH; **2B** = S-2BuOH; **P** = S-nPeOH; **O** = S-nOcOH; **EG** = S-EtGly; **PG** = S-PrGly; **B5** = parent compound.

11.3 Antisolvent addition

Stock solutions in various solvents were prepared by adding minimal solvent to B5HCl (200-400 mg) to dissolve the API at 40 °C (with no precipitation on cooling to RT). To ensure complete dissolution of the drug substance prior to antisolvent addition, the solutions were prepared in advance and filtered through 0.45 µm PTFE syringe filters prior to antisolvent addition. Standard antisolvent addition experiments were conducted at RT. Antisolvent was (manually) added dropwise until either persistent clouding was observed or the maximum antisolvent volume (20 mL) was dispensed. Solutions wherein precipitation was not observed were evaporated. Solid products were isolated by vacuum filtration, then air-dried in the hood. Reverse antisolvent addition experiments were also performed, where HCl solutions were filtered into flasks or vials containing antisolvent. The work-up procedures were the same as those used in the standard antisolvent addition experiments. The results of the antisolvent addition crystallization screen are summarized in Table S23.

Table S23. Summary of standard and reverse antisolvent addition crystallization experiments.

Solvent//Antisolvent	Temp (°C)	Form(s) [a]	Solvent//Antisolvent	Temp (°C)	Form[a]
Standard antisolvent addition					
MeOH//EtOAc	RT	□,**M**	DMSO//MTBE	RT	□
MeOH//nBuOAc	RT	**M**	DMSO//ACN	RT	□
MeOH//aniline	RT	-	DMSO//propionitrile	RT	□
MeOH//2-MeTHF	RT	□,**M**	DMSO//acetone	RT	□
MeOH//THF	RT	**M**	DMAC//MEK	RT	□
MeOH//toluene	RT	**M**	NMP//wet EtOAc	RT	□
MeOH//xylene	RT	**M**	NMP//nBuOAc	RT	□
MeOH//MEK	RT	**M**	NMP//sulfolane	RT	-
MeOH//ACN	RT	-	NMP//anisole	RT	□
MeOH //acetone	RT	-	benzyl alcohol//iPrOAc	RT	□
DMSO //iPrOAc	RT	□	H_2O//iPrOAc	RT	-
DMSO//nBuOAc	RT	□	H_2O//IPA	RT	-
DMSO//2-MeTHF	RT	□	H_2O//ACN	RT	-
DMSO//THF	RT	□	H_2O//acetone	RT	-
DMSO//toluene	RT	□	H_2O//THF	RT	-
DMSO//xylene	RT	□	MeOH//toluene	RT	**M**
Reverse antisolvent addition					
EtOH//n-heptane	50	**E**	3:1 IPA-H_2O//IPA	25	-
EtOH//pentane	25	□,**E**	3:1 1,4-dioxane-H_2O//1,4-dioxane	25	-
EtOH//cyclohexane	50	□,**E**	3:1 THF-H_2O//THF	25	-
3:1 ACN-H_2O//ACN	25	□	1:2 DMSO-THF//THF	25	-
3:1 acetone-H_2O//acetone	25	-	EtOH//heptane	50	□
3:1 EtOH-H_2O//pentane	RT	□	4:1 EtOH-H_2O//EtOH	-	-

NMP (1)//IPA (19)	RT	□,?	1:9 MeOH-IPA	RT	I,?
NMP (1)//nPrOH (19)	RT	-	1:9 MeOH-nPrOH	RT	Pr,M
NMP (1)//nBuOH (19)	RT	B	1:9 MeOH-nBuOH	RT	B
NMP//2BuOH (19)	RT	□,?	1:9 MeOH-2BuOH	RT	M,?
NMP (1)//iBuOH (19)	RT	iB	1:9 MeOH-iBuOH	RT	iB
NMP (1)//4:1 tBuOH-acetone (19)	RT	□,?	MeOH (2) 4:1 tBuOH-acetone (18)	RT	M,□,?
NMP (1)//1-pentanol (19)	RT	P	1:9 MeOH-1-pentanol	RT	P,M
1:19 NMP-octanol	RT	O	1:9 MeOH-octanol	RT	O,M
1:19 NMP-ACN	RT	□	1:9 MeOH-ACN	RT	M,?
1:19 NMP-acetone	RT	□,?	1:9 MeOH-acetone	RT	□
5:1 EtOH-H_2O (1)//IPA (19)	RT	E,I?	5:1 EtOH-H_2O (1) octanol (19)	RT	O
5:1 EtOH-H_2O (1)//nPrOH (19)	RT	Pr	5:1 EtOH-H_2O (1) ACN (19)	RT	□
5:1 EtOH-H_2O (1)//nBuOH (19)	RT	B	5:1 EtOH-H_2O (1) acetone (19)	RT	□,?
5:1 EtOH-H_2O (1)//2BuOH (19)	RT	2B	NMP (1) EtOH (19)	RT	-
5:1 EtOH-H_2O (1)//iBuOH (19)	RT	iB	5:1 EtOH-H_2O (1) EtOH (19)	RT	-
5:1 EtOH-H_2O (1)//4:1 tBuOH-acetone (19)	RT	□	5:1 IPA-H_2O (1) IPA (19)	RT	I
5:1 EtOH-H_2O (1)//1-pentanol (19)	RT	P			

□ = Form I; ◇ = dihydrate; M = S-MeOH; E = S-EtOH; Pr = S-nPrOH; I = S-iPrOH; B = S-nBuOH; iB = S-iBuOH; 2B = S-2BuOH; P = S-nPeOH; O = S-nOcOH; EG = S-EtGly; PG = S-PrGly.

11.4 Vapor diffusion

Solutions of B5HCl for vapor diffusion were prepared as follows: B5HCl (25 ± 1 mg) was dispensed manually into 15 (4 mL) vials. Solvents (0.3-4 mL) were dispensed manually to vials. The stirred solutions were heated (35 °C) then filtered to ensure complete dissolution of the drug substance prior to vapor diffusion. Vapor diffusion experiments were set up at ambient temperature by placing the 15 solutions in closed chambers containing one of nine antisolvents. The solid products were recovered by vacuum filtration or decantation of the mother liquor and air-dried. The results of the vapor diffusion phase of the comprehensive solid form screen are summarized in Table S24.

Table S24. Summary of vapor diffusion experiments.

Solvent//Antisolvent	Temp (°C)	Form(s)[a]	Solvent//Antisolvent	Temp (°C)	Form(s)[a]
DMSO//chloroform	RT	□	19:1 MeOH-DMF//acetone	RT	□,M
DMSO//THF	RT	□	19:1 MeOH-DMAC//ACN	RT	□
DMSO//acetone	RT	□	15:1 H_2O-MeOH//acetone	RT	□,◇
DMSO//CH_2Cl_2	RT	□	15:2 H_2O-EtOH//THF	RT	□,◇
DMSO//ACN	RT	□	H_2O//ACN	RT	□
MeOH//MTBE	RT	□,M	3:1 IPA-H_2O//IPA	RT	I
MeOH//chloroform	RT	M	3:1 EtOH-H_2O//EtOH	RT	□
19:1 MeOH-NMP//1,4-dioxane	RT	□,M	5:2 IPA-MeOH (7)// IPA	5	M,I?
10:1 IPA-H_2O (5.5)//IPA	RT	I,?	5:1.2 nPrOH-MeOH (6.2)// nPrOH	5	M,?
10:1 nPrOH-H_2O (5.5)// nPrOH	RT	-	5:1.4 1-pentanol-MeOH (6.4)// 1-pentanol	5	M,?
5:2 IPA-MeOH (7)// IPA	RT	M,I?	5:1.8 1-heptanol-MeOH (6.8)// 1-heptanol	5	M,?
5:1.2 nPrOH-MeOH (6.2)//nPrOH	RT	M,□?	5:1.4 iAmOH-MeOH (6.4)// iAmOH	5	M,?
5:1.4 1-pentanol-MeOH (6.4)//1-pentanol	RT	M,?	5:2 iBuOH-MeOH (7)// iBuOH	5	M,?
5:1.8 1-heptanol-MeOH (6.8)//1--heptanol	RT	M,?	5:2.4 tBuOH-MeOH (7.4)// tBuOH	5	M,?
5:1.4 iPentanol-MeOH (6.4)// iPentanol	RT	M,iP?	5:1 cyclohexanol-MeOH (6)// cyclohexanol	5	M, cH?
5:2 iBuOH-MeOH (7)//iBuOH	RT	M,?	5:2 octanol-MeOH (7)// octanol	5	M,O?
5:2.4 tBuOH-MeOH (7.4)//tBuOH	RT	M,?	5.9:0.2 EtOH-H_2O (6.1)// EtOH	RT	E
5:1 cyclohexanol-MeOH (6)//cyclohexanol	RT	M, cH?	5:0.1.3:0.3 n-heptanol-EtOH-H_2O (6.6)// n-heptanol	RT	□,?
5:2 octanol-MeOH (7)//octanol	RT	M,O?	5:1.2:0.2 iPentanol-EtOH-H_2O (6.4)// iPentanol	RT	□,iP?
10:1 IPA-H_2O (5.5)//IPA	5	I,?	5:2:0.4 tBuOH-EtOH-H_2O (7.4)// tBuOH	RT	□
10:1 nPrOH-H_2O (5.5)// nPrOH	5	-			

[a] □ = Form I; ◇ = dihydrate; M = S-MeOH; E = S-EtOH; Pr = S-nPrOH; I = S-iPrOH; B = S-nBuOH; iB = S-iBuOH; 2B = S-2BuOH; P = S-nPeOH; O = S-nOcOH; EG = S-EtGly; PG = S-PrGly; cH = S-cHexOH.

11.5 Slurry screen

Solutions/suspensions of B5HCl (various forms) were prepared in several solvents, then stirred at RT or 50 °C. Solid products were recovered by vacuum filtration, air-dried and analyzed by XRPD as dry powders. The experiments conducted during this phase of the solid form screen are summarized in Table S25.

Table S25. Summary of B5HCl slurry screening experiments.

Starting Form(s)[a]	Experimental Conditions					Final Form(s) [a,b]
	Solvent(s)	a_w	pH	Temp (°C)	Time (h)	
☐	EtOH			RT	20	☐
☐	1-BuOH			RT	20	☐
☐	EtOAc			RT	20	☐
☐	iPrOAc			RT	20	☐
☐	ACN			RT	20	☐
☐	MIBK			RT	42	☐
☐	MEK			RT	42	☐
☐	$CHCl_3$			RT	42	--
☐	DMAC	-		50	3	☐
☐	DMF	-		50	3	☐
☐	1,4-dioxane	-		50	3	☐
☐	2-ethoxyethanol	-		50	3	☐
☐,◇	99% acetone-H_2O	0.2		RT	2.75	☐,**B5**
☐,◇	97% acetone-H_2O	0.4		RT	2.75	☐,**B5**
☐,◇	95% acetone-H_2O	0.6		RT	2.75	☐,**B5**
☐,◇	75% acetone-H_2O	0.8		RT	2.75	☐,**B5**
◇	H_2O	1		RT	19	**B5**
☐,◇	H_2O	1		RT	4	☐,**B5**
☐,◇	H_2O	1		RT	5	◇
☐	0.1N HCl		1.45	25	24	☐
☐	0.01 N HCl		1.99	25	24	☐
☐	H_2O	1	1.87	25	24	☐,**B5**
☐	Phosphate buffer, pH 2.0 (50 mM)		1.95	25	24	☐
☐	Phosphate buffer, pH 2.0 (100 mM)		1.92	25	24	☐
☐	Phosphate buffer, pH 4.0 (50 mM)		1.98	25	24	☐
☐	Phosphate buffer, pH 4.0 (100 mM)		2.08	25	24	☐,**B5**,◇
☐	Phosphate buffer, pH 6.0 (50 mM)		1.99	25	24	☐,**B5**
☐	Phosphate buffer, pH 6.0 (100 mM)		2.07	25	24	☐,**B5**
☐	Phosphate buffer, pH 8.0 (50 mM)		2.22	25	24	☐,**B5**
☐	Phosphate buffer, pH 8.0 (100 mM)		2.27	25	24	☐,**B5**
☐	Acetate buffer, pH 4.0 (100 mM)		1.95	25	24	☐,**B5**
☐	Acetate buffer, pH 5.0 (100 mM)		2.08	25	24	☐,**B5**

☐	Acetate buffer, pH 4.0 (200 mM)		2.05	25	24	☐,**B5**
☐	Acetate buffer, pH 5.0 (200 mM)		3.28	25	24	**B5**
☐	McIlvaine buffer, pH 4.0 (100 mM)		2.33	25	24	☐,**B5**
☐	McIlvaine buffer, pH 6.0 (100 mM)		2.56	25	24	☐,**B5**
☐,◇	1N HCl		0.14	25	24	◇
☐,◇	0.1N HCl		0.91	25	24	◇
☐,◇	0.01N HCl		1.86	25	24	◇
☐,◇	0.001N HCl		1.88	25	24	◇

[a]☐ = Form I; ◇ = dihydrate; **B5** = parent compound; [b] wetcake analysis by capillary XRPD.

11.6 Isostructural seeding screen

Table S26. Summary of isostructural seeding crystallization experiments.

Solvent//Antisolvent	Seed	Form(s)[a]	Solvent//Antisolvent	Seed	Form(s)[a]
5:1 EtOH:water//2BuOH	**M**	**2B**,☐	5:1 EtOH:water//cyclohexanol	**I**	**cH**,☐
5:1 EtOH:water//2BuOH	**I**	**2B**,☐	5:1 EtOH:water//EtOH	**M**	**E**
5:1 EtOH:water//hexanol	**M**	☐+pk	5:1 EtOH:water//nPrOH	**M**	☐
5:1 EtOH:water//hexanol	**I**	☐	5:1 EtOH:water//iPrOH	**M**	**I**
5:1 EtOH:water//heptanol	**M**	☐	5:1 EtOH:water//1BuOH	**M**	**B**,☐
5:1 EtOH:water//heptanol	**I**	☐	MeOH	**I**	☐,**M**
5:1 EtOH:water//cyclohexanol	**M**	**cH**,☐			

[a]☐ = Form I; **M** = S-MeOH; **E** = S-EtOH; **I** = S-iPrOH; **B** = S-nBuOH; **2B** = S-2BuOH; **cH** = S-cHexOH.

11.7 Desolvation screen

Table S27. Summary of B5HCl desolvation experiments.

Starting Form	Thermal Annealing (40 °C/90 min)	Thermal Annealing (75 °C/90 min)	RH Annealing (5-95-5% RH)	RH Annealing (80% RH/24 h)
Dihydrate (◇)	□ + ◇	□ + ◇	□	◇ + 9.1, 13.7 pks
MeOH solvate (**M**)	**M** + $□_{tr}$	□ + M_{tr}	□	□ + M_{tr}
EtOH solvate (**E**)	□ + **E**	□	□	□
nPrOH solvate (**Pr**)	**Pr**	**Pr** + □	□	□
nBuOH solvate (**B**)	**B**	**B** + □	□	□
1-pentanol solvate (**P**)	**P**	□	□	□
Octanol solvate (**O**)	**O**	□	**O** + □	□
IPA solvate (**I**)	**I** + □	□	□	□
2BuOH solvate (**2B**)	**2B** + □	□	□	□
iBuOH solvate (**iB**)	**iB**	**iB** + □	□	□
Ethylene glycol solvate (**EG**)	**EG**	**EG**	□	**EG**
Propylene glycol solvate (**PG**)	**PG**	**PG**	□	□

□ = Form I; ◇ = dihydrate; **M** = S-MeOH; **E** = S-EtOH; **Pr** = S-nPrOH; **I** = S-iPrOH; **B** = S-nBuOH; **iB** = S-iBuOH; **2B** = S-2BuOH; **P** = S-nPeOH; **O** = S-nOcOH; **EG** = S-EtGly; **PG** = S-PrGly.

11.8 Solvent exchange screen

Table S28. Summary of B5HCl Solvent Exchange Experiments via Vapor Diffusion.

Starting Form	Vapor Diffusion Solvents (4 weeks)	Solid Form (^{1}H NMR, PXRD)	Starting Form	Vapor Diffusion Solvents (4 weeks)	Solid Form(s) (^{1}H NMR, PXRD)
M	MeOH + EtOH + nPrOH	**M**	**O**	MeOH + EtOH + nPrOH	**M**,**O**,**Pr**
E	MeOH + EtOH + nPrOH	**M**	**iB**	MeOH + EtOH + nPrOH	**M**
Pr	MeOH + EtOH + nPrOH	**M**	**P**	MeOH + EtOH + nPrOH	**M**,**Pr**
I	MeOH + EtOH + nPrOH	**M**	**2B**	MeOH + EtOH + nPrOH	**M**
B	MeOH + EtOH + nPrOH	**M**			

M = S-MeOH; **E** = S-EtOH; **Pr** = S-nPrOH; **I** = S-iPrOH; **B** = S-nBuOH; **iB** = S-iBuOH; **2B** = S-2BuOH; **P** = S-nPeOH; **O** = S-nOcOH.

12. Crystal Morphology

Form I

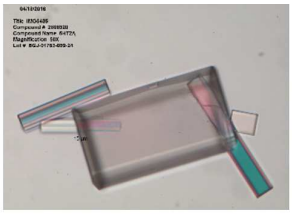

Form I

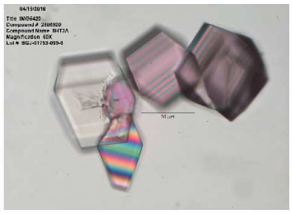

Dihydrate

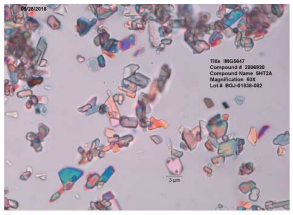

S-MeOH

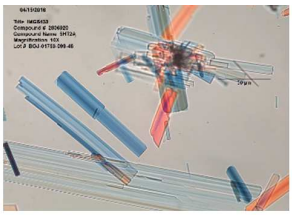

S-EtOH

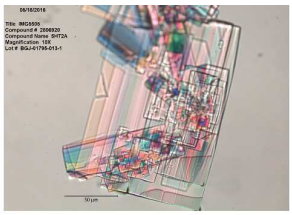

S-nPrOH

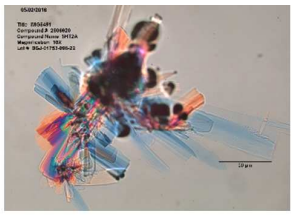

S-iPrOH

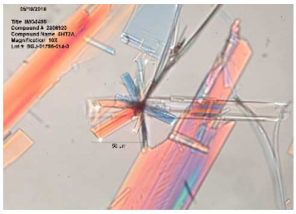

S-nBuOH

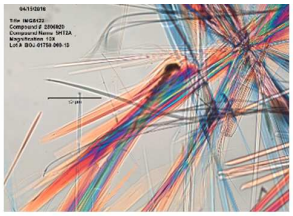

S-iBuOH

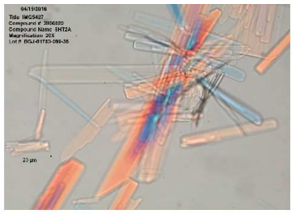

S-2BuOH

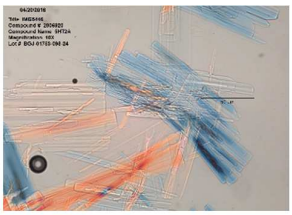

S-PeOH

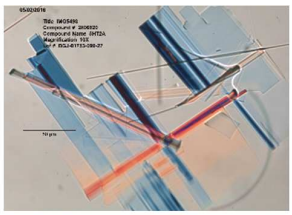

S-nOcOH

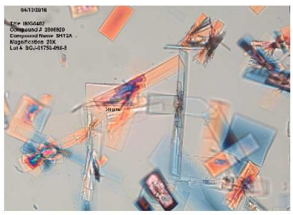

S-cHexOH?

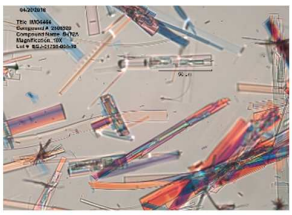

S-iAmOH?

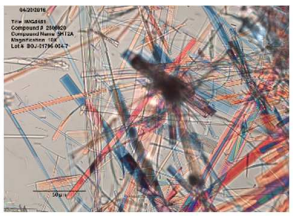

13. Differential Thermal Analysis

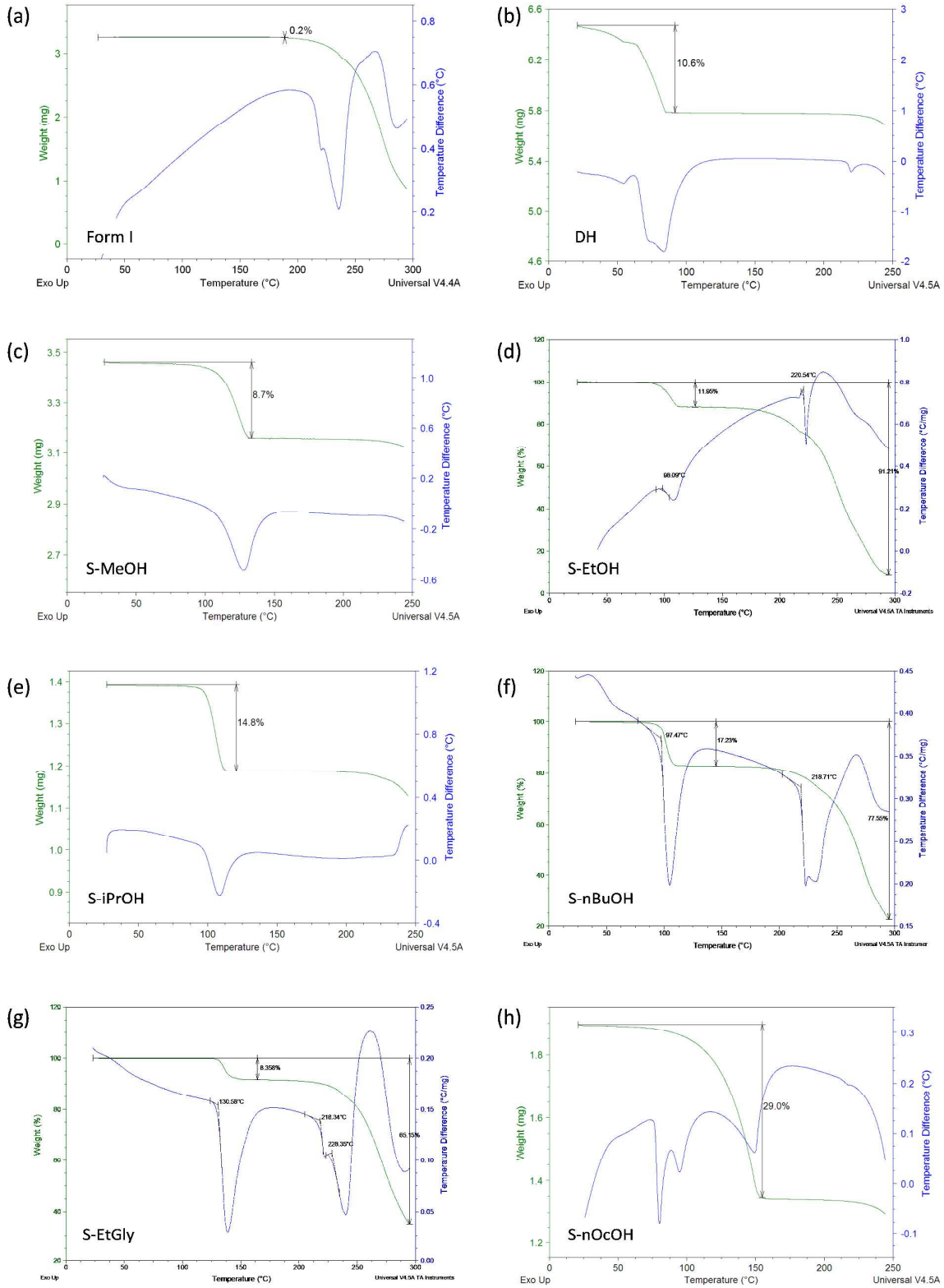

Figure S57. DTA traces of freshly prepared solid forms of B5HCl crystal forms.

Heat of Form II to Form I Transformation

DSC thermograms were recorded on a Diamond DSC (Perkin-Elmer Norwalk, Ct., USA), controlled by the Pyris 7.0 software. Using a UM3 ultramicrobalance (Mettler, Greifensee, CH), samples of approximately 5 mg were weighted into closed 3 bar aluminium pans. The samples were heated using rates ranging from 10 to 20 °C min^{-1}, with dry nitrogen as the purge gas (purge: 20 ml min^{-1}). The instrument was calibrated for temperature with pure benzophenone (mp 48.0 °C) and caffeine (236.2 °C), and the energy calibration was performed with indium (mp 156.6 °C, heat of fusion 28.45 Jg^{-1}). The errors on the stated temperature (peak minimum) and enthalpy value were calculated at the 95% confidence intervals (CI) and are based on three measurements.

And endothermic thermal event was recorded in the temperature range from 90 to 140 °C with a transformation enthalpy of –8.5 ± 0.3 kJ mol^{-1}. The presence of a transformation, and not a crystallisation event, was confirmed with hot-stage microscopy and the presence of Form I after the transformation with PXRD.

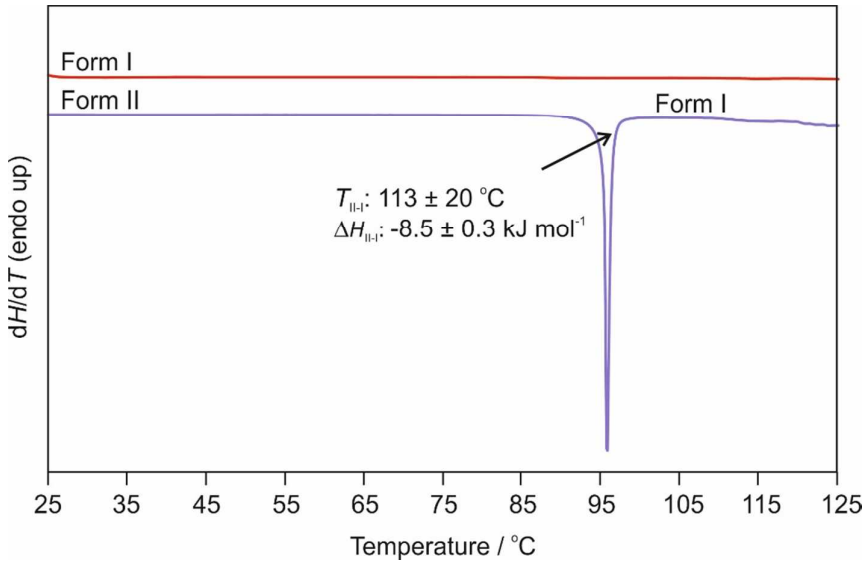

Figure S58. DSC thermograms of B5HCl anhydrate polymorphs in the temperature range from 25 to 125 °C, measured at a heating rate of 20 °C min^{-1}.

14. Gravimetric Vapor Sorption Analysis

Gravimetric Vapor Sorption. Gravimetric moisture sorption analysis (Figure S58) was performed at 25 °C using a TA Instruments VTI Model SGA-100 flow moisture balance. Approximately 20 mg of each sample was loaded into a tared glass sample pan. Moisture sorption-desorption was surveyed between 5 and 95% RH in 5% RH steps. The equilibration criterion for each step was set to <0.01% weight gain in 15 minutes for a maximum time of 120 minutes. Solid residues were collected after each run and analyzed by PXRD.

Additional moisture sorption and desorption studies were performed with the automatic multisample gravimetric moisture sorption analyzer SPS23-10µ (ProUmid, Ulm, D). The moisture sorption analyzer was calibrated with saturated salt solutions according to the suppliers' recommendations. Approximately 500 mg of sample was used for each analysis. The measurement cycles were started at 30% with an initial stepwise desorption (decreasing humidity) to 0%, followed by a sorption cycle (increasing humidity) to 95% RH and a final desorption step to 30%. The RH changes were set to 2% and 5% for measurements <30% and >30% RH, respectively. The equilibria conditions for each step were set to a mass constancy of ± 0.001 % over 60 minutes and a maximum time limit of 48 hours for each step.

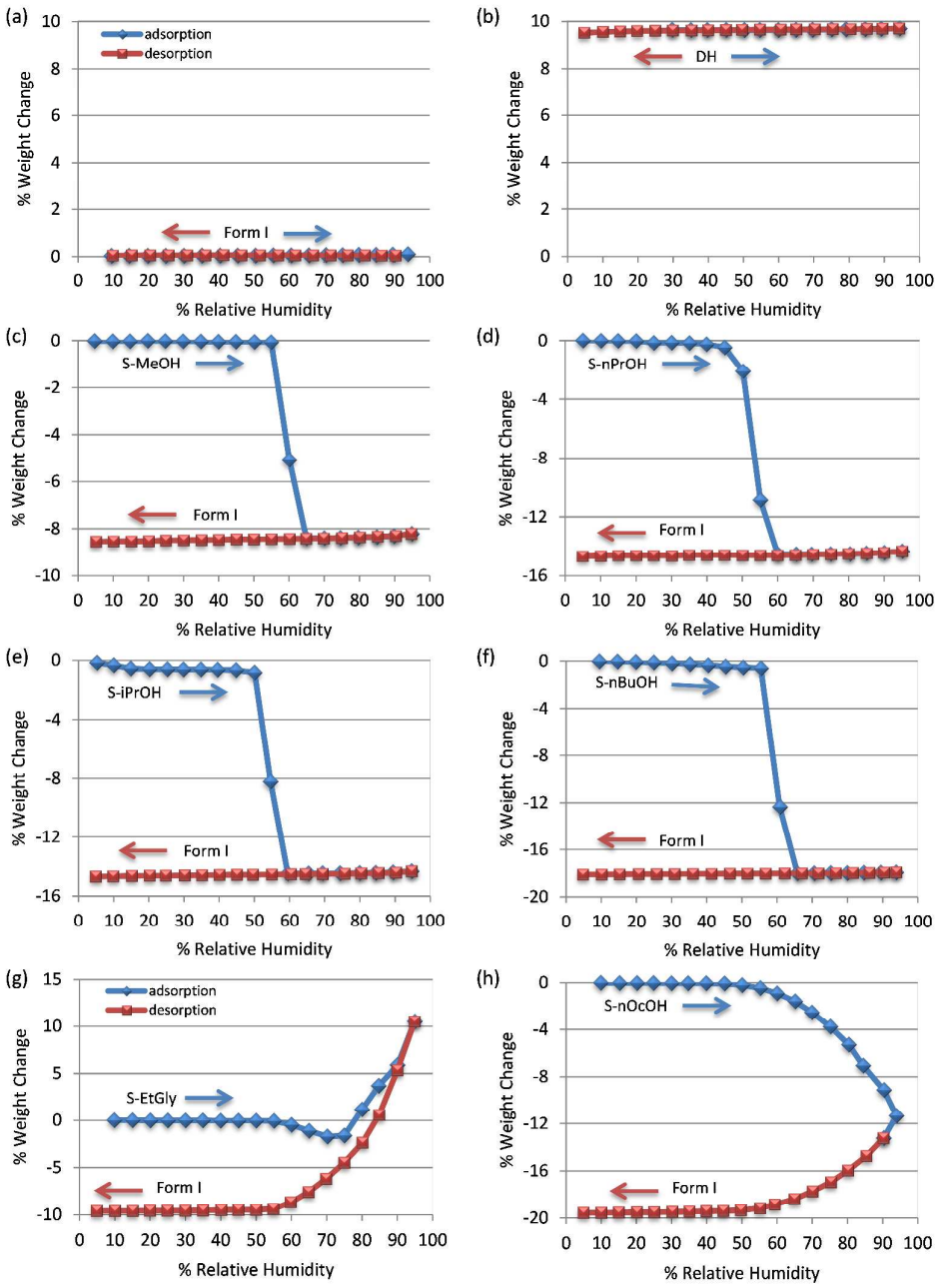

Figure S59. GVS isotherms of several B5HCl crystal forms measured at room temperature (◆ = adsorption, ■ = desorption). (a) Form I and (b) dihydrate show no signs of interconversion or appreciable water uptake (or loss) over a wide range of relative humidity (RH). All alcohol solvates show net weight *losses* during the GVS experiment, marking the loss of solvent upon conversion to Form I. Comparatively volatile solvents (MeOH, nPrOH, iPrOH and nBuOH) are lost in a sudden and stepwise fashion as the RH is increased, while the less volatile solvents (EgGly, PrGly, nOcOH) are slowly lost with weight decreases continuing throughout the desorption phase of the experiment. Whereas surface adsorption of water accelerates the transformation of (c) S-MeOH, (d) S-nPrOH, (g) S-EtGly and (h) S-nOcOH to Form I, presumably through dissolution and subsequent crystal nucleation and growth of dissolved B5HCl, there may be some exchange of the alcohol for water in the (e) S-iPrOH and (f) S-nBuOH crystal structures as shown by the slight weight loss prior to the dramatic weight change on conversion to Form I.

The DVS isotherms in Figure S59 were complemented with high-resolution sorption desorption measurements of Form I and the Dihydrate (Figure S60). In agreement with Figure S59a, the From I sample did not show a phase transition during exposure to variable RHs. Surface adsorption of water started at RH > 70% and liquefaction at the highest RH (95%). Upon decreasing the RH to < 4% RH a transformation of the dihydrate to Form II is observed. The back-transformation already occurs at RH values ≥ 10%, thus Form II show only a very limited moisture-dependent stability range at 25 °C. At ambient temperature not only Form II, but also the dihdyrate is a metastable phase, which is why a transformation to Form I is obtained. Surface liquefaction of B5HCl (dihydrate) at 95% RH is likely to induce the nucleation of Form I upon slightly decreasing the RH and furthermore a transformation to Form I is induced at RH < 70%. Starting with a mixed Form II and dihydrate sample (~5% Form I) confirmed that the presence of Form I accelerates the dihydrate for Form I transformation at RH < 70% (isotherms not shown).

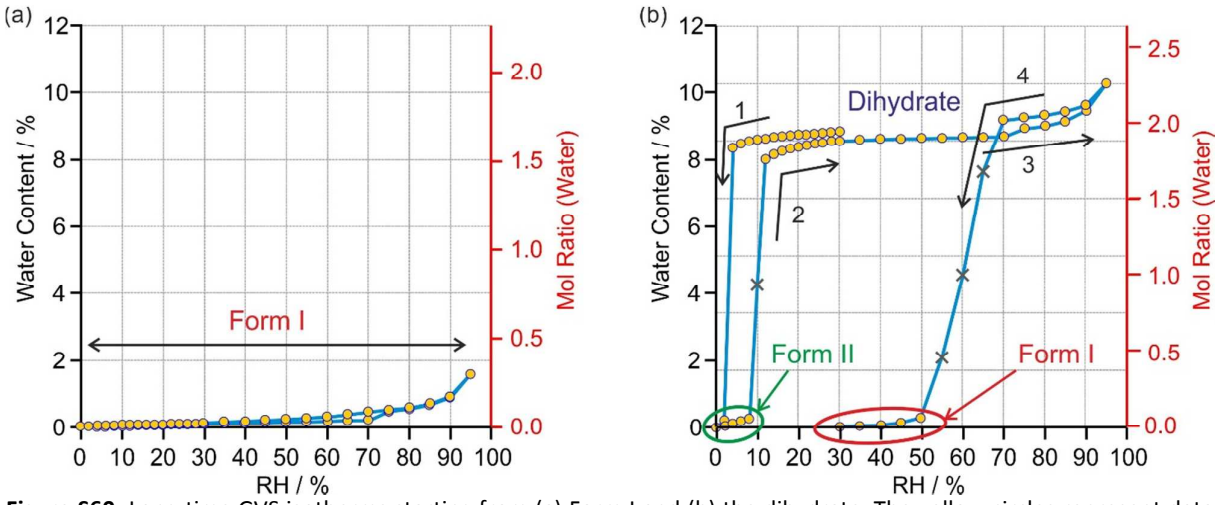

Figure S60. Long-time GVS isotherms starting from (a) Form I and (b) the dihydrate. The yellow circles represent data points reaching the equilibrium (constant mass) within the pre-set maximal equilibration time (see above), whereas crosses mark data points where the sample did not reach the equilibrium moisture content within the allowed time limit of 48 h. The order and direction of the (de)sorption isotherms is indicated by the numbers and arrows in (b).

15. Hydration of Form II

Freshly prepared Form II was stored on a PXRD well plate (25 °C and 18% RH) and the transformation to the dihydrate was measured time resolved.

PXRD patterns were obtained at room temperature using an X'Pert PRO diffractometer (PANalytical, Almelo, NL) equipped with a θ/θ coupled goniometer in transmission geometry, a Cu-K$\alpha_{1,2}$ radiation source with a focussing mirror, a 0.5° divergence slit and a 0.02° Soller slit collimator on the incident beam side, a 2 mm antiscattering slit and a 0.02° Soller slit collimator on the diffracted beam side and a solid state PIXcel detector. The patterns were recorded at a tube voltage of 40 kV and tube current of 40 mA, applying a step size of 2θ = 0.013° with 80s per step with 80 repeats, no breaks in between, in the 2θ range between 2° and 40°.

Figure S61 shows that after three hours (25 °C and 18% RH) the Form II PXRD patterns shows the strong and characteristic reflections of dihydrate. After ~17.5 hours the transformation was complete. The fact that the intensity of the Form II peak positions decreases with dihyrate reflections increasing at the same time at distinct 2theta angles indicates that upon hydration of Form II a structural change occurs. The latter is in agreement with the structure solution of Form II (ESI, section 16), distinct from DH, and the GVS data derived for DH. In case of a non-stoichiometric hydration mechanism, water ingress without significantly altering the structure, only (slight) shifts in the 2theta reflection positions would be visible.

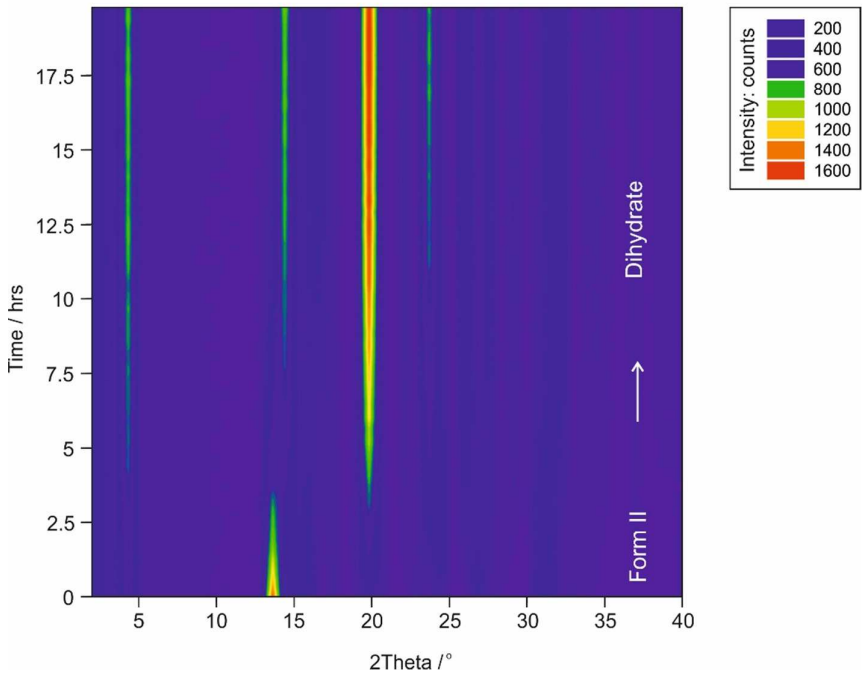

Figure S61. Guinier plots of the Form II (time 0) to dihydrate transformation.

16. Form II – Crystal Structure

The Form II diffraction pattern was indexed to a monoclinic unit cell and the space group was determined to be $P2_1/c$. From the cell volume and solid state NMR measurements it was derived that there is one $BH5^+$ and one Cl^- ion in the asymmetric unit. The data were background subtracted and Pawley refinement[13] was used to extract the intensities and their correlations. Simulated annealing was used to optimize the Form II model against the diffraction data set (156 reflections) in direct space. The internal coordinate (Z-matrix) description was derived from PBE-TS optimized structures of the dihydrate (*ea*) and Form I (*ee*), with C–H, N–H and O–H distances normalized to 0.95, 0.9 and 0.9, respectively. The structure was solved using 250 simulated annealing runs of 1.0×10^8 moves per run as implemented in DASH (2017 CSD Release). The $B5H^+$ ion was allowed 6 external and 4 internal degrees of freedom (torsions $\phi1$, $\phi2$, $\phi3$ and $\phi5$, see Figure 1) and the Cl^- ion 3 external degrees of freedom. The best solution returned a χ^2 ratio of ca. 3.24 (profile χ^2/ Pawley χ^2). Both starting conformations (*ea* and *ee*) resulted in the same minimum structure. A restrained Rietveld refinement,[14] 2θ range 3.6 to 60.0°, was carried out in TOPAS academic V5[15] using the best solution returned from the simulated annealing. The final refinement included a total of 177 parameters (21 profile, 4 cell, 1 scale, 1 isotropic temperature factor, 15 preferred orientations, 135 positons). The refinement converged at R_{wp} = 1.650 %, R_{exp} = 1.358 %, R_p = 1.279 % and χ^2 = 1.475.

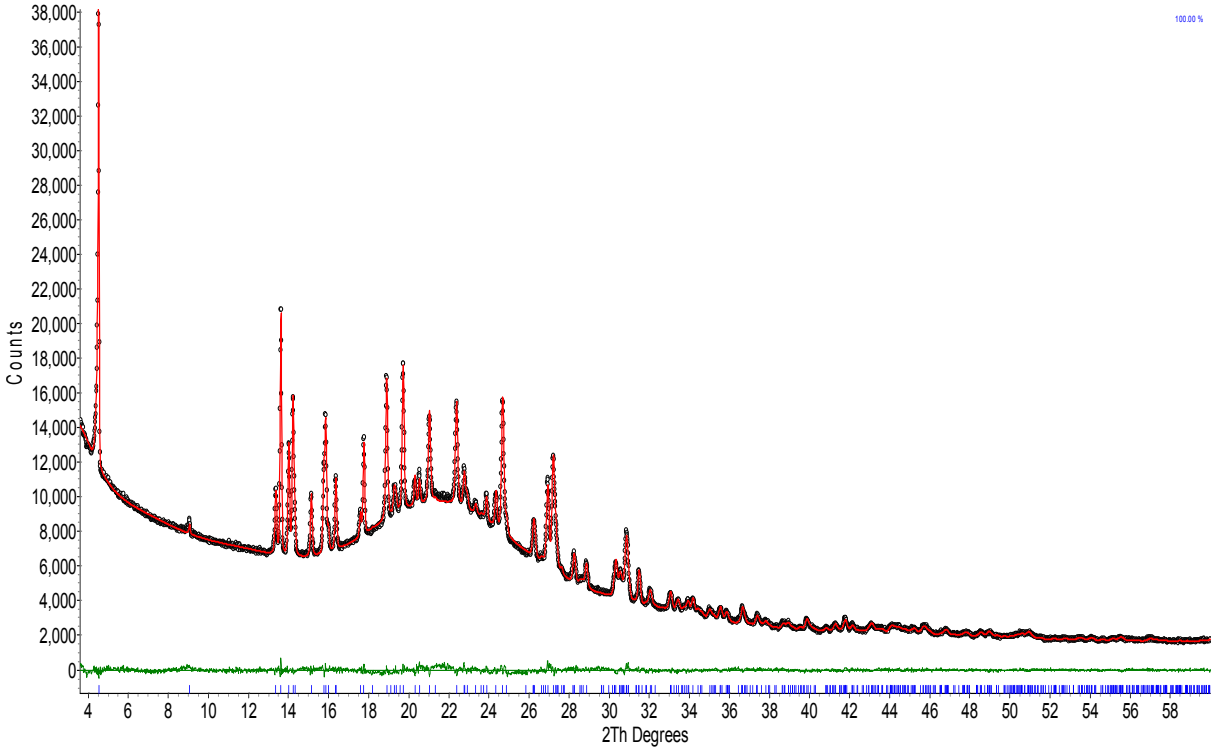

Figure S62. Observed (black points), calculated (red line) and difference (green line) profiles for the Rietveld refinements of Form II. Blue tick marks denote the peak positions.

Furthermore, a rigid body Rietveld refinement,[14] 2θ range 3.6 to 60.0°, was carried out in TOPAS academic V5[15] using the optimized PBE-TS structure of the best solution returned from the simulated annealing. The final refinement included a total of 68 parameters (35 profile, 4 cell, 1 scale, 1 isotropic temperature factor, 15 preferred orientations, 12 positons). The refinement converged at R_{wp} = 2.841 %, R_{exp} = 1.347 %, R_p = 1.839 %.

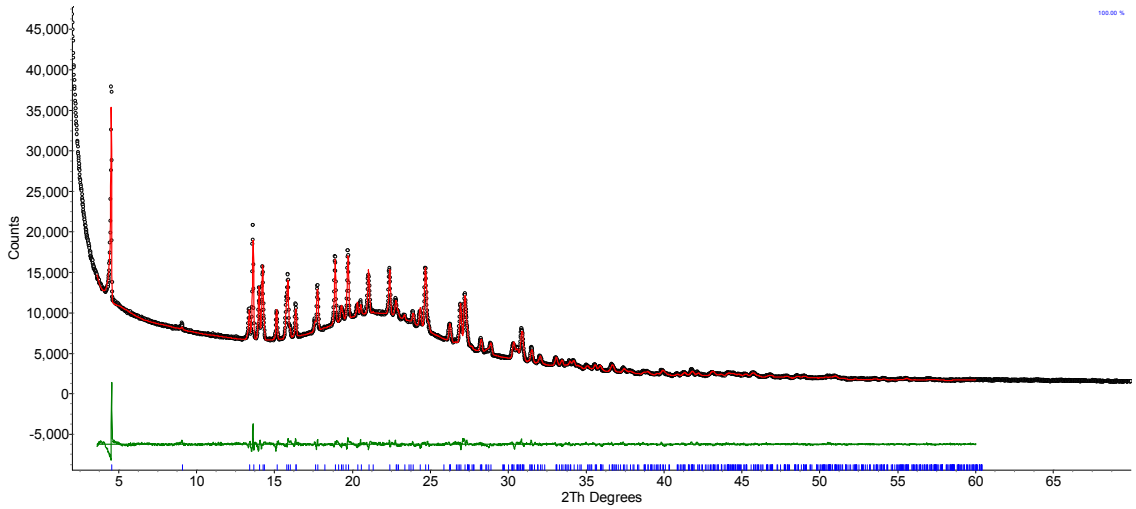

Figure S63. Observed (black points), calculated (red line) and difference (green line) profiles for the Rietveld refinements of Form II. Blue tick marks denote the peak positions.

Table S29. Crystallographic Data for Form II.

	Form II
Crystal system, space group	*Monoclinic, $P2_1/c$*
Formula	$C_{16}H_{22}ClN_3O_3$
a, Å	19.4919(3)
b, Å	6.51644(15)
c, Å	13.2350(2)
β, °	91.404(2)
Z	4
V, Å^3	1680.58(5)
T, °C	25
M (g/mol)	339.81
λ	Cu-$K_{\alpha 1,2}$

E) CSD-Survey:

A search of the CSD (ConQuest Version 1.18) was performed to find all of the crystal structures of organic chloride salts. The hits were reduced to those with full structural coordinates available, R ≤ 0.1, structures with metallic elements and double entries were removed.

The **6512** structures that full-filled the search criteria were analyzed with respect to solvate/hydrate formation and polymorphism:

- 29% of the Cl^- salts form hydrates
- 31% of the Cl^- salts form either a hydrate or heterosolvate with water (organic solvent and water included in the crystal lattice)
- Heterosolvates with water: methanol (n=46), acetonitrile (28), ethanol (26), chloroform (16), DCM (15), 2-PrOH (8), acetone (7), diethyl ether (5), 1,4-dioxane (5), benzene (4), THF (4), 1_PrOH (3), trifluroethanol (3), DMF (2), n-hexane (2), ethyl acetate (2), n-BuOH (2), acetic acid (1), pyridine (1), toluene (1), DMSO (1), ethylene glycole (1).
- 3.9% of the Cl^- salts form alcohol solvates (excl. heterosolvates with water), with methanol solvates (2,4% of Cl^- salts) and ethanol solvates (1.5%) being the "most" frequent. Furthermore, isopropanol (0.2%), nBuOH (0.1%) and ethylene glycole solvates (<0.1%) were found.
- Only 1.9% of the CSD Cl^- salts are polymorphic

Alcohol water heterosolvates were found to be rare, such as gallic acid,[16] aripiprazole,[17] tetroxoprim.[18] Isostructural solvates with the alcohol molecules located in channels are more common,[19] and olanzapine is like B5HCl in having layers of API that can accommodate a range of mixed alcohol and water molecules tethered by an OH interaction.[20]

References

1. Markvardsen, A. J.; David, W. I. F.; Johnson, J. C.; Shankland, K., A probabilistic approach to space-group determination from powder diffraction data. *Acta Crystallographica Section A - Foundations of Crystallography* **2001,** *57*, 47-54.
2. David, W. I. F.; Shankland, K.; van de Streek, J.; Pidcock, E.; Motherwell, W. D. S.; Cole, J. C., DASH: a program for crystal structure determination from powder diffraction data. *Journal of Applied Crystallography* **2006,** *39*, 910-915.
3. Williams, D. E., Improved intermolecular force field for molecules containing H, C, N, and O atoms, with application to nucleoside and peptide crystals. *Journal of Computational Chemistry* **2001,** *22* (11), 1154-1166.
4. Cooper, T. G.; Hejczyk, K. E.; Jones, W.; Day, G. M., Molecular Polarization Effects on the Relative Energies of the Real and Putative Crystal Structures of Valine. *Journal of Chemical Theory and Computation* **2008,** *4* (10), 1795-1805.
5. Etter, M. C.; MacDonald, J. C.; Bernstein, J., Graph-Set Analysis of Hydrogen-Bond Patterns in Organic- Crystals. *Acta Crystallographica Section B - Structural Science* **1990,** *46*, 256-262.
6. Braun, D. E.; McMahon, J. A.; Koztecki, L. H.; Price, S. L.; Reutzel-Edens, S. M., Contrasting Polymorphism of Related Small Molecule Drugs Correlated and Guided by the Computed Crystal Energy Landscape. *Crystal Growth & Design* **2014,** *14* (4), 2056-2072.
7. (a) Singh, S.; Thakur, T., New crystalline salt forms of levofloxacin: conformational analysis and attempts towards the crystal structure prediction of the anhydrous form. *Crystengcomm* **2014,** *16* (20), 4215-4230; (b) Braun, D.; Gelbrich, T.; Kahlenberg, V.; Griesser, U., Insights into Hydrate Formation and Stability of Morphinanes from a Combination of Experimental and Computational Approaches. *Molecular Pharmaceutics* **2014,** *11* (9), 3145-3163.
8. Black, S. N.; Collier, E. A.; Davey, R. J.; Roberts, R. J., Structure, solubility, screening, and synthesis of molecular salts. *Journal of Pharmaceutical Sciences* **2007,** *96* (5), 1053-1068.
9. Sarmah, K.; Sarma, A.; Roy, K.; Rao, D.; Thakuria, R., Olanzapine Salts and Diversity in Molecular Packing. *Crystal Growth & Design* **2016,** *16* (2), 1047-1055.
10. Grimme, S., Semiempirical GGA-type density functional constructed with a long-range dispersion correction. *J. Comput. Chem* **2006,** *27* (15), 1787-1799.
11. (a) Whalley, E., Difference in the intermolecular forces of H2O and D2O. *Trans. Faraday Soc* **1957,** *53*, 1578-1585; (b) Whalley, E., The hydrogen bond in ice. *Hydrogen Bond* **1976,** *3*, 1425-1470.
12. (a) Pickard, C. J.; Mauri, F., All-electron magnetic response with pseudopotentials: NMR chemical shifts. *Physical Review B* **2001,** *63* (24), 245101; (b) Yates, J.; Pickard, C.; Mauri, F., Calculation of NMR chemical shifts for extended systems using ultrasoft pseudopotentials. *Physical Review B* **2007,** *76* (2), 024401.
13. Pawley, G. S., Unit-Cell Refinement from Powder Diffraction Scans. *Journal of Applied Crystallography* **1981,** *14* (DEC), 357-361.
14. Rietveld, H. M., A Profile Refinement Method for Nuclear and Magnetic Structures. *Journal of Applied Crystallography* **1969,** *2*, 65-71.
15. Coelho, A. A., Indexing of powder diffraction patterns by iterative use of singular value decomposition. *Journal of Applied Crystallography* **2003,** *36*, 86-95.
16. Braun, D. E.; Bhardwaj, R. M.; Florence, A. J.; Tocher, D. A.; Price, S. L., Complex Polymorphic System of Gallic Acid-Five Monohydrates, Three Anhydrates, and over 20 Solvates. *Crystal Growth & Design* **2013,** *13* (1), 19-23.
17. Braun, D. E.; Gelbrich, T.; Kahlenberg, V.; Tessadri, R.; Wieser, J.; Griesser, U. J., Stability of Solvates and Packing Systematics of Nine Crystal Forms of the Antipsychotic Drug Aripiprazole. *Crystal Growth & Design* **2009,** *9* (2), 1054-1065.
18. Caira, M.; Bettinetti, G.; Sorrenti, M., Structural relationships, thermal properties, and physicochemical characterization of anhydrous and solvated crystalline forms of tetroxoprim. *Journal of Pharmaceutical Sciences* **2002,** *91* (2), 467-481.
19. (a) Berzins, A.; Skarbulis, E.; Actins, A., Structural Characterization and Rationalization of Formation, Stability, and Transformations of Benperidol Solvates. *Crystal Growth & Design* **2015,** *15*

(5), 2337-2351; (b) Berzins, A.; Skarbulis, E.; Rekis, T.; Actins, A., On the Formation of Droperidol Solvates: Characterization of Structure and Properties. *Crystal Growth & Design* **2014,** *14* (5), 2654-2664; (c) Watabe, T.; Kobayashi, K.; Hisaki, I.; Tohnai, N.; Miyata, M., Guest-induced supramolecular isomerism and chirality of brucine inclusion crystals with aliphatic alcohols: A hierarchical interpretation. *Bulletin of the Chemical Society of Japan* **2007,** *80* (3), 464-475; (d) Stieger, N.; Liebenberg, W.; Wessels, J.; Samsodien, H.; Caira, M., Channel inclusion of primary alcohols in isostructural solvates of the antiretroviral nevirapine: an X-ray and thermal analysis study. *Structural Chemistry* **2010,** *21* (4), 771-777.

20. Bhardwaj, R. M.; Price, L. S.; Price, S. L.; Reutzel-Edens, S. M.; Miller, G. J.; Oswald, I. D. H.; Johnston, B. F.; Florence, A. J., Exploring the Experimental and Computed Crystal Energy Landscape of Olanzapine. *Crystal Growth & Design* **2013,** *13* (4), 1602-1617.